Energy and Exergy Analysis of Nanofluid Based Solar Assisted Power Generation and Absorption Cooling Systems

Muhammad Abid

Submitted to the
Institute of Graduate Studies and Research
in partial fulfillment of the requirements for the degree of

Doctor of Philosophy
in
Mechanical Engineering

Eastern Mediterranean University
September 2016
Gazimağusa, North Cyprus

Approval of the Institute of Graduate Studies and Research

Prof. Dr. Mustafa Tümer
Acting Director

I certify that this thesis satisfies the requirements as a thesis for the degree of Doctor of Philosophy in Mechanical Engineering.

Assoc. Prof. Dr. Hasan Hacışevki
Chair, Department of Mechanical Engineering

We certify that we have read this thesis and that in our opinion it is fully adequate in scope and quality as a thesis for the degree of Doctor of Philosophy in Mechanical Engineering.

Asst. Prof. Dr. Tahir A.H. Ratlamwala
Co-Supervisor

Prof. Dr. Uğur Atikol
Supervisor

Examining Committee

1. Prof. Dr. Uğur Atikol
2. Prof. Dr. Javed Ahmad Chattha
3. Prof. Dr. Fuat Egelioğlu
4. Prof. Dr. Sümer Şahin
5. Asst. Prof. Dr. Murat Özdenefe

ABSTRACT

The present study is conducted to perform the comparative analysis of solar assisted multi-effect absorption cooling systems. Absorption cooling cycles, from single to quadruple effects are analyzed for their energy and exergy perspectives. In the first half of the analysis, the solar collectors (parabolic trough and parabolic dish) are modelled and analyzed using water based nanofluids of Al_2O_3 and Fe_2O_3. Secondly, the absorption cooling cycles of single, double, triple and quadruple effects are simulated and analyzed separately. Then finally, they are integrated with solar collectors to produce power as well as to provide heating and cooling effect.

All the four absorption cycles are designed to work on LiBr-H_2O working pair and are analyzed for their coefficient of performance (COP) as well as exergetic performance viewpoints. The absorption cycles are operated on a heat source of solar energy collected through solar collectors. It is observed that the quadruple effect absorption cycle (QEAC) has substantial performance enhancement over the double and triple effect absorption cycles. The QEAC consists of four generators and four condensers coupled together, making an extension of triple effect absorption cycle where there are three condensers and three generators joined together to complete the cycle. The system is designed to work on parallel flow system. All four absorption cycles are designed to have the identical cooling output and same operating conditions. Engineering Equation Solver (EES) software is used to simulate and study the effects of various operational aspects on the COP and exergetic performance of the cycles. The triple effect absorption cycle is observed to have COP of more than twice the single effect and for quadruple it is 2.55 times higher than single effect absorption cycle. The exergetic efficiency of the quadruple absorption effect cycle is 11.7% higher than single effect and 6% higher than triple effect absorption cycle. It is found that for a fixed evaporator temperature and for a fixed condenser load, there is an optimal temperature of the generator, where the COP and exergy efficiency are found to be maximum. A small modification of mass distribution among the generators would help in higher COP without requiring any additional heat input. Quadruple effect absorption cycle works on higher heat source temperatures in comparison to single effect absorption cycle but requires less heat input to produce the same cooling effect.

Keywords: solar collectors, absorption cooling, LiBr-H_2O, quadruple effect, COP, exergy efficiency.

ÖZ

Bu araştırma, güneş destekli çoklu etki emme soğutma sistemlerinin karşılaştırmalı analizini gerçekleştirmek için yapılmıştır. Yapılan çalışmada soğutma, soğurma, enerji ve kullanılabilir enerji bakış açıları bir den dörtlü etkilere kadar var olan döngüler ışığında analiz edilmiştir. Analizin ilk bölümünde, güneş kolektörleri (parabolik oluk ve parabolik çanak) modellenmiş ve Al_2O_3 ve Fe_2O_3 su bazlı küçük sıvılar kullanılarak analiz edilmektedir. İkinci olarak tek, çift, üçlü ve dörtlü etkilerin döngüleri soğutma emilimi üzerine uygulanıp her biri ayrı ayrı analiz edilmekle beraber güç üretmek yanı sıra ısıtma ve soğutma etkisini sağlamak için güneş kolektörleri ile entegre edilmiştir. Araştırmaya konu edilen dört emme döngüsü LiBr-H_2O çalışma çifti üzerinde çalışmak üzere tasarlanmış ve performans katsayısı (COP) kullanılabilir enerji verimlilik bakış açıları için analiz edilmiştir. Emme döngüleri güneş kolektörleri tarafından toplanan güneş enerjisinin bir ısı kaynağı üzerine işletilmektedir. Dörtlü Etki Emme Döngüsü (QEAC), çift ve üçlü etki döngüleri üzerinde önemli performans özelliklerine sahip olduğu görülmektedir. Dörtlü Etki Emme Döngüsü (QEAC) ‘nün tamamlanabilmesi için dört jeneratör, dört kondansatör ve ayrıca üçlü etki döngüsünün genişletilmesi için üç jeneratör ve üç kondansatör bir birine eklenerek oluşturulmuştur. Sistem paralel akış sistemi üzerinde çalışmak üzere tasarlanmıştır. Tüm emme döngüleri aynı soğutma çıkışı ve aynı işletim koşullarına sahip şekilde tasarlanmıştır. Çalışma sırasında mühendislik Denklem Çözücüsü (EES) yazılımı simüle edilmiş ve performans katsayısı (COP) ekserji performansına bağlı olarak operasyonel etkileri çeşitli açılardan incelenmiştir. Sonuç olarak üçlü etki döngüsünün performans kat sayısı (COP) tek döngünün iki katından daha fazla etkili olduğu görüşmüştür. Ayrıca dörtlü etkinin tek etkili döngüsünden 2.55 kat daha fazla olduğu tespit edilmiştir.

Dörtlü etki döngüsünün ekserji verimi açısından tekli etkisine göre % 11,7 daha yüksek ve üçlü etki emme döngüsünden % 6 daha yüksektir. Jeneratörün uygun değer sıcaklığına ulaştığı noktada sabit bir buharlaştırma sıcaklığı ve sabit bir kondenser yükü için performans katsayısı (COP) ve ekserji verimliliğinin yüksek olduğu bulunmuştur. Bununla beraber performans katsayısı (COP) ilave ısı girişi olmaksızın artmış olup, ancak pompalanan çözelti akış oranında küçük optimizasyonu ile jeneratör arasında kütle dağılımı olabilir. Dörtlü etki döngüsü tek etkili döngüye göre daha yüksek ısı kaynağı ile çalışır ama aynı soğutma etkisini üretmek için daha az ısı girişi gerekmektedir.

Anahtar Kelimeler: Güneş kollektörleri, Emme soğutma, $LiBr\text{-}H_2O$, Dörtlü etki, performans katsayısı (COP), Ekserji verimliliği.

DEDICATION

To My Beautiful Wife

ACKNOWLEDGMENT

I would love to express my special thanks to my supervisor and Co-supervisor Prof. Dr. Uğur Atikol and Asst. Prof. Dr. Tahir A. H. Ratlamwala for their support and help through my thesis work. They helped me a lot with their critical suggestions to complete my work on time. It was really a very valuable experience to work under their supervision.

I have to thank Prof. Dr. Uğur Atikol for his incessant encouragement throughout my studies.

A bundle of thanks to my lovely wife, Saadia ABID and beautiful daughter, Barirah, my brother Muhammad Shabbir, my in-laws and everyone who supported me and encouraged me in finishing my work.

Once again, really very thankful to Dr. Tahir Ratlamwala for letting me to be his student, it's a great privilege to work under his guidance, and he is always very supportive and enthusiastic for research. I wouldn't have completed my degree without his support, Sir, thank you very much.

I would like to thank Almighty Allah for everything He has blessed me with. I am really thankful to my lovely parents who worked very hard to make me a person who I am today.

TABLE OF CONTENTS

LIST OF TABLES

LIST OF FIGURES

LIST OF ABBREVIATIONS

A_{ap}	area of the collector aperture (m^2)
A_r	receiver area (m^2)
C	concentration ratio
C_p	specific heat capacity (J / g °C)
$D_{r,o}$	outer diameter of receiver (m)
$D_{c,o}$	outer diameter of cover (m)
$\dot{E}x$	Exergy rate (kW)
F_r	heat removal factor
G_b	solar irradiation (w/m^2)
h_r	radiation heat transfer coefficient
h_0	convection heat transfer coefficient
h	enthalpy (kj/kg)
$h_{c,ca}$	convection heat transfer coefficient between outside environment and glass cover
K_r	thermal conductivity of receiver tube
L	length of the solar receiver (m)
$\dot{m}$	mass flow rate (kg/s)
Nu	Nusselt number
U_L	overall heat loss ($W/m^2.C$)
$\dot{Q}$	Heat transfer rate (kW)
R	receiver
R_e	Reynolds number
S	absorbed solar radiation (w/m^2)

U_0	overall heat loss coefficient
$\dot{W}$	Work rate (kW)
V	velocity (m/s)
T_0	ambient temperature (K)
T_c	glass cover temperature (K)
T_r	receiver temperature (K)

Greek letters

ϵ	surface emissivity
ρ	density (kg/m^3)
η	efficiency
μ	dynamic viscosity
k	thermal conductivity

Subscripts

abs	absorbed
avg	average
b	boiler
cond	condenser
col	collector
dest	destroyed
en	energy
evp	evaporator
ex	exergy
gen	generator

i	inner
n_f	nanofluid
o	outer
p	pump
r	receiver
sol	solar
s	ideal
st	steam
0…16	state numbers

Acronyms

CFWH	closed feed water heater
CSC	concentrating solar collector
CNT	carbon nanotube
DCC	double condenser coupling
DCCA	double condenser coupled alternate
DE	double effect
DEAC	double effect absorption cycle
HPT	high pressure turbine
HE	heat exchanger
HHE	high heat exchanger
HTF	heat transfer fluid
HTC	high temperature condenser
HTG	high temperature generator
LHE	low heat exchanger

LPT	low pressure turbine
LTD	low temperature desorber
LTG	low temperature generator
MTG	medium temperature generator
MHE	medium heat exchanger
OFWH	open feed water heater
PT	parabolic trough
PD	parabolic dish
PDSTPP	parabolic dish solar thermal power plant
QE	quadruple effect
RERDC	Renewable Energy Research and Development Center
SDR	solution distribution ratio
SC	solar collector
SE	single effect
SNL	sandia national laboratories
SEAC	single effect absorption cycle
STPP	solar thermal power plant
TE	triple effect
VHTG	very high temperature generator
VRA	vapor recompression absorber
3C3D	three condenser three desorber

Chapter 1

INTRODUCTION

1.1 Background

The traditional energy resources such as fuel oil cause ecological complications, which are considered as serious threats for the viability of energy systems. Owning to these environmental issues and the high prices of fossil fuels, the use of solar energy or other renewable energies for power production is growing gradually. Renewable energies, such as solar energy, is considered the utmost favorable alternative to be used for power generation purposes. The role of the solar energy is a key in providing pollution free energy and fulfilling the desired energy demand. Solar energy collectors are being used to produce electricity as well as to fulfil the cooling and heating demands. The solar energy collectors for instance, flat plate, parabolic trough and parabolic dish, are in use to harness solar energy. The solar collectors are assessed on the basis of their performance. Better design parameters would affect the performance of solar collectors Bellos et al. [1]. The application of heat transfer fluids (HTFs) would be a factor to be considered to have positive impact on the performance of collectors. The high HTFs such as nanofluids, would be employed to increase the efficiency of solar collectors. Nanofluids are proved to have better thermal properties in comparison to traditional base fluids, and can be used to play a pivotal role in augmenting heat transfer properties of solar collectors Yamin and Li [2].

Nanofluids are the combination of nanoparticles and base fluids. These nano sized particles can be of pure metals (aluminum, zinc, copper, silver, etc.) or of metal oxides (aluminum oxide, ferric oxide (Iron (III) oxide), copper oxide, etc.). The fraternization of nanoparticles in standard base fluids effects the properties of the conventional base fluids. The application of nanofluids in solar collectors is more constructive as nanofluids have better heat transfer properties than base fluids Li et al. [3].

1.2 Absorption Cooling

Absorption cooling systems also known as “absorption chillers” are devices, which function similar to vapor compression refrigeration cycles. The compressor is replaced by a generator, an absorber, a heat exchanger and a pump to compress the working fluid. The COP of the absorption coolers is lower as compared to conventional refrigeration systems, but they are required to work on less expensive heat source, such as solar energy and geothermal energy. The basic absorption cooling system and its working principle is displayed in Fig. 1. It comprises of an absorber, an evaporator, a condenser, a generator, a pump and a heat exchanger. The heat from an outer source, such as solar or geothermal energy drives the generator. The solution (LiBr-H_2O) is being heated in the generator resulting in splitting the refrigerant (water vapor) from the solution. The refrigerant goes to the condenser and exchanges heat in the condenser. The refrigerant gets condensed in the condenser by an exchange of heat with the cooling water and goes to the evaporator by flowing through the refrigerant valve. In evaporator, it produces cooling affect by extracting heat from the outer environment. The high concentration solution exiting the generator goes to the absorber by flowing through the heat exchanger (HE), where it loses heat to the less concentrated solution and enters into the absorber. The high concentrated solution absorbs the refrigerant leaving the evaporator and enters into the pump as a weak solution. The weak solution is pumped to the generator pressure with the help of a pump. The pressurized solution flows through the heat exchanger and enters into the generator, where it gets heated from an external heat source to separate the vapor from the solution. The frequently used working pairs in absorption cycles are mixture of LiBr-H_2O and NH_3-H_2O.

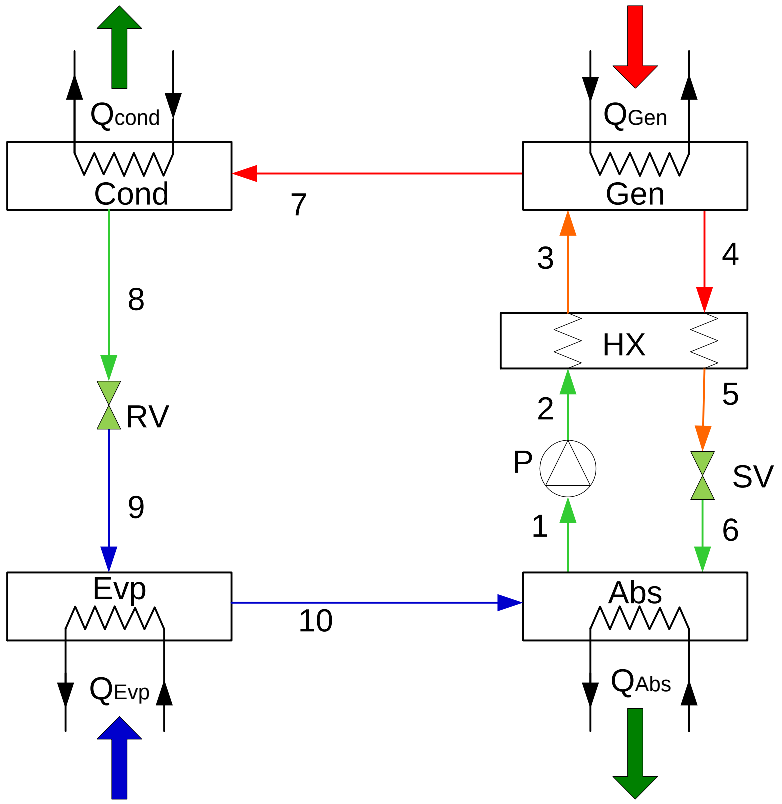

Figure 1: The single effect absorption cooling cycle

1.3 Objectives of the present research

This PhD work is conducted to investigate the performance of a solar assisted reheat Rankine cycle and multi-effect absorption cooling systems operated on a mixture of LiBr-H_2O. The application of nanofluids in solar collectors to produce useful heat and to drive steam turbine as well as to drive absorption cooling machines is unusual. The solar energy has not been used before to drive the generators of the higher stages of absorption cycles, especially the quadruple effect cycle. Therefore, this exclusive research has been conducted to find out the possibility to drive the high temperature generators of the multi-effect (single-quadruple effect) absorption cooling cycles using solar heat. The aim of the present study is to examine the impact of nanofluids on the efficiency of collectors. The higher efficiency of solar collectors would help in increasing the performance of Rankine cycle in addition to absorption cycles. The objective is to investigate the performance enhancement of absorption cooling cycles using nanofluids as well as by increasing their stages. The outline to achieve the objectives of this study is given as follows:

1. To simulate and analyze the solar collector models of parabolic trough solar collector (PTSC) and parabolic dish solar collector (PDSC) using nanofluids. The solar collectors are evaluated for their energetic and exergetic performance evaluation.
2. The simulation results are validated with the experimental results obtained for PTSC working on Al_2O_3-water based nanofluids.
3. To simulate and analyze the model of reheat Rankine cycle for power production. The reheat Rankine cycle is evaluated further for its energetic and exergetic efficiency.
4. The solar collectors of parabolic trough and parabolic dish are integrated with reheat Rankine cycle. The combined system is further evaluated to explore the overall productivity of the incorporated system.
5. To model the absorption cooling systems for cooling production.
    i. Modelling and analysis of single effect absorption cycle (SEAC).
    ii. Modelling and analysis of double effect absorption cycle (DEAC).
    iii. Modelling and analysis of triple effect absorption cycle (TEAC).
    iv. Modelling and analysis of quadruple effect absorption cycle (QEAC).

6. Integration of solar collectors with absorption cycles.
    1. The solar collectors of parabolic trough and parabolic dish are integrated with the above mentioned absorption cycles.
    2. The thermodynamic analyses of the integrated system are carried out to evaluate the COP as well as exergetic performance of the systems.

1.4 Thesis Organization

The composition of this PhD thesis consists of the succeeding chapters:

Chapter 1 provides the introductory information of the thesis. Chapter 2 provides a detailed review of the literature results, including a detailed survey of nanofluids, the solar collectors working on nanofluids. It includes a comprehensive appraisal of the solar collectors to be employed for power generation purposes. It also discusses the absorption cooling systems of single, double, triple and quadruple effects in detail. The system description of parabolic trough and parabolic dish solar collectors is provided in chapter 3. The description includes the integration of solar collectors with thermal power plant (Rankine cycle). The system description of the absorption cycles of SE, DE, TE and QE is described with the help of schematic diagrams. Finally, the solar driven absorption cycles are discussed thoroughly. Chapter 4 describes the methodology applied to model the solar collectors and the solar assisted thermal power plants. It also explains in detail the methodology used to design and analyze absorption cooling systems starting from single to quadruple effect cycles. Chapter 5 describes the thermophysical properties and preparation of nanofluids. The equations used to calculate those properties are discussed in detail. It also includes the illustration of the experimental setup. Chapter 6 discusses the results and discussion of the analyzed systems. The first part of chapter 6 provides the validation of simulations with experimental results of PTSC using nanofluids as HTFs. The second part explains in detail the simulation analysis solar collectors and their validation with literature results. It also provides detailed analysis of solar integrated thermal power plants. The last part of chapter 6 provides comprehensive analysis of multi-effect absorption cooling systems along with their validation and comparison between multistage absorption cycles. Chapter 7 summarizes the conclusions and provides recommendations for future research.

Chapter 2

LITERATURE REVIEW

Advancement in renewable energy technologies, such as geothermal, wind and solar for the replacement of those using fossil fuels is the need of the day. Scientists have been putting remarkable efforts into this matter for some decades [4, 5]. Solar energy, is a serene, free and easily obtainable energy source and could be a substitute to fossil fuels [6]. The harnessing of solar energy through standard base fluids is a traditional practice for many years, however; utilizing nanoparticles with regular base fluids as solar absorbers is an unusual approach in solar applications. It has been proved experimentally as well as theoretically that the nanofluids are better heat conductors (higher thermal conductivity) and can be advantageous to be used as heat transfer fluids [7]. The integration of solar energy with power production technologies play a vital role to fulfill energy demand. Power production applications such as steam power plants are currently integrated with parabolic trough solar collectors (PTSCs) to produce electricity [8].

2.1 Nanofluids

Nanofluids are very tiny atoms mixed in conventional fluids. S.U. Choi [9] used the colloidal particles of aluminum oxide in water and named them nanofluids. He observed that the properties of the base fluids get affected upon adding a minute fraction of nanoparticles in daily life fluids. Eastman et al. [10] presented their results on thermal conductivity enhancement using nanofluids. The authors used Al_2O_3 and CuO nanoparticles mixed in distilled water and observed the thermal conductivity to be increased by 29% and 60% respectively at 5% volume fraction of nanoparticles. The thermal conductivity (*k*) of Cu/oil nanofluids was noticed to increase about 44% by dispersing 0.052% volume fraction of Cu nanoparticles mixed in oil. Roetzel et al. [11] carried out their analysis using ethylene glycol and H_2O to prepare nanofluids of Al_2O_3 and CuO. They witnessed an increment of 20% in thermal conductivity at 4% volume fraction of CuO nanoparticles.

Li et al. [12] reported in their review article that the researchers have tried different methods, different preparation techniques and models to observe and analyze the effects of nanofluids on thermophysical properties of traditional fluids. Wen and Ding [13] conducted an empirical analysis using carbon nanotube-water nanofluids and revealed that the thermal conductivity of nanofluids was higher in comparison with daily use fluids. Natarajan and Sathish [14] revealed that the use of carbon nanotube (CNT) improves the properties of the base fluids, and proposed that nanofluid enhances the performance of solar collectors upon using them as heat transfer fluids (HTFs). Masuda et al. [15] conducted their analysis using aluminum oxide and titanium oxide nanoparticles and witnessed 32% and 11% growth in the thermal efficiency of oxides in H_2O at a weight fraction of 4.3%. Grimm [16] performed an experimental analysis using Al_2O_3 nano powder of size (1-80nm) dispersed in water and witnessed to achieve 100% improvement in thermal conductivity at 0.5-10% weight fraction of nanoparticles. The effect of pH variations on the properties of nanofluids is surveyed by many researchers [17-22]. The positive or negative deviation in pH of nanofluids at equal electrical charge, enhances the revulsion force which results in reduced clustering of particles. The reduction in clustering increases the particles’ durability and therefore resulting in higher thermal conductivity of nanofluids [23–25]. Thomas and Sobhan [26] carried out an experimental evaluation to measure the effective thermal conductivity using nanofluids, and observed in their analysis that the use of nanoparticles does have an effect on the properties of the base fluids.

Wang et al. [27] performed experimental studies to evaluate the viscosity effects of nanofluids by three methods and did not observe any non-Newtonian effects. They found a 30% increase in viscosity for the Al_2O_3-water nanofluid in comparison to pure water at 3% volume fraction of the nanoparticles. On the other hand, the research conducted by Pak and Cho [28] shows much higher viscosity in comparison to the results presented by [27]. The studies conducted by Choi et al. [29] shows that the discrepancy may be due to the technique used, which may not be suitable for fluids that contains acids or bases. However, the studies performed by Das et al. [30] shows that the viscosity was independent of shear rate. In another study conducted by Das et al. [31] shows the viscosity effects at different particle concentrations that was measured by a rotating-disc method. The results of their findings show that the behavior of nanofluids is perfectly Newtonian. Heat transfer studies under convective conditions are rather scarce. Choi [32] presented a theoretical studies for the assessment of convection heat transfer enhancement, which essentially means a dramatic decrease of pumping power for a given heat transfer.

Xuan and Roetzel [33] were the first to indicate a mechanism for heat transfer in nanofluids. They projected thermal dispersion as a major mechanism of heat transfer in flowing fluid, along with the enhancement of thermal conductivity of nanofluids. However, they didn’t present any evidence to support their claims. Pak and Cho [28] presented their results using nanofluids, even though the Nusselt number increases, the heat transfer coefficient actually decreases by 3–12%. However, this may be due to the large increase in viscosity they observed. In contrast, Eastman et al. [34] showed that with less than 1% volume fraction of CuO, the convection heat transfer rate increased by more than 15% in pure water. The work of Putra et al. [35] showed that natural convection in nanofluids deteriorated with concentration of nanoparticles and observed to be less than the base fluid.

2.2 Application of Nanofluids in Solar Collectors

Recently some studies have been reported about the use of nanofluids in solar collectors. Yousefi et al. [36] evaluated experimentally the impact of aluminum oxide-water nanofluids on the efficiency of FPSC. The weight fraction of 0.2% of nanoparticles is used to mix in distilled water and perceived an increase of 28.3% in efficiency through nanofluids. Otanicar et al. [37] carried out an experiential analysis on prototype solar collector using nanofluids and found an enhancement of 5% in the efficiency using nanofluids as HTFs. Enhancement in efficiency of solar collectors was also observed even at very small percentage of nanoparticles of silver oxide, graphite and carbon nanotubes (CNT's) mixed in water. Tyagi et al. [38] executed a theoretical investigation to observe the influence of Al_2O_3-H_2O nanofluids on direct absorption solar collectors (DASCs) and observed 9 times higher incident solar radiation as compared to water. It was also witnessed that the DASC are about 10% more efficient in comparison with FP solar collectors. The authors used 0.1 to 0.5 volume percentage of nanoparticles and an enhancement in efficiency was witnessed at low percentage of nanoparticles, but it started to level off with increase in percentage of nanoparticles. Otanicar and Golden [39] explored the effects of nanofluids on solar collectors economically as well as environmentally, and compared their efficiency with the conventional flat plate solar collectors. Saidur et al. [40] explored the possible application of nanofluids in areas such as, cooling and heating industry, medicine, fuel cells, heat exchangers and solar water heaters. In another work conducted by Yousefi et al. [41] using multiwall carbon nanotube and water nanofluids concluded to achieve higher efficiency upon using nanofluids. It was also witnessed that the amount of surfactant (TritonX-100) does effect the performance of solar collector. The authors also reported that difference in pH values too affects the efficiency of the solar collector. The research performed by Taylor et al. [42] displayed the possibility of investigating two prototypes simultaneously to observe their effect on optical properties of the nanofluids. The authors concluded that the sunlight can be captured up to 95% by using nanofluids as the heat transfer fluids. The application of nanofluids as base fluids in non-concentrating collectors have been explored by some researchers [43-44]. The nanofluids are investigated to identify their effect on the heat flux of the solar collectors [45-46]. The research conducted by Lenert and Wang [47] demonstrates that the volumetric percentage of nanofluids increases the efficiency to 35% upon incorporating it with Rankine cycle. Saidur et al. [48] conducted a study for the probable application of nanofluids in refrigeration systems to enhance the thermophysical properties of the refrigerants. The researchers concluded that more focused study needs to be performed in order to identify the reasons of heat transfer improvement and irrelevant rise in pressure.

Alternatively, several studies have been performed on exergy analysis of PTSCs. Conducting exergetic analysis of solar collectors is crucial to discover the optimal working conditions and to analyze the real work potential of the energy systems. Researchers such as, Kahrobaian and Malekmohammadi [49] conducted exergetic analysis to explore the performance of linear PTSCs and suggested to conduct the exergy analysis along with energy analysis to evaluate the real performance of PTSCs. Ceylan and Ergun [50] performed experimental evaluation of temperature controlled

PTSC. The authors performed a detailed exergy and energy analysis of PTSC. Zamfirescu and Dincer [51] performed exergetic evaluation of solar collectors and recommended to perform the exergy analysis of solar collectors because the exergetic analysis measures the real performance of solar collectors. Dincer and Rosen [52] explored the causes of lower collector performance and claimed that the performance gets affected by the lost work potential in between the different parts of the solar collector. Hou et al. [53] carried out a theoretical investigation of PTSC to evaluate the energy and exergy efficiencies. Liang et al. [54] performed a comparative study for one-dimensional PTSC models based on the experimental results taken from sandia national laboratories (SNL). The authors concluded that the 1-D models have better performance than 3-D models. Kalogirou S. A. [55] proposed a novel methodology to carry out the exergetic analysis of concentrated solar collector (CSC) to evaluate the real potential of CSCs. Al Suleiman et al. [56] performed a detailed exergetic analysis of parabolic trough solar thermal power plant (PTSTPP). They produced power by integrating PTSCs with Rankine cycle as well as with gas cycle. The exergy efficiency was observed to be increased from 8% to 20% using multi-generation instead of power generation only. Kaushik et al. [57] evaluated the energetic and exergetic aspects of PTSTPP. It was witnessed that the energy loses were maximum at the condenser and exergy loses were found to be higher in receiver-collector assembly. Gupta and Kaushik [58] conducted a theoretical evaluation of direct steam generation power plant (DSGPP). The authors carried out both first and second law analysis of the plant and concluded to have observed higher exergy loses in solar collector field and the energy loses were found to be higher in condenser assembly. Kullar et al. [59] have performed theoretical evaluation to estimate the thermal efficiency of parabolic trough (PT) solar collectors operated on nanofluids. It is perceived in their findings that the thermal efficiency is approximately 5–10% higher in comparison to traditional PT solar collector. The literature shows that the behavior of nanofluids in flat plate and parabolic trough collectors have been investigated numerically as well as experimentally.

The parabolic dish solar collectors have been studied numerically [60-64] to evaluate the performance of solar Stirling engines on the basis of geometry effects. The geometry effects play an important role in heat transfer enhancement, because the heat convection coefficient is a strong function of geometry. The experimental analysis of parabolic dish solar collectors have also been conducted by some other researchers [65-69] using Stirling engine to produce electricity. It is observed that most of the literature studies were conducted to evaluate the performance of Stirling engines on the basis of geometry effects using standard base fluids. The applications of nanofluids in parabolic dish collectors is still limited and needs further investigation. Only few researchers [70-74] carried out their studies on PD collectors using nanofluids as heat transport medium. The authors concluded to achieve higher efficiency with nanofluids in comparison to other base fluids.

It is difficult to understand the behavior of nanofluids, because of their nature and dramatic changes in their properties at elevated temperatures. The literature results show that the nanofluids has already been explored enough for their possible use in heat transfer applications. However, the application of nanofluids in solar collectors is limited and needs to be explored further in greater depth. Apart from the literature studies, there are concerns need to be addressed and questions need to be answered. Therefore, the idea of the present research is to explore the application of nanofluids further in detail to find the impetus behind the heat transfer enhancement through nanofluids.

2.3 Absorption cooling

2.3.1 Single Effect Absorption Cycle (SEAC)

The vapor absorption cycle has attracted researchers as it does not discharge harmful gasses such as, CO_2, NO, CO etc., which damage the environment. Absorption cycles use heat energy source such as solar or geothermal to produce the necessary heating and cooling which also helps to reduce the peak load demand. Many studies have been performed experimentally as well as theoretically to investigate the absorption cycles driven by solar heat. A single effect (SE) solar absorption cooler of 7 kW cooling ability and about 10% energy efficiency was designed in Singapore [75]. The research conducted by Huang et al. [76] demonstrates that the temperature of generator was reduced by using double effect (DE) absorption cycle (lithium bromide and water) as compared to SE cycle. Studies performed by Li et al. [77] and He et al. [78] describe a 100 kW absorption system which is designed to deliver heating as well as cooling concurrently. The system was designed to save energy significantly as well as to be environment friendly. A SE absorption cooling cycle operated on solar collectors was designed and experimented in Malaysia by Assilzadeh et al. [79]. It was observed that the higher solar irradiation results in producing higher useful energy as well as the higher outlet temperature of the solar collector. On the other hand, increase in inlet temperature of the solar collector decreases the useful energy production and increases cooling load, the higher cooling will have higher COP of the system. Authors believed that countries, such as Malaysia with higher solar radiations, are good for solar assisted absorption cooling systems. Izquierdo et al. [80] performed comparative evaluation of the SE absorption cycle to that of air-cooled cycle, and his findings showed that SE cycle are less economical than the compression air-cooled cycle in case of prime energy and less satisfactory when conventional heat source is used to empower it. The SE absorption chiller using lithium bromide water operated on solar collectors was designed and evaluated by Syed et al. [81]. Their results reveled that system was more consistent in hot and dry environment along with enormous diversity for relative humidity. The comparison was done between SE absorption cycles with water-cooled and DE air-cooled absorption cycle integrated with flat plate collectors by Izquierdo et al. [82]. They witnessed to achieve the condenser temperature of almost 53°C for the latter, however, condensation temperature was just 45 °C for the former one because of the crystallization of the solution. An experimental study on solar assisted SE absorption cycle was conducted by Asdrubali and Grignaffini [83]. Their research showed that COP was maximum when temperature of hot water reached to 70 °C. Performance comparison of different water-ammonia systems with various parameters and conditions were assessed by Engler et al. [84]. Hamad and Audi [85] explored the performance of a continuous, non-storage solar-assisted absorption refrigeration system. The ideal COP of the system was observed to be 1.6, but the actual COP was determined to be 0.55. Haim et al. [86] carried out a theoretical analysis of two different absorption cycles. Both cycles include an evaporator and an absorber. The solar energy concentrates directly on to the generator to concentrate the low concentrated solution. The mathematical equations of the simulated model were examined using computer based software specifically designed for absorption cycles. The operating parameters were calculated using different design aspects. It was concluded that the direct regeneration has higher performance over the indirect ones. Hawlader et al. [87] performed experimental as well as numerical analysis of absorption machine using LiBr-H_2O. Their simulated results were validated with experimental data and they found to be in good agreement with the empirical data. It is witnessed that their experimental efficiency and cooling load was found to be in between 38-67% and 31-72 kW. Ghaddar et al. [88] conducted simulation study of solar operated absorption cycle for Beirut. The results revealed that it requires at least 23m^2 collector area for each ton of cooling and for a water storage of about 1000-1500 L per day upon operating the system solely on solar for 7 hours a day.

2.3.2 Double Effect Absorption Cycles (DEAC)

A comparative study performed between double effect (DE) parallel and series flow lithium-bromide absorption system by Arun et al. [89], their results show that optimal coefficient of performance (COP) attained for first system is greater than the second one. In addition, rate of heat given to the low pressure generator has more effect on parallel system rather than on the series flow system. Gomri [90] studied the capability of three available absorption cooling systems (single, double and triple) to generate chilled water by considering 300 kW cold output for all the systems. The outcome showed that the COP of SE cycle was half as compared to the DE cycle and COP of TE cycle was observed to be 3 times higher than SE absorption cycle. The exergetic evaluation of the different parts of the DE series absorption cycle driven by solar collectors is examined by Ravikumar et al. [91] with the influence of low and high pressure generators. The past research [92] of Gomri was enhanced by him to triple effect absorption cycle by considering the series flow and made the comparison of the outcomes with the single and DE cycles. Integration of a vapor recompression absorber (VRA) with DE absorption chiller, enhanced the flow rate of refrigerant in the circuit to further improve the cooling capacity as demonstrated by Worek et al. [93]. The authors concluded to have achieved higher COP. The exergo-economic assessment of the three types of DE absorption cycles by considering the various parameters and their effects on the COP of the system were assessed by [94]. Results indicated that at greater evaporator and high pressure generator temperatures, lower capital cost was achieved but at a low condensation temperature. Grossman et al. [95] taken in to account different variations to assess them using LiBr-H_2O working pair as the working fluid, he evaluated the different alternatives considering parallel and series flow systems.

Lee and Sheriff [96] performed second law analysis of DE absorption cycles with LiBr-H_2O. The temperature of the cooling production was required to be 7.22 °C and cold water temperature of 29.4-35 °C. Gommed and Grossman [97] performed thermodynamic analysis of single effect as well as of different designs of DE cycles for LiBr-H_2O working pair for various working conditions. Arun et al. [98] evaluated the performance of DE cycle operated on LiBr-H_2O pair, and concluded to have achieved higher COP for the parallel flow in comparison to series flow. Oh et al. [99] performed their analysis on air cooled DE parallel flow absorption heat pump and recommended the optimal range of solution distribution ratio (SDR) to be in between 0.35-0.4 for concentration difference of 4% between inlet and exit of the absorber.

2.3.3 Triple Effect Absorption Cycles (TEAC)

Oouchi et al. [100] performed analysis of three condenser-three desorbers (3C3D) TE cycles, which is an extended form of traditional DE cycle with an evaporator and an absorber to absorb the refrigerant, 3C3Ds recover heat for the lower temperature desorber from the condenser of high temperature. The application of water and ammonia pair to the several versions of three stage system was examined and presented by De Vault and Marsala [101]. They explained that the feasibility of three-condenser system was not justifiable as the ammonia critical point was lower than the condensation temperature. De Vault and Biermann [102] presented analysis of triple cycles similar to 3C3D cycle with double condenser coupling (DCC), where heat is recovered from the hot solution leaving the high temperature condensers (HTCs) and added to the low temperature desorbers (LTDs). The generator with the higher temperature is connected to medium and low temperature side generators, transfers the refrigerant to high temperature condenser (HTC). This arrangement increased heat recovery which in turn enhanced the thermal efficiency of the system. Gomri [103] assessed the exergetic losses which occurs in triple effect cycle. He also evaluated the COP along with exergetic performance of the triple effect cycle. The exergetic performance and the COP was observed to be maximum at higher temperature of low and medium pressure generators. Solar thermal integrated absorption cycle applied for space cooling as well as hydrogen generation was analyzed by Ratlamwala et al. [104] for United Arab Emirates (UAE) conditions. They focused their research on exergetic and energetic efficiencies, hydrogen production rate, COP, influence of photovoltaic collector on electricity generation and average beam radiation of different months. They found that both exergy and energy efficiencies were maximum in March but optimal hydrogen production was achieved in August.

Grossman et al. [105] performed in details, the analysis of triple effect (parallel, series, reverse) cycles using LiBr-H_2O. It is observed in their study that the parallel flow double-condenser coupled alternate (DCCA) cycle has the highest COP of 1.729 at 63% solution concentration and at a high temperature generator (HTG) temperature of 218 °C. The COP can be increased further up to 1.825 upon changing the mass distribution for the generators at the same inlet conditions. Kaita [106] carried out the simulation analysis of triple effect cycles with heat recovery from the high heat refrigerant vapor exiting the LTG. The COP increased further with this new design by

0.03-0.05 at a solution concentration of 59.5%. Sedigh and safari [107] conducted thermodynamic analysis of DCCA and achieved a COP of 1.7 for an absorber and condenser temperature of 35 °C, and at an evaporator temperature of 8 °C and at a generator temperature of 180 °C. The triple effect absorption systems are analyzed extensively by Ratlamwala et al. [108-113] for cooling and heating proposes as well as for hydrogen production using different design parameters. Gomri [114] carried out simulation analysis for single and multistage absorption cooling systems and concluded to achieve the COP of around 1.62-1.9 for series flow TE cycles. The exergy efficiency was also observed to be higher for triple effect cycles in comparison to single and double effect cycles. Some other researchers [115-119] performed thermodynamic analysis of triple effect cycles. It is observed in their analysis that these multistage systems can be compared not only for energy efficiency but also for practicality, economics and environmental aspects. The quadruple effect cycles, which are the extended versions of the triple effect cycles are relatively new and not fully explored. There is not much literature available on quadruple effect cycles. Ratlamwala et al. [120-121] carried out their research on quadruple effect absorption cycles to evaluate their COP along with their exergetic efficiency. The authors used ammonia-water mixture as the working pair and performed energetic and exergetic analysis of the QE cycles. As mentioned earlier that quadruple effect cycle working on LiBr-H_2O has not been studied in earlier research works. Therefore, the present research focuses on to evaluate the performance of quadruple effect cycle using LiBr-H_2O working pair. The quadruple effect cycle along with other cycles will be modelled and analyzed for their energetic and exergetic performance perspective. The mathematical models of the absorptions cycles will be simulated to operate on solar heat. In order to compare the COP of the absorption cycles, the other three (single, double and triple effect) absorption cycles will also be analyzed in the present research.

Chapter 3

DESCRIPTION OF THE SYSTEMS

In this chapter, the description of the systems is described in detail. The structure of the proposed systems is designed to produce useful heat. The useful heat is further used to drive the steam turbines to produce electricity as well as to drive the absorption cooling cycles to provide the cooling effect. The input parameters of the simulated models are varied to fulfil the energy requirements (electricity and cooling production) simultaneously. The system components are simulated using EES software, therefore, the dimensions and sizing of the components are not considered in the analysis. The explanation of the systems will be as follows:

1. The parabolic trough solar collector (PTSC) will be described with the help of schematic diagrams, then it will be integrated with reheat Rankine cycle for power production.
2. The parabolic dish solar collector (PDSC) will be explained in details with the help of schematic diagrams, then it will be integrated with reheat Rankine cycle for power production.
3. The absorption cycles of single, double, triple and quadruple effect assisted on solar collectors will be described comprehensively with the aid of schematic diagrams.

3.1 Parabolic Trough Solar Collector (PTSC)

The PT solar collector shown in Fig. 2 is employed to heat the working fluid flowing inside the receiver tube. Three different heat transfer fluids (HTFs) are used to absorb heat collected by PT solar collector. The HTFs are aluminum oxide (Al_2O_3), ferric oxide (Fe_2O_3) and water. The first two are water based nanofluids. The nanofluids are prepared by mixing different percentages of nanoparticles of Al_2O_3 and Fe_2O_3 in water. Before entering into the solar collector, a pressure pump is used to pressurize the HTFs. The pressurized HTFs would help them stay in liquid form even at higher temperatures. The HTFs enter into the collector at a relatively medium temperature, but attains higher temperature by interacting with the absorber tube. The absorber tube is at the focal line of the parabola of the PT solar collector. The PT solar collector concentrate solar rays on to the receiver tube. The collected energy is being transferred to the heat transfer fluid flowing through the receiver tube. The temperature of the HTF increases and the high temperature HTF exchanges heat with the fluid of the steam cycle (in the boiler) and goes back to the collector to reheat.

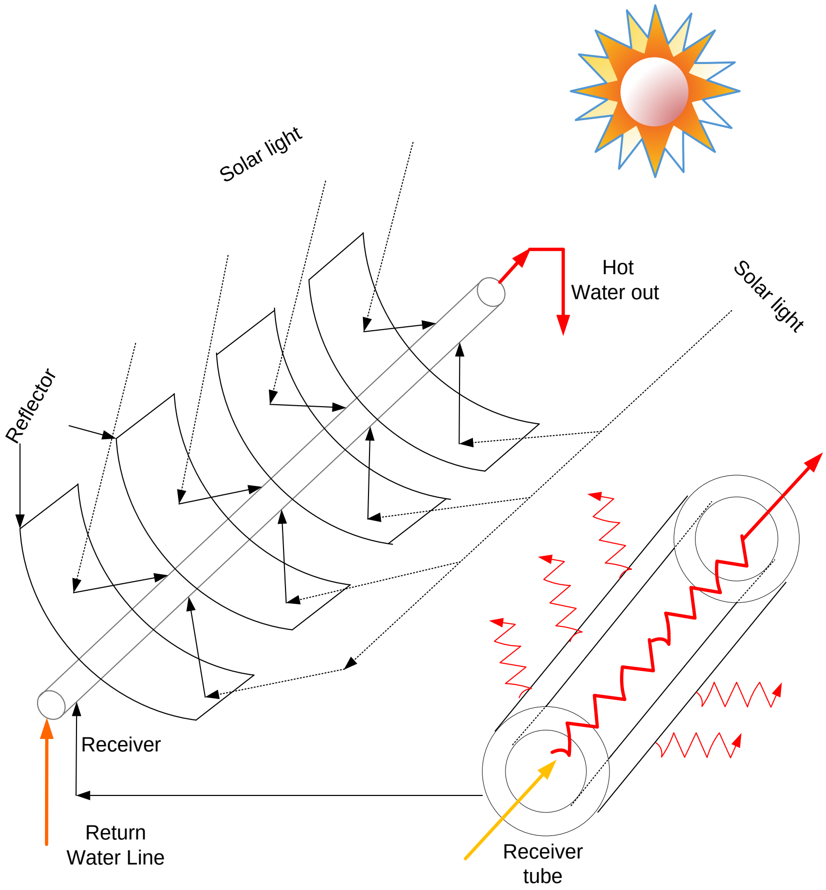

Figure 2: The schematic of the PT solar collector with receiver tube

3.1.1 Integration of parabolic trough collector with reheat Rankine cycle

The parabolic trough (PT) solar collector incorporated with reheat Rankine cycle is described in Fig. 3. The parabolic trough collector reflects the solar rays onto the solar receiver. The receiver then transfers the collected energy to the HTF flowing through it. The HTFs used are Aluminum Oxide (Al_2O_3), Ferric/Iron III Oxide (Fe_2O_3) and water. Aluminum Oxide and Ferric Oxide are nanoparticles mixed in pure/distilled water. At state 16, the high temperature HTF leaves for the boiler of the steam cycle.

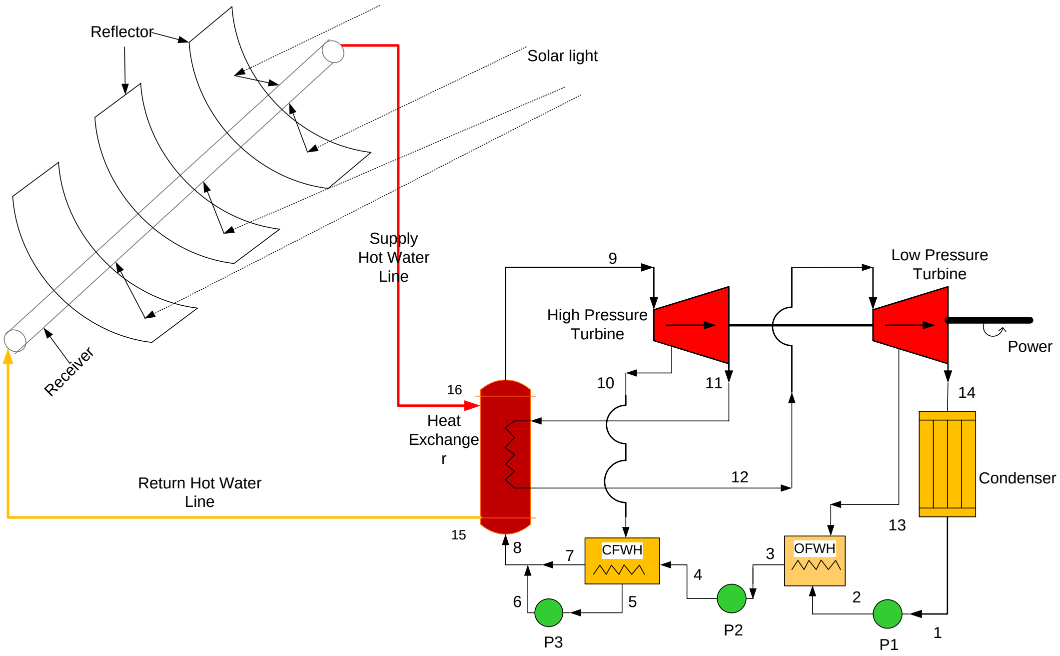

Figure 3: The schematic of the PT solar collector integrated with Rankine cycle

In the boiler, it exchanges heat with the high pressure fluid coming from state 8, and goes back to the solar collector at relatively low temperature at state 15 to get reheated. The superheated vapor generated in the boiler is directed for the main steam turbine at state 9. The steam expands and provides mechanical work at the expense of losing pressure and temperature. A stream of intermediate temperature and pressure taken from the turbine is directed towards the closed feed-water heater (CFWH) at state 10 as well as for the boiler to be reheated at state 11. Steam at state 12 gets reheated at the same temperature as it was on state 9 and heads for the low pressure turbine. It produces power yet again and leaves for the condenser as low grade mixture at state 14. Moderately low grade pressure and lower temperature mixture enters further into the condenser to get cooled. The mixture turns into the saturated liquid and directed towards the pump at state 1. The saturated liquid turns into the compressed liquid by passing through the pump at state 2 and enters into the open feed-water (OFWH). Some relatively medium pressure steam is extracted to feed the open feed-water heater

(OFWH) at state 13. Both streams from state 2 and state 13 get mixed in OFWH, the mixture becomes saturated liquid and enters into the pump 2 at state 3. It turns into the compressed liquid again by pump work and enters into the CFWH at state 4. The feed-water exchanges heat with the steam coming from state 10 and leaves the CFWH at a relatively high temperature at state 7. Steam coming from high pressure turbine at state 10 loses its energy in CFWH and leaves as saturated liquid and enters into the pump 3 at state 5. The saturated liquid gets compressed by pump work at state 6 and mixes with feed-water coming from state 7. Both streams from state 6 and 7 mix together and enter into the boiler of the steam cycle as high pressure fluid at state 8. The compressed liquid gets heated in the boiler with an exchange of heat from solar collectors. The high temperature and high pressure steam then directed towards the turbine to produce power yet again by completing the cycle. The produced power is further connected to the grid to be used for domestic proposes.

3.2 Parabolic dish solar collector

The PD solar collector shown in Fig. 4 is used to generate heat from the solar energy. The heat transfer fluids (HTFs) used are of Al_2O_3 and Fe_2O_3 water based nanofluids and water for the comparison with nanofluids. The nanofluids are prepared by mixing different percentages of nanoparticles of Al_2O_3 and Fe_2O_3 in water. Before entering into the solar collector, the HTFs are compressed with the help of a pump to increase their pressure. The pressurized HTFs would help them stay in liquid form even at greater temperatures. The HTFs enter into the collector at a relatively medium temperature, but temperature of the HTF increases by interacting with the absorber tube. The absorber tube is at the focal point of the parabola of the PD solar collector. The PD collector concentrates the solar rays on to the receiver pipe. The temperature of the receiver pipe gets increased with the help of solar energy. The absorber pipe passes the collected energy in the form of heat to the HTF flowing through it. The temperature of HTF increases and the high temperature HTF heads for the steam cycle boiler to exchange heat with the steam cycle fluid and goes back to the collector to reheat.

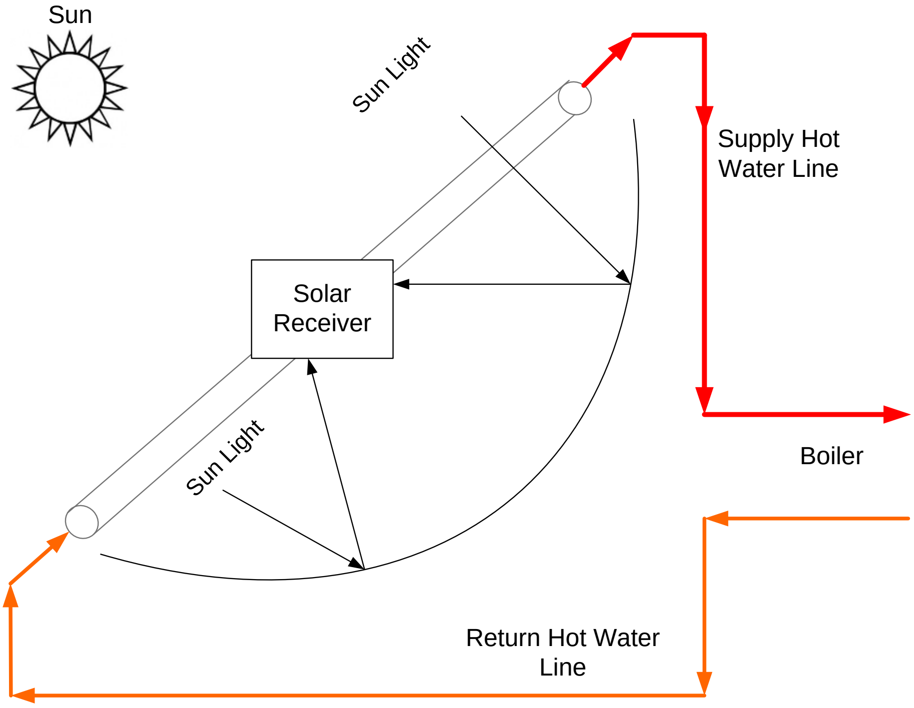

Figure 4: The schematic of the parabolic dish solar collector

3.2.1 Integration of parabolic dish collector with reheat Rankine cycle

The system description of the parabolic dish solar thermal power plant (PDSTPP) is shown in Fig. 5. As a replacement for PT, it is now PD, which is being integrated with steam cycle to produce power. The working principle, heat transfer fluids (HTFs) and state points are kept same for both systems.

Parabolic dish solar collector incorporated with reheat Rankine cycle is described in Fig. 5. The parabolic dish collector reflects solar rays onto the solar receiver. The receiver transfers the collected energy to the HTF flowing through it. The HTFs used are Aluminum Oxide (Al_2O_3), Ferric Oxide (Fe_2O_3) and water. Aluminum Oxide and Ferric Oxide are nanoparticles mixed in pure water. The solar collectors collects the solar energy and transfer it to the HTFs. The high temperature HTF leaves the collector and enters into the boiler of the steam cycle at state 16.

In the boiler, it exchanges heat with the high pressure fluid coming from state 8, and goes back to the solar collector at relatively low temperature at state 15 to get reheated. The superheated vapor generated in boiler is directed for the main steam turbine at state 9. It vapor expands and provides mechanical work at the expense of losing pressure and temperature. A stream of intermediate temperature and pressure taken from the turbine is directed towards the closed feed-water heater (CFWH) at state 10 as well as for the boiler to be reheated at state 11. Steam at state 12 gets reheated at the same temperature as it was on state 9 and heads for the low pressure turbine. It produces power yet again and leaves for the condenser as saturated liquid vapor mixture at state 14. Moderately low pressure and low temperature mixture then enters into the condenser to get cooled. The mixture turns into the saturated liquid and directed towards the pump at state 1. The saturated liquid turns into the compressed liquid by passing through the pump at state 2 and enters into the open feed-water (OFWH). Some relatively medium pressure steam is taken from low pressure turbine to feed the open feed-water heater (OFWH) at state 13. Both streams from state 2 and state 13 get mixed in OFWH and enter into the pump 2 as saturated liquid at state 3. It turns into the compressed liquid again by pump work and enters into the CFWH at state 4. The feed-water exchanges heat with the steam coming from state 10 and leaves the CFWH at a relatively high temperature at state 7. Steam coming from high pressure turbine at state 10 loses its energy in CFWH and leaves as saturated liquid and enters into the pump 3 at state 5. The saturated liquid gets compressed by pump work at state 6 and mixes with feed-water coming from state 7. Both streams from state 6 and 7 mix together and enter into the boiler of the steam cycle as high pressure fluid at state 8. The compressed liquid gets heated in the boiler with an exchange of heat from solar collectors. The high temperature and high pressure steam then directed towards the turbine to produce power yet again by completing the cycle. The produced power is further connected to the grid to be used for domestic proposes.

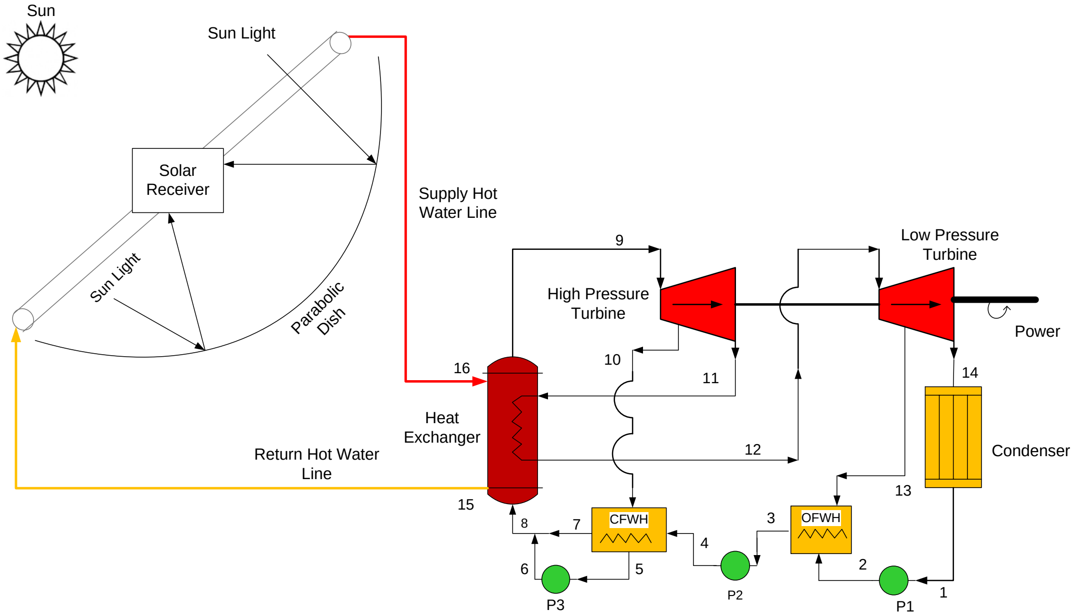

Figure 5: Parabolic dish collector incorporated with steam cycle

3.3 Solar assisted absorption cycles

3.3.1 Single Effect Absorption Cycle (SEAC)

The single effect (SE) cycle shown in Fig. 6, is modelled with a simulation program called EES developed by S.A Klein [122]. In SE cycle, the refrigerant (water) vapour gets separated from the solution (LiBr-H_2O) at a single stage. The vapour refrigerant condenses in the condenser and goes to the evaporator to produce cooling effect.

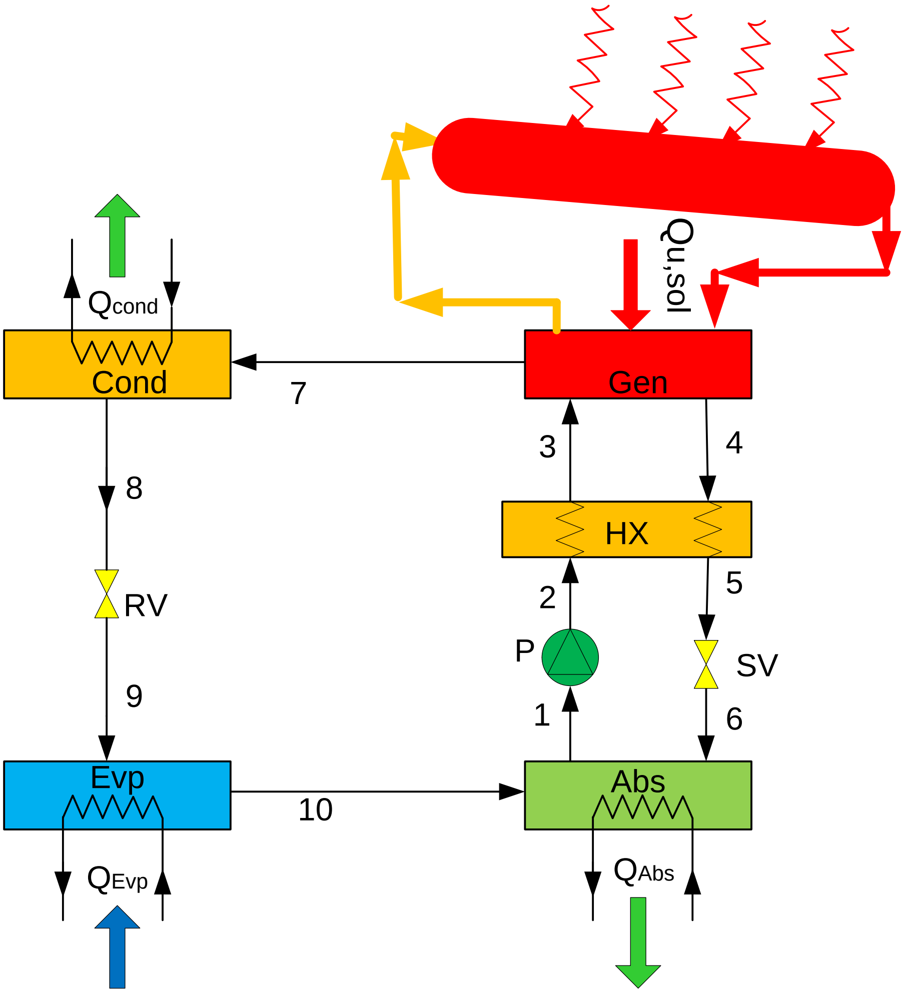

Figure 6: The diagram of the SE absorption cooling cycle

The solution is considered as a weak solution (low percentage of LiBr in water) at states 1, 2, 3 and strong solution (high percentage of LiBr in water) at states 4, 5, 6. At states 7, 8, 9 and 10 there exists only the refrigerant vapour, which is water in this case. The solution having less concentration of $LiBr\text{-}H_2O$ at state 1 enters into the pump and gets compressed to the generator pressure at state 2. It gets heated by passing through the heat exchanger at state 3 and enters into the generator. The solution is being heated in the generator, splitting out the vapour from the solution. The vapour at state 7 goes to the condenser and exchanges heat with cooling water and enters into the refrigerant valve as saturated liquid at state 8. The saturated liquid turns into the saturated liquid vapour mixture by flowing through the refrigerant valve at state 9. The mixture enters into the evaporator and exchanges heat with the outer environment, providing the cooling effect at state 10, and goes to the absorber. The strong solution of LiBr-H_2O from the generator at state 4 leaves for the heat exchanger, it delivers heat to the weak solution entering the heat exchanger and enters into the solution valve at 5. The high concentration solution leaves for the absorber as low grade solution. In the absorber, it absorbs the low grade vapour and cools it down by exchanging heat with the environment. The mixture at state 1 is weak in concentration (LiBr-H_2O) and ready to enter into pump at state 2.

3.3.2 Double Effect Absorption Cycle (DEAC)

The double effect (DE) absorption cycle is analogous to SE cycle. The DE cycle produces vapour in two stages which makes it different from the single effect absorption cycle (SEAC) where the vapour produced at a single stage. The higher vapour production will produce more cooling effect and consequently will have higher coefficient of performance (COP) as compared to SEAC. The working mechanism of DE cycle is displayed in Fig. 7. The distribution of the mass concentration and functioning of the DE cycle is very similar to SE. The assumptions made in modelling the DE cycle are similar to the ones used to design SE cycle. The assumptions made are provided in chapter 4.

The weak solution of LiBr-H_2O at state 1 enters into the pump and gets compressed to the generator pressure at state 2. It gets heated by passing from the low temperature generator (LHE) at state 3. The part of the solution goes to the medium temperature generator (MTG) at state 11 and remaining goes to the high heat exchanger (HHE) at state 12. It gets heated again and goes to the HTG at state 13. The solution boils off in the HTG, splitting the refrigerant from the solution. The refrigerant vapour at state 16 goes to the MTG and exchanges heat with the solution coming from state 11 and enters into the condenser at state 17, where it loses heat to the environment. Another stream of refrigerant from state 7 enters into the condenser. Both streams from state 7 and 18 get mixed and enter into the refrigerant valve as saturated liquid at state 8. The saturated liquid turns into the saturated liquid vapour mixture by passing through the refrigerant valve at state 9. The mixture enters into the evaporator and exchanges heat with the outer environment, providing the cooling effect at state 10, and the low grade vapour forwards to the absorber. The rich concentration solution of LiBr-H_2O leaves for the HHE at state 14. It delivers heat to the weak solution entering the HHE and gets mixed with the rich concentration solution at state 18. Both streams of state 15 and 18 enter into the low heat exchanger (LHE) at state 4. The solution exchanges heat further at the low temperature generator (LTG) and goes to the solution valve at state 5. The low grade solution enters into the absorber at state 6 by passing from the solution valve. In the absorber, it mixes with the low grade vapour. The mixture rejects heat to the outside environment and fully ready to enter into the pump at state 1.

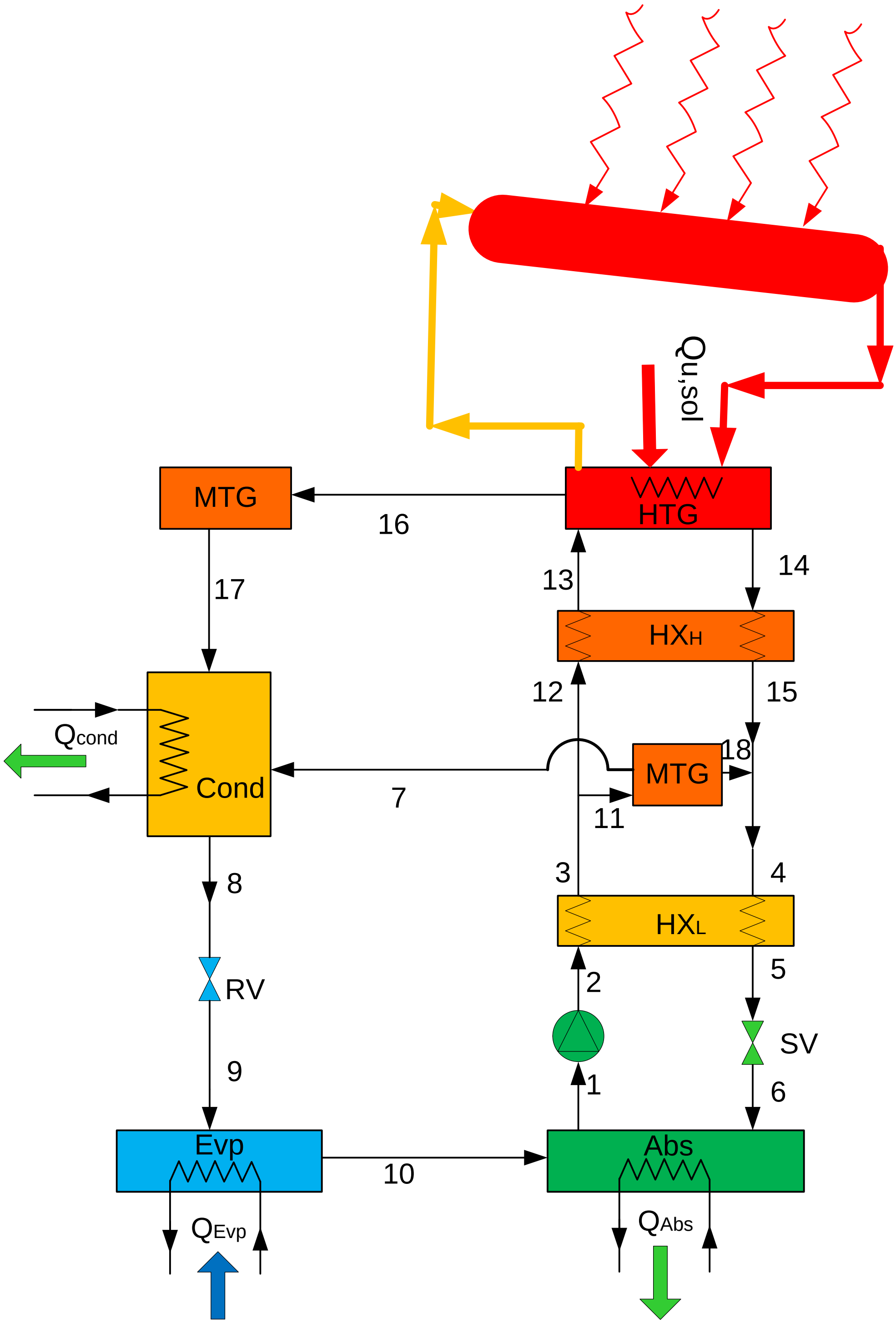

Figure 7: The representation of the double effect absorption cooling cycle

3.3.3 Triple Effect Absorption Cycle (TEAC)

The triple effect (TE) absorption cycle is the extension of the conventional DE cycle. The TE cycle has three generators to produce vapour from the solution. The TE cycle needs higher generator temperature to operate and produces higher cooling effect as compared to DE. The higher the cooling effect, the higher will be the COP. The TE cycle requires less heat input to drive the generator in comparison to SE and DE cycles, but has higher cooling production. The Fig. 8 given below describes the working principle of the TE cycle.

The weak solution of LiBr-H_2O at state 1 enters into the pump and gets compressed to the high temperature generator (HTG) pressure at state 2. It gets heated as it passes over the LHE at state 3. The part of the mixture goes to the LTG at state 4 and remaining goes to the medium heat exchanger (MHE) at state 5. It gets heated in an exchange of heat in MHE at state 6. The part of the solution goes for the MTG at 7 and the remaining heads for the HHE at point 8, where it passes through the HHE at state 9 and into the HTG at state 9. The solution boils off in the HTG with an exchange of heat from the solar energy, which separates the vapour refrigerant out of the solution. The high heat refrigerant vapour at state 19 goes to the MTG, where it exchanges heat with the solution and enters into the LTG at state 20. It gets mixed with the stream of hot refrigerant coming from state 21. Both streams mix together in LTG and provides additional heating to the low temperature solution entering at state 4, and finally enter into the condenser at state 22. Another stream of refrigerant from state 23 enters into the condenser. Both streams from state 22 and 23 get mixed and enter into the refrigerant valve as saturated liquid at state 24. The saturated liquid turns into the saturated liquid vapour mixture by passing through the refrigerant valve at state 25. The mixture enters into the evaporator and exchanges heat with the outer environment, providing the cooling effect at state 26, and leaves for the absorber as low grade refrigerant. It gets absorbed with rich concentration solution. The rich concentration solution of LiBr-H_2O leaves the HTG at state 10 and enters into the HHE. It delivers heat to the less concentration solution entering the HHE and gets mixed with the rich solution coming from state 12. Both streams of state 11 and 12 enter into the MHE at state 13. In the MHE, the rich solution provides extra heating to the poor concentration solution and gets mixed with the high concentration solution coming from state 15. Both streams from state 14 and 15 get mixed together and enter into the LHE at state 16. In the LHE, it transfers heat from strong solution to weak solution and enters into the solution valve at state 5. The low grade solution enters into the absorber by passes over the solution valve at 18. In the absorber, it absorbs the low grade refrigerant and turns into the less concentrated solution at state 1.

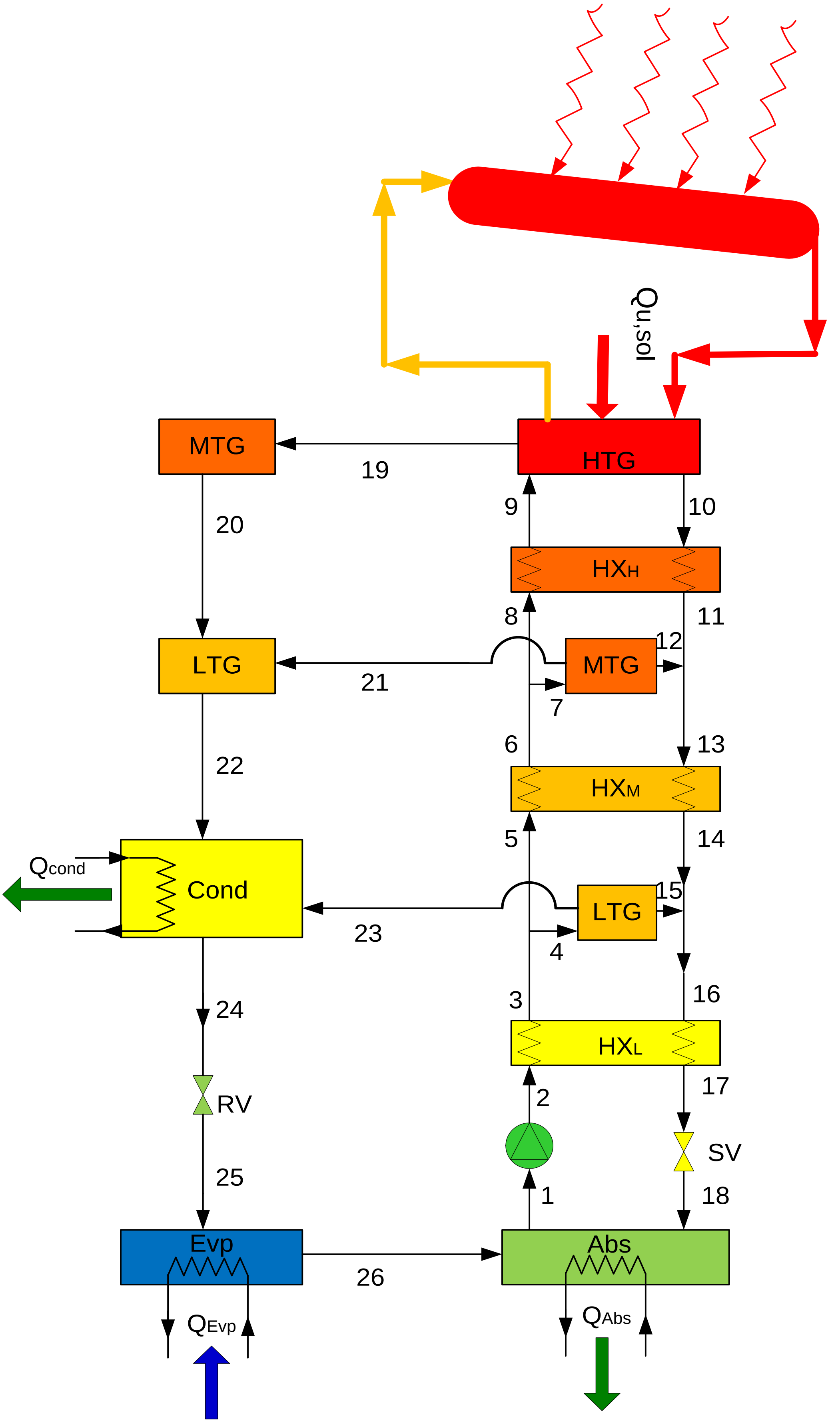

Figure 8: The representation diagram of the triple effect absorption cooling cycle

3.3.4 Quadruple Effect Absorption Cycle (QEAC)

The quadruple effect (QE) absorption cycle along with other cycles is modelled and simulated using the EES software proposed by S. A. Klein [122]. The simulated model of the QE cycle is the extension of the triple effect cycle studied in detail by [105, 106]. The Fig. 9 displays the operational functioning of the QE cycle. The QE cycle requires higher heat source temperatures to work. But requires less heat input as compared to TE cycle. The QE cycle produces vapour in four stages and have the highest cooling effect, consequently, have the highest COP among all the cycles under identical operating conditions.

The weak solution of LiBr-H_2O at state 1 enters into the pump and gets compressed to the very high temperature generator (VHTG) pressure at state 2. It gets heated as it passes over LHE at state 3. The part of the solution goes to the LTG at state 4 and remaining goes to the MHE at state 5. It gets heated in an exchange of heat in MHE at state 6. The part of the solution goes for the MTG at 7 and the remaining heads for the HHE at state 8, where it passes through the HHE at state 9. The part of the solution is fed to the HTG and remaining enters into the very high heat exchanger (VHHE) at state 11. The solution gets heated in an exchange of heat in the VHHE and enters into the VHTG at state 12. The solution boils off in the VHTG with an exchange of heat from the solar energy, extracting the vapour out from the fluid. The vapour at state 25 goes to the HTG and provides additional heating to help the solution to evaporate and produce more vapour at state 10 and leaves for the MTG at state 26, where it gets mixed with the stream of refrigerant coming from state 27. In MTG, both streams offer heating aid again to produce more vapour at state 7 and enter into the LTG at state 28. It gets mixed with the refrigerant stream coming from state 29 and enters into the LTG to help produce vapour yet again at state 4. After an exchange of heat in the LTG the refrigerant inters into the condenser at state 30. Another stream of refrigerant from state 31 enters into the condenser, where it gets cooled by losing heat to the environment. Then finally, the refrigerant enters into the refrigerant valve as saturated liquid at state 32. The saturated liquid turns into the saturated liquid vapour mixture by passing through the refrigerant valve at state 33. The mixture enters into the evaporator and exchanges heat with the outer environment, providing the cooling effect at state 34, and low grade refrigerant enters into the absorber. The rich concentrating solution of LiBr-H_2O leaves the VHTG at state 13 and enters into the VHHE, where it delivers heat to the less concentrated solution entering the VHHE and at state 14 gets mixed with the rich concentration solution coming from state 15. Both streams of state 14 and 15 enter into the HHE at state 16. The solution exchanges heat in the HHE and gets mixed with the rich solution of state 18. Both streams from state 17 and 18 get mixed together and enter into the MHE at state 19. It loses heat to the low concentration solution entering the MHE and gets mixed with the rich solution coming from 21. Both streams of state 20 and 21 get mixed together and enter into the LHE, where it exchanges heat yet again and enters into the solution valve at state 23. The low grade rich solution finally enters into the absorber by passing from the solution valve at state 24. In the absorber, it absorbs the low grade refrigerant and turns into the less concentrated solution at state 1.

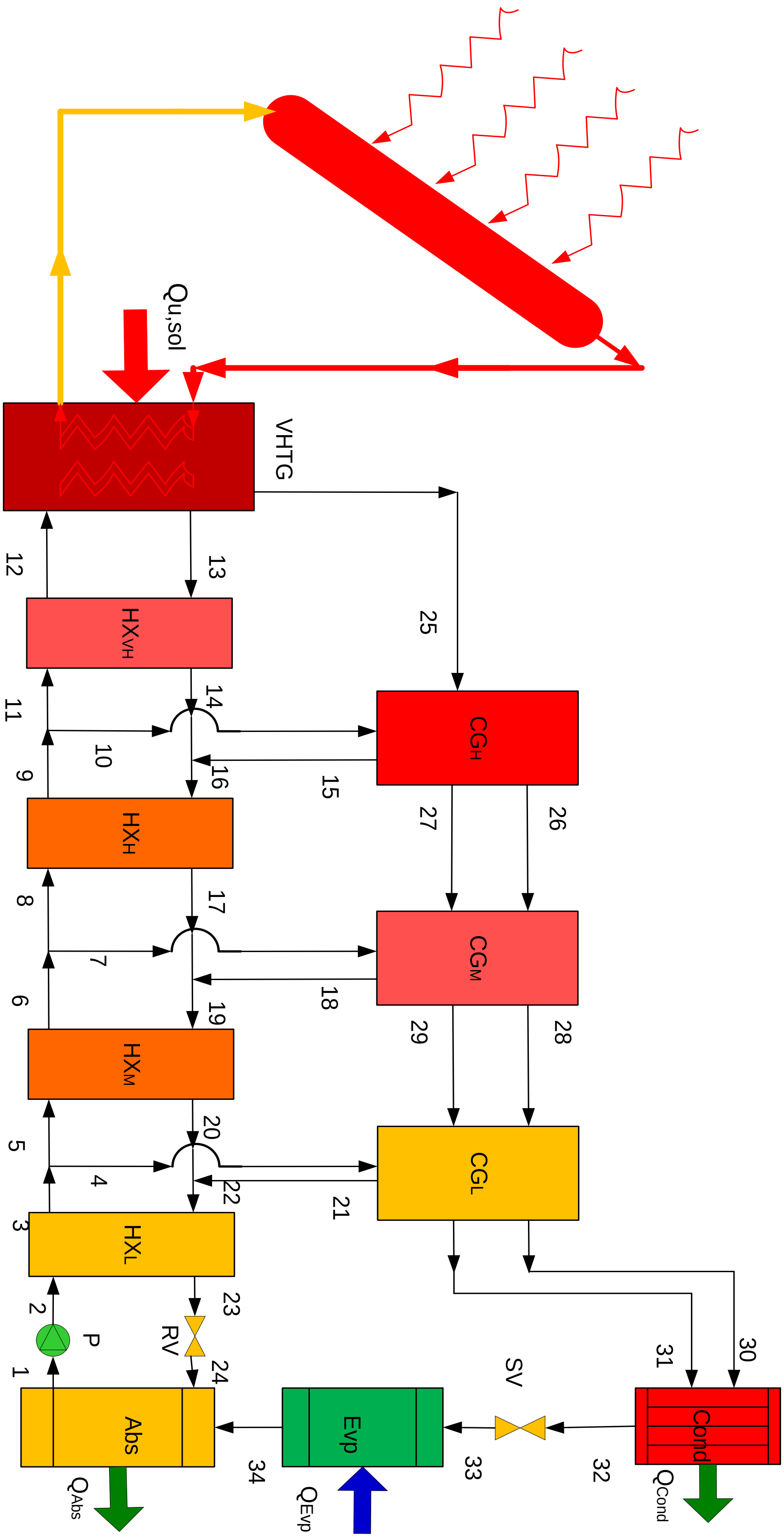

Figure 9: The flow diagram of the quadruple effect absorption cooling cycle

Chapter 4

ANALYSIS OF SOLAR ASSISTED POWER GENERATION AND MULTI-EFFECT ABSORPTION COOLING SYSTEMS

This chapter explains in detail the methodology applied to carry out the research of the proposed study. The mathematical models of solar collectors and the integrated systems are explained as follow.

1. Parabolic trough solar collectors
    1. Energy analysis of PTSC
    2. Exergy analysis of PTSC
    3. Entropy analysis of PTSC
2. Parabolic dish solar collectors
    1. Energy analysis of PDSC
    2. Exergy analysis of PDSC
    3. Entropy Analysis of PDSC
3. Reheat Rankine cycle
    1. Energy balance
    2. Entropy balance
    3. Exergy balance
4. Absorption cooling systems
    1. Single effect absorption cycle

        i. Energy and mass balance
        ii. Exergy balance
    2. Double effect absorption cycle
        i. Energy and mass balance
        ii. Exergy balance
    3. Triple effect absorption cycle
        i. Energy balance
        ii. Exergy balance
    4. Quadruple effect absorption cycle
        i. Energy and mass balance
        ii. Exergy balance
    5. Entropy balance of Absorption cycles
5. Assumptions and design parameters
    1. Design parameters and assumption made in analyzing the solar collectors
    2. Design conditions and assumption made in analyzing the absorption cycles

4.1 The parabolic trough solar collector

The model of the parabolic trough (PT) solar collector is examined using the relevant mathematical equations. The PT solar collector is adopted from the model presented by Kalogirou [123] and F.A. Suleiman [56]. The parameters of the reference model are altered according to the design conditions (to fulfil the useful energy requirements). The heat transfer fluids (HTFs) used in the present work are Al_2O_3 and Fe_2O_3 water based nanofluids. The equations used to solve the PT solar collector model are presented in this section.

4.1.1 Energy Analysis

The collector receiver and aperture area is defined as

$$A_{re} = \pi . D_{r,0} . L \tag{4.1}$$

The aperture area of the collector is calculated as

$$A_{ap} = \left(W - D_{c,o}\right) . L \tag{4.2}$$

where $D_{r,o}$ is receiver outer diameter W is width and L is length of the collector. To find out the wind flow outside the solar receiver, and to find the wind convection coefficient, it is necessary to first determine the Reynolds number which is calculated as proposed by Kalogirou S. A. [123]

$$R_e = \frac{\rho . V . D_{c,o}}{\mu} \tag{4.3}$$

where $D_{c,o}$, V, μ and ρ represent outer diameter of glass cover of the evacuated tube, velocity, dynamic viscosity and density of air outside the collector.

The Reynolds number provides an idea of the flow regime, according to the results, the Reynolds number is found to be 25347 which is in the turbulent region and the N_u is determined by applying the relevant turbulent flow formula proposed by Kalogirou S.A. [123].

$$N_u = 0.3 . {R_e}^{0.6} \tag{4.4}$$

To find out the overall heat transfer coefficient (U_0) and the collector losses (U_L), it is necessary to first calculate the heat transfer coefficients inside and outside the solar collector. The heat convection coefficient from the glass cover to the outer environment, also known as wind convection coefficient is determined as proposed by Kalogirou S. A. [123].

$$h_{c,ca} = N_u \cdot \frac{k_{air}}{D_{c,o}} \tag{4.5}$$

The radiation heat transfer coefficient from the glass cover to the ambient is to be calculated as

$$h_{r,ca} = \varepsilon_{cv} \,.\, \sigma \,.\, (T_c + T_o).(T_c \,.\, T_c + T_o \,.\, T_o) \tag{4.6}$$

where ε_{cv} represents glass cover emissivity.

The radiation heat transfer coefficient from the glass to the receiver is estimated as proposed by Kalogirou S. A. [123]

$$h_{r,cr} = \frac{\sigma.\left(T_c+T_{r,av}\right) \,.\, \left(T_c.T_c + T_{r,av} \,.\, T_{r,av}\right)}{\frac{1}{\epsilon_r}+\frac{A_r}{A_c} \,.\, \left[\frac{1}{\varepsilon_{cv}}-1\right]} \tag{4.7}$$

where σ, T_c and $T_{r,av}$ represent Boltzmann's constant, glass cover temperature and average temperature respectively. The collector loss coefficient is determined using the approach proposed by [101] as

$$U_L = \left[\frac{A_r}{A_c \,.\left(h_{c,ca}+h_{r,ca}\right)} + \frac{1}{h_{r,cr}}\right]^{-1} \tag{4.8}$$

The heat removal factor is calculated as proposed by [123]

$$F_r = \frac{\dot{m}_r \,.\, C_p}{A_r \,.\, U_L} \,.\left[1 - exp\left(-\frac{A_r \,.\, U_L \,.\, F_1}{\dot{m}_r \,.\, C_p}\right)\right] \tag{4.9}$$

where $\dot{m}_r$ is collector flow rate, C_p represents heat capacity of the HTF. The glass cover temperature which was assumed earlier, can be rechecked using the following equation

$$T_{c,avg} = \frac{h_{r,cr} \,.\, T_{r,av} + \frac{A_c}{A_r} + \left(h_{c,ca}+h_{r,ca}\right).\, T_0}{h_{r,cr} + \frac{A_c}{A_r} \,.\, \left(h_{c,ca}+h_{r,ca}\right)} \tag{4.10}$$

where T_0 represents the environmental temperature.

Useful energy can be calculated as proposed by Duffie and Beckman [124]

$$\dot{Q}_g = F_r \,.\, [S \,.\, A_{ap} - A_r \,.\, U_L \,.\left(T_{r,i} - T_0\right)] \tag{4.11a}$$

where S, A_{ap}, represents absorbed solar radiation.

The rate of heat transfer is determined as

$$\dot{Q}_{prod} = \frac{\dot{Q}_g}{1000} \quad (4.11b)$$

To convert the units from W to kW the equation is divided by 1000.

The available rate of solar heat is determined as

$$\dot{Q}_{solar} = \frac{F_r \,.\, A_{ap} \,.\, S}{1000} \quad (4.12)$$

The collector's overall heat transfer coefficient is estimated using the formula proposed by Kalogirou S.A. [123], is given as

$$U_0 = \left[\frac{1}{U_L} + \frac{D_{r,0}}{h_{c,r,in} \,.\, D_{r,i}} + \frac{D_{r,0}}{2.\, k_r} \,.\, \ln(\frac{D_{r,0}}{D_{r,i}})\right]^{-1} \quad (4.13)$$

where k_r represents thermal conductivity of the receiver tube.

The energetic efficiency of PT solar collector is determined from the equations proposed by Duffie and Beckman [124], is given as

$$\eta_{en,PTSC} = F_r \,.\left[\eta_r - U_L \,.\, (\frac{T_{r,i} - T_0}{G_b . C})\right] \quad (4.14)$$

4.1.2 Exergy Analysis

The exergetic analysis is executed to estimate the real potential of the PT solar collector. The exergy of the solar collector and solar rays is calculated using the energy produced by solar collector and the available solar energy. The thermal heat exergy of the collector is defined as

$$\dot{E}x_{col} = \left(1 - \frac{T_0}{T_{avg}}\right). \dot{Q}_{prod} \quad (4.15a)$$

The available solar exergy is calculated as

$$\dot{E}x_{sol} = \left(1 - \frac{T_0}{T_{sun}}\right). \dot{Q}_{sol} \quad (4.15b)$$

The exergetic efficiency of PT collector is to be determined as proposed by Ratlamwala et al. [125]

$$\eta_{ex,PTSC} = \frac{\dot{E}x_{col}}{\dot{E}x_{solar}} \quad (4.16)$$

where η_r, G_b and C, represent receiver efficiency, solar irradiation and concentration ratio respectively.

4.1.3 Entropy Analysis

To maximize the output of the solar collector, it is necessary to minimize the entropy generation in the system. The entropy generation is linked to the exergy flow through the collector. The entropy generation is the product of exergy destroyed of the collector and the ambient temperature. The exergy destroyed is the difference of the exergy coming and going out of the collector.

$$\dot{E}x_{des} = \dot{E}x_{sol} - \dot{E}x_{col} \tag{4.17}$$

The entropy generation in PTSC is described as

$$\dot{S}_{gen} = \frac{\dot{E}x_{des}}{T_0} \tag{4.18}$$

4.2 Parabolic dish solar collector

The equations used to model the PT collector are very similar to the PT collector. The parabolic dish collector model studied in our analysis is derived from the model presented by Lloyd C. Ngo, [67].

4.2.1 Energy analysis

The aperture area of the solar collector and solar receiver (cylindrical receiver) area is described as

$$A_{ap} = \pi . R^2 \tag{4.19}$$

$$A_r = \frac{\pi . d^2}{4} \tag{4.20}$$

where, R represents the radius of the aperture and d represents the diameter of the receiver. The concentration ratio between aperture and the receiver areas of the collector and is calculated as

$$C = \frac{A_{ap}}{A_r} \tag{4.21}$$

The heat loss through the collector is calculated in the rate form as proposed by [67]

$$Q_l = U_l . A_r (T_r - T_0) \tag{4.22}$$

where U_L represent the collector loss coefficient, which is calculated from equation (4.8).

The useful heat delivered by solar collector is defined as

$$Q_u = \dot{m} C_p (T_{out} - T_{in}) \tag{4.23}$$

The famous Hottel-Whillier [67] relation is applied to calculate heat gain as

$$Q_u = F_r \, A_{ap} . \left[S - \frac{A_r}{A_{ap}} \, U_L \, . (T_{in} - T_0) \right] \tag{4.24}$$

Where S is the absorbed radiation, and it calculated as ($S = \eta_0 . G_b$), η_0 is the optical efficiency of the PD collector, which is supposed as 0.85 [20]. T_0 is the environmental temperature and F_r is the factor of heat removal of the collector which is calculated as

$$F_r = \frac{\dot{m} C_p}{A_r U_L} [1 - \exp(\frac{A_r . U_L . F}{\dot{m} C_p})] \tag{4.25}$$

where, F is the ratio between U_0 and U_L.

The energetic efficiency of the PD collector is computed using the relation proposed by [124].

$$\eta_{en,PDSC} = F_r \, . \left[\eta_r - \; U_L \, . (\frac{T_{r,i} - T_0}{G_b . C}) \right] \tag{4.26}$$

4.2.2 Exergy Analysis

The exergetic analysis of PD collector is performed to find out the maximum possible work potential, the PD solar collector can generate. The exergy is calculated at the collector as well as the available exergy of solar heat. To find out the total exergetic content (exergy destroyed) of the collector, we need to first estimate the exergy coming and exergy going out of the collector.

$$\dot{E}_{x_{in}} = \dot{m}.C_p(T_{in} - T_0 - T_0.\ln(T_{in} - T_0)) \tag{4.27a}$$

$$\dot{E}_{x_{out}} = \dot{m}.C_p(T_{out} - T_0 - T_0.\ln(T_{out} - T_0)) \tag{4.27b}$$

$$\dot{E}_{x_{total}} = \dot{E}_{x_{out}} - \dot{E}_{x_{in}} \tag{4.28}$$

The total exergetic content of the solar is calculated as

$$\dot{E}_{x_{sol}} = G_b.A_{ap}.\eta_{pe} \tag{4.29}$$

where η_{pe} the Patella's efficiency is calculated as proposed by [126]

$$\eta_{pe} = 1 - \frac{4T_0}{3T_s} + \frac{1}{3}\left(\frac{T_0}{T_s}\right)^4 \tag{4.30}$$

The exergetic efficiency of the PD collector is the ratio of the total exergy output of the system to the total exergy available of the solar, it is calculated as

$$\eta_{ex,PDSC} = \frac{\dot{E}_{x,total}}{\dot{E}_{x,sol}} \tag{4.31}$$

where $\dot{E}x_{sol}$ represents the available rate of solar exergy.

4.2.3 Entropy Analysis

The entropy balance for PDSC is similar to the PTSC. The exergy destroyed of PDSC is described in equation 4.28 and the product of equation 4.28 and ambient temperature results in defining the entropy generation in the system.

$$\dot{S}_{gen} = \frac{\dot{E}x_{total}}{T_0} \tag{4.32}$$

4.3 Reheat Rankine cycle

The reheat Rankine cycle employed in the present research is the revised version of the model proposed by [127]. The steam cycle is evaluated for its energetic and exergetic viewpoints, and to find the net total work produced by the steam cycle. The Rankine cycle is further combined with solar collectors to supply the required heat to the boiler of the steam cycle (Rankine cycle). The energy equations used to solve the thermodynamic model of the steam cycle are given below.

4.3.1 Energy Equations

First of all the enthalpies values are calculated at each stage of the cycle. The turbines used in the analysis are considered to be adiabatic. Based on enthalpies, the efficiency of both turbines is calculated as.

$$\eta_{hpt} = \frac{h_9 - h_{10}}{h_9 - h_{s,10}} \tag{4.33}$$

$$\eta_{lpt} = \frac{h_{12} - h_{13}}{h_{12} - h_{s,13}} \tag{4.34}$$

where h_{12} and h_{13} represent enthalpy values at state 12 and 13.

There are four pumps used to circulate and pressurize the working fluid. All the pumps are considered to be adiabatic. The work input and the rate of work input estimated as below

$$w_{p1,in} = V_1 \left[\frac{P_{ofwh} - P_{cond}}{\eta_p}\right] \tag{4.35}$$

$$\dot{W}_{p1,in} = \dot{m}_1 \,.\, w_{p1,in} \tag{4.36}$$

where V, p_{ofwh}, p_{cond}, η_p and $\dot{m}_1$ represent specific volume, open feed water heater pressure, condenser pressure pump efficiency and flow rate of the collector. The power produced and the work produced rate of turbines is calculated as

$$w_{T,out,high} = x.(h_9 - h_{10}) + z.(h_9 - h_{11}) \tag{4.37}$$

$$w_{T,out,low} = m\,.(h_{12} - h_{13}) + n\,.(h_{12} - h_{14}) \tag{4.38}$$

$$\dot{W}_{T,out,high} = \dot{m}_{10}\,.(h_9 - h_{10}) + \dot{m}_{11}\,.(h_9 - h_{11}) \tag{4.39}$$

$$\dot{W}_{T,out,low} = \dot{m}_{13}\,.(h_{12} - h_{13}) + \dot{m}_{14}.(h_{12} - h_{14}) \tag{4.40}$$

where $\dot{m}_{14}$ is flow rate at state 14 and h_{14} represent enthalpy of the fluid at state 14, and x, y, z, m, n are fractions of steam respectively. The heat input is the heat provided to the boiler can be determined as

$$q_{in} = h_9 - h_8 + z\,.(h_{12} - h_{11}) \tag{4.41}$$

Heat rejected of the condenser is calculated as

$$q_{out} = n\,.\,(h_{14} - h_1) \tag{4.42}$$

The heat rate of the boiler and the condenser is defined as

$$\dot{Q}_b = \dot{m}_9\,.\,(h_9 - h_8) + \dot{m}_{11}\,.\,(h_{12} - h_{11}) \tag{4.43}$$

$$\dot{Q}_c = \dot{m}_{14}\,.\,(h_{14} - h_1) \tag{4.44}$$

The total work output of the Rankine cycle is determined to be

$$\dot{W}_{net} = \dot{W}_{T,out,high} + \dot{W}_{T,out,low} - (\dot{W}_{p1,in} + \dot{W}_{p2,in} + \dot{W}_{p3,in}) \tag{4.45}$$

The productivity of the steam generation is calculated as

$$\eta_{en,st} = \frac{\dot{W}_{net}}{\dot{Q}_b} \tag{4.46}$$

where $\dot{Q}_b$ represents the boiler heat rate.

The global energetic efficiency of the integrated system is calculated as

$$\eta_{en,ov} = \frac{\dot{W}_{net}}{\dot{Q}_{solar}} \tag{4.47}$$

where $\dot{Q}_{solar}$ represents heat rate of the solar.

4.3.2 Entropy Balance

Molecular disorder of the thermodynamic systems is called entropy. The entropy cannot be destroyed, but only be transferred to or from the system. The entropy at each state point of the system is calculated to estimate the total entropy of the combined cycle. The entropy balance of a thermodynamic system is defined as proposed by [128]

$$S_{in} - S_{out} + S_{gen} = \Delta S_{sys} \tag{4.48}$$

The ΔS_{sys} of the overall system is then determined as

$$\Delta S_{sys} = S_2 - S_1 \tag{4.49}$$

The entropy in the rate form is defined as

$$\dot{S}_{in} - \dot{S}_{out} + \dot{S}_{gen} = {}^{dS}\!/_{dt} \tag{4.50}$$

4.3.3 Exergy analysis

The exergy analysis are performed by calculating exergy values at every individual point of the integrated system. The exergy input, exergy output and exergy destroyed are calculated using the exergies found at every point and the exergy is defined as

$$E_x = (h - h_0) - T_0(s - s_0) \tag{4.51}$$

where h_o, T_o and s_o represent the reference values of the environment. The general rate form of exergy is calculated as

$$\dot{X}_{in} - \dot{X}_{out} - \dot{X}_{des} = \frac{dX_{sys}}{dt} \tag{4.52}$$

The exergetic performance of the Rankine cycle is estimated by calculating the incoming, outgoing and exergetic contents destroyed at each point of the cycle. Exergy values are calculated at all points to compute the exergy destroyed by each component of the system. Exergy destruction of the pumps used in the cycle is expressed as

$$\dot{E}x_1 + \dot{W}_{p1,in} = \dot{E}x_2 + \dot{E}x_{dest,p1} \tag{4.53}$$

$$\dot{E}x_3 + \dot{W}_{p2,in} = \dot{E}x_4 + \dot{E}x_{dest,p2} \tag{4.54}$$

$$\dot{E}x_5 + \dot{W}_{p3,in} = \dot{E}x_6 + \dot{E}x_{dest,p3} \tag{4.55}$$

where $\dot{E}x_1$ and $\dot{E}x_{dest,p1}$ represent exergy destroyed by state 1 and exergy destroyed by pump 1 respectively. The exergy destroyed by pump 3 and pump 4 can be calculated the same way. The exergy destruction of high and low pressure turbines is determined as

$$\dot{E}x_9 = \dot{E}x_{10} + \dot{E}x_{11} + \dot{E}x_{dest,hpt} \tag{4.56}$$

$$\dot{E}x_{12} = \dot{E}x_{13} + \dot{E}x_{14} + \dot{E}x_{dest,lpt} \tag{4.57}$$

where $\dot{E}x_{dest,hpt}$ and $\dot{E}x_{dest,lpt}$ represent exergy destroyed by HPT and exergy destroyed by LPT respectively. The lost work potential of boiler and condenser can be computed the same way as turbines, and it is calculated as

$$\dot{E}x_8 + \dot{E}x_{11} + \dot{E}x_{th,b} = \dot{E}x_9 + \dot{E}x_{12} + \dot{E}x_{dest,b} \tag{4.58}$$

$$\dot{E}x_{14} = \dot{E}x_1 + \dot{E}x_{th,c} + \dot{E}x_{dest,c} \tag{4.59}$$

where $\dot{E}x_{dest,b}$ and $\dot{E}x_{dest,c}$ represent exergy destroyed by boiler and condenser. The exergy destruction of open and closed feed water heaters is computed as

$$\dot{E}x_{dest,ofwh} = \dot{E}x_2 + \dot{E}x_{13} - \dot{E}x_3 \tag{4.60a}$$

$$\dot{E}x_{dest,cfwh} = \dot{E}x_4 + \dot{E}x_{10} - \dot{E}x_5 - \dot{E}x_7 \tag{4.60b}$$

The rate of heat exergy of the boiler is calculated as

$$\dot{E}x_{th,b} = \left[1 - \frac{T_0}{T_b}\right] . \dot{Q}_b \tag{4.61}$$

where T_b represents the temperature of boiler, the rate at which exergy transfer of the condenser is calculated the same way. The accessible rate of solar exergy is expressed as

$$\dot{E}x_{solar} = \left[1 - \frac{T_0}{T_s}\right] . \dot{Q}_{solar} \tag{4.62}$$

where T_s represents the temperature of the sun.

The exergy efficiency of steam cycle is calculated as

$$\eta_{ex,st} = \frac{\dot{W}_{net}}{\dot{E}x_{th,b}} \tag{4.63}$$

Where $\dot{E}x_{th,b}$ represents the heat exergy provided to the boiler. The overall exergy efficiency of the system is calculated as

$$\eta_{ex,ov} = \frac{\dot{W}_{net}}{\dot{E}x_{solar}} \tag{4.64}$$

4.4 Absorption Cycles

4.4.1 Single Effect Absorption Cycle

4.4.1.1 Energy and mass conversion

The constituents of the single effect (SE) cycle are modelled individually, and are explained with the help of equations.

Absorber:

The mass and energy balance around the absorber is defined as

$$\dot{m}_1 = \dot{m}_6 + \dot{m}_{10} \tag{4.65}$$

and

$$\dot{Q}_{abs} = \dot{m}_6 h_6 + \dot{m}_{10} h_{10} - \dot{m}_1 h_1 \tag{4.66}$$

Condenser:

Mass and energy conversion for the condenser is calculated as

$$\dot{m}_7 = \dot{m}_8 \tag{4.67}$$

and

$$\dot{Q}_{con} = \dot{m}_7 (h_7 - h_8) \tag{4.68}$$

Evaporator:

The mass and energy balance of the evaporator is determined as

$$\dot{m}_9 = \dot{m}_{10} \tag{4.69}$$

and

$$\dot{Q}_{evp} = \dot{m}_9 (h_{10} - h_9) \tag{4.70}$$

Generator:

The mass balance on the generator is

$$\dot{m}_3 = \dot{m}_4 + \dot{m}_7 \tag{4.71}$$

The energy balance on the generator is

$$\dot{Q}_{gen} = \dot{m}_4 h_4 + \dot{m}_7 h_7 - \dot{m}_3 h_3 \tag{4.72}$$

Heat Exchanger:

The mass and energy balance around the heat exchanger is determined as

$$\dot{m}_2 + \dot{m}_4 = \dot{m}_3 + \dot{m}_5 \tag{4.73}$$

and

$$\dot{Q}_{HE} = \dot{m}_2 h_2 + \dot{m}_4 h_4 - \dot{m}_3 h_3 - \dot{m}_6 h_6 \tag{4.74}$$

The COP of the SE cycle is calculated as

$$COP_{en} = \frac{\dot{Q}_e}{\dot{Q}_g + \dot{W}_p} \tag{4.75}$$

4.4.1.2 Exergy balance

The exergy vales are calculated at each state point of the SE cycle. The heat exergy and exergy destroyed are computed using exergy found at every individual point and the exergy is defined as

$$E_x = (h - h_0) - T_0(s - s_0) \tag{4.76}$$

where h_o, T_o and s_o represent the reference values of the environment. The general rate form of exergy is calculated as

$$\dot{X}_{in} - \dot{X}_{out} - \dot{X}_{des} = \frac{dX_{sys}}{dt} \tag{4.77}$$

Thermal exergy and the exergy destroyed by every constituent of the SE cycle is found as given below

Absorber:

$$\dot{E}_{x_{th,a}} = \left(1 - \frac{T_0}{T_1}\right) . \dot{Q}_a \tag{4.78}$$

$$\dot{E}_{x_{des,a}} = \dot{E}_x[10] + \dot{E}_x[6] - \dot{E}_{x_{th,a}} - \dot{E}_x[1] \tag{4.79}$$

Condenser:

$$\dot{E}_{x_{th,C}} = \left(1 - \frac{T_0}{T_8}\right) . \dot{Q}_C \tag{4.80}$$

$$\dot{E}_{x_{des,c}} = \dot{E}_x[7] - \dot{E}_{x_{th,c}} - \dot{E}_x[8] \tag{4.81}$$

Evaporator:

$$\dot{E}_{x_{th,e}} = \left(1 - \frac{T_0}{T_{10}}\right) . \dot{Q}_e \tag{4.82}$$

$$\dot{E}_{x_{des,e}} = \dot{E}_x[9] + \dot{E}_{x_{th,e}} - \dot{E}_x[10] \tag{4.83}$$

Generator:

$$\dot{E}_{x_{th,g}} = \left(1 - \frac{T_0}{T_4}\right) . \dot{Q}_g \tag{4.84}$$

$$\dot{E}x_{des,g} = \dot{E}_x[3] + \dot{E}_x[7] + \dot{E}x_{th,g} - \dot{E}_x[4] \tag{4.85}$$

Heat Exchanger:

$$\dot{E}x_{des,HE} = (\dot{E}_x[2] + \dot{E}_x[4]) - (\dot{E}_x[5] + \dot{E}_x[3]) \tag{4.86}$$

Pump:

$$\dot{E}x_{des,p} = \dot{E}_x[1] + \dot{W}_p - \dot{E}_x[2] \tag{4.87}$$

The Exergetic performance of the SE cycle is evaluated as

$$\eta_{ex} = \frac{\dot{E}x_{th,e}}{\dot{E}x_{th,g} + \dot{W}_p} \tag{4.88}$$

4.4.2 Double Effect Absorption Cycle

4.4.2.1 Energy and mass balance

The energy equations used to model the double effect (DE) absorption cycle are presented in this section. The general energy equations are similar to the ones used in SE, but with different state points.

Absorber:

The mass and energy balance around the absorber is defined as

$$\dot{m}_1 = \dot{m}_6 + \dot{m}_{10} \tag{4.89}$$

and

$$\dot{Q}_{abs} = \dot{m}_6 h_6 + \dot{m}_{10} h_{10} - \dot{m}_1 h_1 \tag{4.90}$$

Condenser:

Mass and energy conversion for the condenser is calculated as

$$\dot{m}_8 = \dot{m}_7 + \dot{m}_{17} \tag{4.91}$$

and

$$\dot{Q}_{con} = \dot{m}_7 h_7 + \dot{m}_{17} h_{17} - \dot{m}_8 h_8 \tag{5.92}$$

Medium Temperature Generator (MTG):

Mass and energy balance for MTG is calculated as

$$\dot{m}_{11} = \dot{m}_7 + \dot{m}_{18} \tag{4.93}$$

$$\dot{m}_{16} = \dot{m}_{17} \tag{4.94}$$

and

$$\dot{Q}_{MTG} = \dot{m}_7 h_7 + \dot{m}_{18} h_{18} - \dot{m}_{11} h_{11} \tag{4.95}$$

$$\dot{Q}_{MTG} = \dot{m}_{16}(h_{16} - h_{17}) \tag{4.96}$$

Evaporator:

The mass and energy balance for the evaporator is determined as

$$\dot{m}_9 = \dot{m}_{10} \tag{4.97}$$

and

$$\dot{Q}_{evp} = \dot{m}_9(h_{10} - h_9) \tag{4.98}$$

Generator:

The mass balance on the generator is

$$\dot{m}_{13} = \dot{m}_{14} + \dot{m}_{16} \tag{4.99}$$

The energy balance on the generator is

$$\dot{Q}_{gen} = \dot{m}_{14} h_{14} + \dot{m}_{16} h_{16} - \dot{m}_{13} h_{13} \tag{4.100}$$

High Heat Exchanger (HHE):

The mass and energy balance around HHE is determined as

$$\dot{m}_{12} + \dot{m}_{14} = \dot{m}_{13} + \dot{m}_{15} \tag{4.101}$$

and

$$\dot{Q}_{HHE} = \dot{m}_{12} h_{12} + \dot{m}_{14} h_{14} - \dot{m}_{13} h_{13} - \dot{m}_{15} h_{15} \tag{4.102}$$

Low Heat Exchanger (LHE):

The mass and energy balance around LHE is calculated as

$$\dot{m}_2 + \dot{m}_4 = \dot{m}_3 + \dot{m}_5 \tag{4.103}$$

and

$$\dot{Q}_{LHE} = \dot{m}_2 h_2 + \dot{m}_4 h_4 - \dot{m}_3 h_3 - \dot{m}_6 h_6 \tag{4.104}$$

Finally, the COP of the DE cycle is calculated as

$$COP_{en} = \frac{\dot{Q}_e}{\dot{Q}_g + \dot{W}_p} \tag{4.105}$$

4.4.2.2 Exergy balance

To find the exergetic performance of the DE cycle, we need to find the exergy at each state point. The heat exergy and exergetic content destroyed of the DE cycle is estimated using exergy values found at every individual point.

Absorber:

$$\dot{E}_{x_{th,a}} = \left(1 - \frac{T_0}{T_1}\right) . \dot{Q}_a \tag{4.106}$$

$$\dot{E}_{x_{des,a}} = \dot{E}_x[10] + \dot{E}_x[6] - \dot{E}_{x_{th,a}} - \dot{E}_x[1] \tag{4.107}$$

Condenser:

$$\dot{E}_{x_{th,C}} = \left(1 - \frac{T_0}{T_8}\right) . \dot{Q}_C \tag{4.108}$$

$$\dot{E}_{x_{des,c}} = \dot{E}_x[7] + \dot{E}_x[17] - \dot{E}_{x_{th,c}} - \dot{E}_x[8] \tag{4.109}$$

Evaporator:

$$\dot{E}_{x_{th,e}} = \left(1 - \frac{T_0}{T_{10}}\right) . \dot{Q}_e \tag{4.110}$$

$$\dot{E}_{x_{des,e}} = \dot{E}_x[9] + \dot{E}_{x_{th,e}} - \dot{E}_x[10] \tag{4.111}$$

Generator:

$$\dot{E}_{x_{th,g}} = \left(1 - \frac{T_0}{T_{14}}\right) . \dot{Q}_g \tag{4.112}$$

$$\dot{E}_{x_{des,g}} = \dot{E}_x[13] - \dot{E}_x[16] + \dot{E}_{x_{th,g}} - \dot{E}_x[14] \tag{4.113}$$

Medium Temperature Generator:

$$\dot{E}_{x_{th,mtg}} = \left(1 - \frac{T_0}{T_7}\right) . \dot{Q}_{ltg} \tag{4.114}$$

$$\dot{E}_{x_{des,mtg}} = \dot{E}_x[11] - \dot{E}_x[18] + \dot{E}_{x_{th,ltg}} - \dot{E}_x[7] \tag{4.115}$$

High Heat Exchanger:

$$\dot{E}x_{des,HHE} = \dot{E}_x[12] + \dot{E}_x[14] - \dot{E}_x[5] - \dot{E}_x[13] \quad (4.116)$$

Low Heat Exchanger:

$$\dot{E}x_{des,LHE} = (\dot{E}_x[2] + \dot{E}_x[4]) - (\dot{E}_x[5] + \dot{E}_x[3]) \quad (4.117)$$

Pump:

$$\dot{E}x_{des,p} = \dot{E}_x[1] + \dot{W}_p - \dot{E}_x[2] \quad (4.118)$$

The Exergetic performance of the DE cycle is estimated as

$$\eta_{ex} = \frac{\dot{E}x_{th,e}}{\dot{E}x_{th,g} + \dot{W}_p} \quad (4.119)$$

4.4.3 Triple Effect Absorption Cycle

4.4.3.1 Energy and mass balance

The analytical model the triple effect (TE) absorption cycle is solved using energy equations presented in this section. The mathematical equations are similar to the ones used in DE, but with different state points. The mathematical model of TE cycle is solved using the equations given below.

Absorber:

$$\dot{m}_1 = \dot{m}_{18} + \dot{m}_{26} \quad (4.120)$$

$$\dot{Q}_{abs} = \dot{m}_{18}h_{18} + \dot{m}_{26}h_{26} - \dot{m}_1h_1 \quad (4.121)$$

Condenser:

$$\dot{m}_{24} = \dot{m}_{22} + \dot{m}_{23} \quad (4.122)$$

$$\dot{Q}_{con} = \dot{m}_{22}h_{22} + \dot{m}_{23}h_{23} - \dot{m}_{24}h_{24} \quad (4.123)$$

LTG:

$$\dot{m}_4 = \dot{m}_{15} + \dot{m}_{23} \quad (4.124)$$

$$\dot{m}_{22} = \dot{m}_{20} + \dot{m}_{21} \quad (4.125)$$

$$\dot{Q}_{LTG} = \dot{m}_{15}h_{15} + \dot{m}_{23}h_{23} - \dot{m}_4h_4 \quad (4.126)$$

$$\dot{Q}_{LTG} = \dot{m}_{20}h_{20} + \dot{m}_{21}h_{21} - \dot{m}_{22}h_{22} \quad (4.127)$$

MTG:

$$\dot{m}_7 = \dot{m}_{12} + \dot{m}_{21} \quad (4.128)$$

$$\dot{m}_{19} = \dot{m}_{20} \quad (4.129)$$

$$\dot{Q}_{MTG} = \dot{m}_{12}h_{12} + \dot{m}_{21}h_{21} - \dot{m}_7h_7 \quad (4.130)$$

$$\dot{Q}_{MTG} = \dot{m}_{19}(h_{19} - h_{20}) \quad (4.131)$$

HTG:

$$\dot{m}_9 = \dot{m}_{10} + \dot{m}_{19} \quad (4.132)$$

$$\dot{Q}_{HTG} = \dot{m}_{10}h_{10} + \dot{m}_{19}h_{19} - \dot{m}_9h_9 \quad (4.133)$$

Evaporator:

$$\dot{m}_{25} = \dot{m}_{26} \quad (4.134)$$

$$\dot{Q}_{evp} = \dot{m}_{25}(h_{26} - h_{25}) \quad (4.135)$$

LHE:

$$\dot{m}_2 + \dot{m}_{16} = \dot{m}_3 + \dot{m}_{17} \quad (4.136)$$

$$\dot{Q}_{LHE} = \dot{m}_2h_2 + \dot{m}_{16}h_{16} - \dot{m}_3h_3 - \dot{m}_{17}h_{17} \quad (4.137)$$

MHE:

$$\dot{m}_5 + \dot{m}_{13} = \dot{m}_6 + \dot{m}_{14} \quad (4.138)$$

$$\dot{Q}_{MHE} = \dot{m}_5h_5 + \dot{m}_{13}h_{13} - \dot{m}_6h_6 - \dot{m}_{14}h_{14} \quad (4.139)$$

HHE:

$$\dot{m}_8 + \dot{m}_{10} = \dot{m}_9 + \dot{m}_{11} \quad (4.140)$$

$$\dot{Q}_{HHE} = \dot{m}_8h_8 + \dot{m}_{10}h_{10} - \dot{m}_9h_9 - \dot{m}_{11}h_{11} \quad (4.141)$$

Finally, the COP of the TE cycle is calculated as

$$COP_{en} = \frac{\dot{Q}_e}{\dot{Q}_g + \dot{W}_p} \quad (4.142)$$

4.4.3.2 Exergy balance

The heat exergy and the exergy destroyed by each component of the TE cycle is presented below

Absorber:

$$\dot{E}_{x_{th,a}} = \left(1 - \frac{T_0}{T_1}\right). \dot{Q}_a \tag{4.143}$$

$$\dot{E}_{x_{des,a}} = \dot{E}_x[18] + \dot{E}_x[26] - \dot{E}_{x_{th,a}} - \dot{E}_x[1] \tag{4.144}$$

Condenser:

$$\dot{E}_{x_{th,C}} = \left(1 - \frac{T_0}{T_{24}}\right). \dot{Q}_C \tag{4.145}$$

$$\dot{E}_{x_{des,c}} = \dot{E}_x[22] + \dot{E}_x[23] - \dot{E}_{x_{th,c}} - \dot{E}_x[24] \tag{4.146}$$

Evaporator:

$$\dot{E}_{x_{th,e}} = \left(1 - \frac{T_0}{T_{26}}\right). \dot{Q}_e \tag{4.147}$$

$$\dot{E}_{x_{des,e}} = \dot{E}_x[25] + \dot{E}_{x_{th,e}} - \dot{E}_x[26] \tag{4.148}$$

High Temperature Generator:

$$\dot{E}_{x_{th,htg}} = \left(1 - \frac{T_0}{T_{19}}\right). \dot{Q}_{htg} \tag{4.149}$$

$$\dot{E}_{x_{des,htg}} = \dot{E}_x[9] - \dot{E}_x[10] + \dot{E}_{x_{th,htg}} - \dot{E}_x[19] \tag{4.150}$$

Medium Temperature Generator:

$$\dot{E}_{x_{th,mtg}} = \dot{E}_x[19] - \dot{E}_x[20] \tag{4.151}$$

$$\dot{E}_{x_{des,mtg}} = \dot{E}_x[7] - \dot{E}_x[12] + \dot{E}_{x_{th,mtg}} - \dot{E}_x[21] \tag{4.152}$$

Low Temperature Generator:

$$\dot{E}_{x_{th,ltg}} = \dot{E}_x[20] + \dot{E}_x[21] - \dot{E}_x[22] \tag{4.153}$$

$$\dot{E}_{x_{des,ltg}} = \dot{E}_x[5] - \dot{E}_x[15] + \dot{E}_{x_{th,ltg}} - \dot{E}_x[23] \tag{4.154}$$

High Heat Exchanger:

$$\dot{E}_{x_{des,HHE}} = \dot{E}_x[10] + \dot{E}_x[8] - \dot{E}_x[9] - \dot{E}_x[11] \quad (4.155)$$

Medium Heat Exchanger:

$$\dot{E}_{x_{des,MHE}} = \dot{E}_x[5] + \dot{E}_x[13] - \dot{E}_x[6] - \dot{E}_x[14] \quad (4.156)$$

Low Heat Exchanger:

$$\dot{E}_{x_{des,LHE}} = \dot{E}_x[2] + \dot{E}_x[16] - \dot{E}_x[3] - \dot{E}_x[17] \quad (4.157)$$

Pump:

$$\dot{E}_{x_{des,p}} = \dot{E}_x[1] + \dot{W}_p - \dot{E}_x[2] \quad (4.158)$$

The Exergetic efficiency of the TE cycle is defined as

$$\eta_{ex} = \frac{\dot{E}_{x_{th,e}}}{\dot{E}_{x_{th,g}} + \dot{W}_p} \quad (4.159)$$

4.4.4 Quadruple Effect Absorption Cycle

The mathematical model of the quadruple effect (QE) is solved using the equations presented in this section.

4.4.4.1 Mass and energy balance

The law of conservation of mass includes the mass conversion of the total mass as well as the concentration of the material used in the solution. The mass and concentration equations for steady state system are given as,

$$\sum \dot{m}_i - \sum \dot{m}_o = 0 \quad (4.160)$$

$$\sum \dot{m}_i . x_i - \sum \dot{m}_o . x_o = 0 \quad (4.161)$$

Where *m* is the mass at each state point and *x* is the solution concentration. The mass distribution among the components of the system is provided in schematic diagrams in chapter 3. The concentration of the low and high solution is calculated at each state point using the above equation. Energy balance at every part of the QE cycle is found out by applying the first law of thermodynamics.

$$(\sum \dot{m}_i . h_i - \dot{m}_0 . h_0) + (\sum Q_i - \sum Q_o) + W = 0 \quad (4.162)$$

The energy analysis is performed for every part of the QE cycle. They are described as follow.

Absorber:

$$\dot{Q}_{abs} = \dot{m}_{24}.h_{24} + \dot{m}_{34}.h_{34} - \dot{m}_{1}.h_{1} \qquad (4.163)$$

Condenser:

$$\dot{Q}_{con} = \dot{m}_{31}.h_{31} + \dot{m}_{30}.h_{30} - \dot{m}_{32}.h_{32} \qquad (4.164)$$

Evaporator:

$$\dot{Q}_{evp} = \dot{m}_{33}(h_{34} - h_{33}) \qquad (4.165)$$

VHTG:

$$\dot{Q}_{VHTG} = \dot{m}_{13}.h_{13} + \dot{m}_{25}.h_{25} - \dot{m}_{12}.h_{12} \qquad (4.166)$$

HTG:

$$\dot{Q}_{HTG} = \dot{m}_{15}.h_{15} + \dot{m}_{27}.h_{27} - \dot{m}_{10}.h_{10} \qquad (4.167)$$

$$\dot{Q}_{HTG} = \dot{m}_{25}(h_{25} - h_{26}) \qquad (4.168)$$

MTG:

$$\dot{Q}_{MTG} = \dot{m}_{18}.h_{18} + \dot{m}_{29}.h_{29} - \dot{m}_{7}.h_{7} \qquad (4.170)$$

$$\dot{Q}_{MTG} = \dot{m}_{26}.h_{26} + \dot{m}_{27}.h_{27} - \dot{m}_{28}.h_{28} \qquad (4.171)$$

LTG:

$$\dot{Q}_{LTG} = \dot{m}_{21}.h_{21} + \dot{m}_{31}.h_{31} - \dot{m}_{4}.h_{4} \qquad (4.172)$$

$$\dot{Q}_{LTG} = \dot{m}_{22}.h_{22} + \dot{m}_{29}.h_{29} - \dot{m}_{30}.h_{30} \qquad (4.173)$$

LHE:

$$\eta_{LHE} = \frac{(T_{22} - T_{23})}{(T_{22} - T_{2})} \qquad (4.174)$$

MHE:

$$\eta_{MHE} = \frac{(T_{19} - T_{20})}{(T_{19} - T_{5})} \qquad (4.175)$$

HHE:

$$\eta_{HHE} = \frac{(T_{16} - T_{17})}{(T_{16} - T_8)} \tag{4.176}$$

VHHE:

$$\eta_{VHHE} = \frac{(T_{13} - T_{14})}{(T_{13} - T_{11})} \tag{4.177}$$

The COP, is the ratio of the chilled water production, to that of the solar heat supplied to the VHTG of the QEAC and the pumping power required

$$COP = \frac{\dot{Q}_{evp}}{\dot{Q}_{VHTG} + \dot{W}_P} \tag{4.178}$$

The energy equations of the SE, DE and TE cycles are solved in a similar way as of quadruple effect cycle to calculate the COP.

4.4.4.2 Exergy balance

The exergetic evaluation of the absorption cycles is performed by calculating the exergy at every individual part of the system. The total exergy change which occurs between the systems components is determined as

$$\dot{E}_{des} = \sum_j \left(1 - \frac{T_0}{T_j}\right) . Q_j + \left(\sum_i m_i . e_{xi}\right)_{in} - \left(\sum_i m_i . e_{xi}\right)_{out} - W \tag{4.179}$$

where, $\dot{E}_{des}$, T0, T_j and e_x represent the exergy destruction between the system components, ambient temperature, heat source temperature and specific exergy respectively. The exergy at any specific point of the system is estimated as,

$$e_x = (h - h_0) - T_0(s - s_0) \tag{4.180}$$

where the subscript 0 in the above equations is for the reference values, i.e, ambient environment. The heat exergy and the exergy destroyed by each component of the QE cycle is presented below.

Absorber:

$$\dot{E}_{x_{th,a}} = \left(1 - \frac{T_0}{T_1}\right) . \dot{Q}_a \tag{4.181}$$

$$\dot{E}_{x_{des,a}} = \dot{E}_x[34] + \dot{E}_x[24] - \dot{E}_{x_{th,a}} - \dot{E}_x[1] \tag{4.182}$$

Condenser:

$$\dot{E}_{x_{th,C}} = \left(1 - \frac{T_0}{T_{32}}\right).\dot{Q}_C \tag{4.183}$$

$$\dot{E}_{x_{des,c}} = \dot{E}_x[30] + \dot{E}_x[31] - \dot{E}_{x_{th,c}} - \dot{E}_x[32] \tag{4.184}$$

Evaporator:

$$\dot{E}_{x_{th,e}} = \left(1 - \frac{T_0}{T_{34}}\right).\dot{Q}_e \tag{4.185}$$

$$\dot{E}_{x_{des,e}} = \dot{E}_x[33] + \dot{E}_{x_{th,e}} - \dot{E}_x[34] \tag{4.186}$$

Very High Temperature Generator:

$$\dot{E}_{x_{th,vhtg}} = \left(1 - \frac{T_0}{T_{13}}\right).\dot{Q}_{vhtg} \tag{4.187}$$

$$\dot{E}_{x_{des,vhtg}} = \dot{E}_x[12] - \dot{E}_x[13] + \dot{E}_{x_{th,vhtg}} - \dot{E}_x[25] \tag{4.188}$$

High Temperature Generator:

$$\dot{E}_{x_{th,htg}} = \left(1 - \frac{T_0}{T_{15}}\right).\dot{Q}_{htg} \tag{4.189}$$

$$\dot{E}_{x_{des,htg}} = \dot{E}_x[10] - \dot{E}_x[15] + \dot{E}_{x_{th,htg}} - \dot{E}_x[27] \tag{4.190}$$

Medium Temperature Generator:

$$\dot{E}_{x_{th,mtg}} = \left(1 - \frac{T_0}{T_{18}}\right).\dot{Q}_{mtg} \tag{4.191}$$

$$\dot{E}_{x_{des,mtg}} = \dot{E}_x[7] - \dot{E}_x[18] + \dot{E}_{x_{th,mtg}} - \dot{E}_x[29] \tag{4.192}$$

Low Temperature Generator:

$$\dot{E}_{x_{th,ltg}} = \left(1 - \frac{T_0}{T_{21}}\right).\dot{Q}_{ltg} \tag{4.193}$$

$$\dot{E}_{x_{des,ltg}} = \dot{E}_x[4] - \dot{E}_x[21] + \dot{E}_{x_{th,ltg}} - \dot{E}_x[31] \tag{4.194}$$

Very High Heat Exchanger:

$$\dot{E}_{x_{des,VHHE}} = \dot{E}_x[11] + \dot{E}_x[13] - \dot{E}_x[12] - \dot{E}_x[14] \tag{4.195}$$

High Heat Exchanger:

$$\dot{E}_{x_{des,HHE}} = \dot{E}_x[16] + \dot{E}_x[8] - \dot{E}_x[9] - \dot{E}_x[17] \quad (4.196)$$

Medium Heat Exchanger:

$$\dot{E}_{x_{des,MHE}} = \dot{E}_x[5] + \dot{E}_x[19] - \dot{E}_x[6] - \dot{E}_x[20] \quad (4.197)$$

Low Heat Exchanger:

$$\dot{E}_{x_{des,LHE}} = \dot{E}_x[2] + \dot{E}_x[22] - \dot{E}_x[3] - \dot{E}_x[23] \quad (4.198)$$

Pump:

$$\dot{E}_{x_{des,p}} = \dot{E}_x[1] + \dot{W}_p - \dot{E}_x[2] \quad (4.199)$$

Finally the exergetic efficiency of the QEAC is calculated as,

$$\eta_{ex} = \frac{\dot{E}_{th,evp}}{\dot{E}_{th,VHTG} + \dot{W}_p} \quad (4.200)$$

The exergy analysis described above can also be used for other absorption cycles.

4.4.5 Entropy Balance

The general entropy balance around each component of the absorption cycle is calculated as follow

$$0 = \sum \dot{m}_i S_i - \sum \dot{m}_e S_e + \dot{S}_{gen,k} \quad (4.201)$$

where k represents any component of the system. The rate of entropy generation is calculated using the product of exergy destroyed and ambient temperature and is calculated as

$$\dot{S}_{gen,k} = \frac{\dot{E}_{x_{des}}}{T_0} \quad (4.202)$$

The same approach is used to calculate the entropy balance of all the absorption cycles.

4.5 Assumptions and design parameters

4.5.1 Assumptions and design parameters used in analyzing the solar collectors

Table 1: Design parameters and assumptions made in analyzing the solar collectors

Parameter	Symbol	Unit	Value	

			Parabolic trough	**Parabolic dish**	
Aperture area	A_{ap}	m^2	50.27	50.27	Fixed
Receiver area	A_{re}	m^2	4.712	0.071	Fixed
Ambient temperature	T_0	K	300	300	Variable
Ambient Pressure	P_0	kPa	100	100	Fixed
Sun temperature	T_s	K	5600	5600	Fixed
Inlet temperature of the solar receiver	T_{in}	K	350	350	Fixed
Outlet temperature	T_{out}	K	-------	------	Variable
Solar radiation	G_b	W/m^2	900	900	Variable
Concentration ratio	C	------	10.66	1600	Variable
Mass flow rate	$\dot{m}$	Kg/s	0.01	0.01	variable
Optical efficiency	η_0	------	0.85[124]	0.85[129]	Fixed
Specific heat capacity	C_p	J/kg.K	-------	--------	Variable
Collector efficiency factor	F'	-----	0.9 [123]	0.9 [129]	Fixed
Overall heat loss coefficient	U_L	$W/m^2.K$	-------	--------	Variable
Tracking	-----	------	E-W [101, 124]	Two axis [67]	

In order to do the parametric analysis, the parameters are varied individually to observe their effect on the performance parameters, such as, useful energy. The tracking of the collectors was not considered in the simulations.

4.5.2. Design conditions and Assumptions made in analyzing the absorption cycles

The assumptions considered to carry out the simulation analysis of SE, DE, TE and QE absorption cycles are as follows,

- The system is supposed to be at steady state.
- The heat loses are ignored except the prescribed ones.
- Pressure loses in pipes and fittings are not considered
- The refrigerant is saturated liquid at the exit of the condenser.
- The refrigerant is saturated vapour at the exit of the evaporator.
- The enthalpy is supposed to be same at both ends of the valves.
- The temperature of the vapour at the exit of the generators is at the mean temperature of the solution ($T25= (T13+T12)/2$, in case of QEAC) for all four absorption cycles as proposed by [130].
- The condenser and absorbers reject heat to the environment.
- The solution is considered as week solution (52.25% LiBr) at the absorber exit and strong solution at the generator exit (57% LiBr) as proposed by [131].
- The ambient pressure and temperature are supposed to be 100 kPa and 300 K.
- The system produces chilled water.

Chapter 5

Methodology for Preparing the Nanofluids

5.1 Preparation of nanofluids

This chapter discusses in details the properties and preparation of nanofluids. The nanoparticles of aluminum oxide and ferric oxide powder are procured from US-Nano research materials [132]. The following are the properties of the nanoparticles at ambient conditions.

The Al_2O_3 nanoparticles are 99+% pure, particle size of 20 nm, white color powder, spherical shaped, having the specific heat capacity of 880 j/kg K and density of 3890 kg/m^3. The Fe_2O_3 nanoparticles are 98+% pure, particle size of 20-40 nm, red brown color, spherical in shape and the bulk density of 5240 kg/m^3 [132]. The nanoparticles used to make suspensions of nanofluids are shown in the Fig. 10 given below. The nanoparticles of Al_2O_3 and Fe_2O_3 nano-powder are selected to be mixed with pure water to prepare the nanofluids. They are selected on the basis of their availability to be purchased as well as their preparation methods are well defined in the literature. Since their thermophysical properties and affinity to water is high, they have been used in many literature studies. They have already been explored numerically as well as experimentally [36], therefore, they are selected to be analyzed in the present research too.

Figure 10: Nanoparticles of Al_2O_3 and Fe_2O_3 in the form of nano powder

The nanofluids are prepared by mixing of nanoparticles in distilled water. Different percentage of nanoparticles are suspended in base fluids to make the nanofluids. Initially 0.5 weight percent nanoparticles are mixed in distilled water. The nanoparticles of Al_2O_3 are dispersed slowly in distilled/pure water with a continuous stirring to achieve the batter stability. The solutions are prepared with and without the surfactant TritonX-100. The surfactant TritonX-100 is used as the surfactant agent to increase the stability of nanofluids. In order to get the homogenous solution, one drop of TritonX-100 is added for each milliliter of the solution as proposed by different researchers [36]. The TritonX-100 purchased from Uni-Chem chemicals, is shown in the Fig. 11.

Figure 11: The surfactant TritonX-100 used in preparation of nanofluids

After 2 hours of continuous stirring, the nanofluids are then kept in ultrasonic mixture for 8 hours at a frequency of 100-140 Hz [36]. The continuous sonication for 8 hours made a very stable suspension of particles in base fluids of water. The prepared nanofluids are shown in the Fig. 12 given below. The same approach is applied to prepare Fe_2O_3 nanofluids. Finally, the water based Al_2O_3 and Fe_2O_3 nanofluids are tested in parabolic trough solar collector.

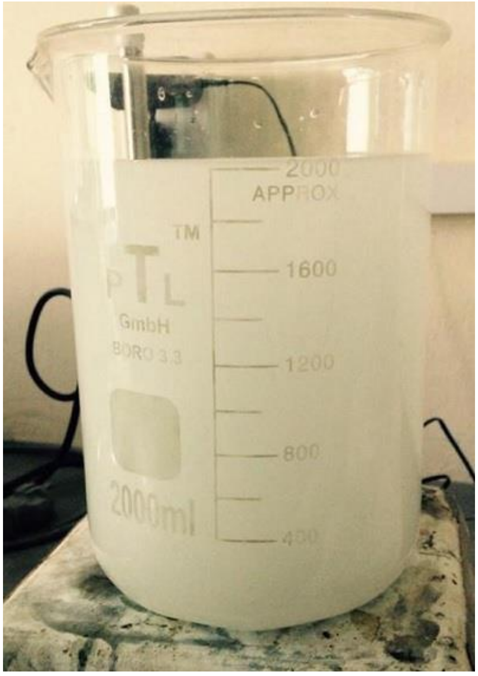

Figure 12: The Al_2O_3 nanoparticles suspended in base fluids of pure water

5.2 Properties of nanofluids

In order to identify the heat transfer enhancement through nanofluids, it is necessary to first evaluate the thermophysical properties of nanofluids, such as, thermal conductivity, density, viscosity and specific heat capacity which needs to be calculated at design conditions. The C_p of the nanofluids is determined as using the correlation recommended by Khanfer and Vafai [133]

$$C_{p,nf} = C_{p,np}(\varphi_{np}) + C_{p,bf}(1 - \varphi_{np}) \tag{5.1}$$

where C_{pbf} and φ_{np} represent specific heat capacity of base fluid and percentage of nanoparticles in the base fluids. The density of the nanofluids is determined as proposed by Ayatollahi et al. [134]

$$\rho_{nf} = \rho_{bf}(1 - \varphi_{np}) + \rho_{np}.\varphi_{np} \tag{5.2}$$

where ρ_{np} and ρ_{bf} are density of nanoparticles and density of base fluids.

Different researchers have used different correlations to find the thermal conductivity of the nanofluids, the thermal conductivity equation proposed by Maxwell [135, 136] is given as

$$k_{nf} = \frac{k_{np}+2k_{bf}-2(k_{np}-k_{bf})\varphi_{np}}{k_{np}+2k_{bf}-(k_{np}-k_{bf})\varphi_{np}} k_{bf} \tag{5.3}$$

where k_{nf}, k_{np}, k_{bf} are thermal conductivity of nanofluids, nanoparticles and base fluids. The thermal diffusivity of nanofluids can also be used to calculate the Prandtl number, is computed using the correlation proposed by Yimin and Li [2]

$$\alpha_{nf} = \frac{k_{nf}}{(\rho C_p)_{nf}} = \frac{k_{nf}}{(1-\varphi)(\rho C_p)_{np}+\varphi(\rho C_p)_{bf}} \tag{5.4}$$

The viscosity of the nanofluids is calculated using the equation proposed by G. K. Batchelor [137]

$$\mu_{nf} = \mu_{bf}(1 + 2.5\varphi + 6.5\varphi^2) \tag{5.5}$$

The nanofluids have better thermal properties in comparison to base fluids. The use of nanofluids and their influence on the efficiency of the solar collectors is estimated using the proper energy equations.

The heat transfer properties, especially the heat convection coefficient between the between the absorber and working fluid is a key factor to analyze the heat transfer characteristics. The higher convection coefficient leads to the lower absorber temperature, therefore low thermal losses from the absorber as suggested by Lienhard VI and Lienhard V [138]. The heat convection coefficient is estimated using the useful energy equation suggested by Incropera [128].

$$Q_u = h_{con} A_r (T_r - T_{avg}) \tag{5.6}$$

The Nusselt number needs to be calculated to find the h_{con}.

$$N_{u_{nf}} = \frac{h_{con}\, D_h}{k_{nf}} \tag{5.7}$$

where D_h and k_{nf} represent hydraulic diameter and thermal conductivity of nanofluids. The correlation proposed by Colburn [138] is employed to estimate the Nusselt number. Colburn correlation is widely used to find Nusselt numbers under the turbulent flow regime.

$$N_{u_{nf}} = 0.023 {R_{e_{nf}}}^{0.8} . {P_{r_{nf}}}^{0.4} \tag{5.8}$$

To find the Nusslet number, it is necessary to first find the Reynolds and Prandtl numbers. The Reynolds number is calculated using the mass flow rate of the nanofluid as proposed by Duffie and Beckman [124].

$$R_{e_{nf}} = \frac{4.\dot{m}}{D_{ri}.\mu_{nf}} \tag{5.9}$$

The viscosity of the nanofluids plays an important role in determining the flow regime of the fluids. At elevated temperatures, viscosity effects become weaker and can sometimes be ignored in the analysis. The details of the viscosity affects are provided in results and discussion section (Fig. 15b). The Reynolds number for the nanofluids is calculated to be 8111, which confirms the flow to be in the turbulent region, therefore the Nusselt number is calculated using equation (5.11). The Prandtl number is determined as

$$P_r = \frac{\mu_{nf}.C_{p_{nf}}}{k_{nf}} \tag{5.10}$$

The formula proposed by Xuan and Li [2] is specifically derived to find Nusselt number for nanofluids. This correlation includes the percentage of nanoparticles, the results of this equation are in good agreement with Colburn equation [139].

$$N_{u_{nf}} = 0.0059\left(1 + 7.628\phi^{0.6886} . {P_e}^{0.001}\right) . {R_{e_{nf}}}^{0.9238} . {P_{r_{nf}}}^{0.4} \tag{5.11}$$

The combination of equations (5.7-5.11) provides the h_{con}, which is further used in solar collectors along with radiation coefficients to find the useful energy. The useful energy produced by solar collectors is computed using the formula suggested by Kalogirou S. A. [123].

$$Q_u = A_c F_r (G_T(\tau\alpha) - U_L(T_{in} - T_a) \quad (5.12)$$

where A_c, F_r, G_T and U_L represent surface area of the collector, heat removal factor, solar radiation and loss coefficient through the collector. The first term on the left side of the equation shows the absorbed energy and the term of the right side shows the energy lost from the collector.

The instantaneous efficiency of the solar collector is calculated using the equations proposed by Kalogirou S. A. [123].

$$\eta_i = \frac{Q_u}{A_c G_T} = \frac{\dot{m} C_p (T_{out} - T_{in})}{G_T} \quad (5.13)$$

$$\eta_i = F_r(\tau\alpha) - F_r U_L \frac{(T_{in} - T_a)}{G_T} \quad (5.14)$$

5.3 Experimental setup

The experimental system is fabricated based on the design parameters mentioned in chapter 4, for real time analysis. The setup consists of a PTC, working fluid circuit, sensing and measuring instruments. The stainless steel sheet having dimensions of 1.8m x 1m is used to reflect solar rays onto the solar collector. The sheet is properly bent to achieve the desired design concentration ratio of 9.89 and focal point of 0.210.

The evacuated tube receiver consists of a copper tube 2m long with outer and inner diameters of 0.021m and 0.019m, respectively, with selective coating. The absorber tube is covered by borosilicate glass of thickness 0.003m. Additionally, the storage tank with polyurethane insulation also equipped with electric heater, a heat exchanger, water pumps and data acquisition unit are also included. The design parameters and overall system specifications are defined in Table 2. The task of Single axis E-W tracking was accomplished by solar tracking kit consisting of sunlight sensor and solar tracker linear actuator.

Table 2: Design parameters of the parabolic trough solar collector

Parameter	**Symbol**	**Unit**	**Value**	
Aperture area	A_{ap}	m^2	1.8	Fixed
Receiver outer diameter	d_o	m	0.021	Fixed
Receiver outer diameter	d_i	m	0.019	Fixed
Glass cover diameter	d_g	m	0.182	Fixed
Glass cover thickness	t	m	0.003	Fixed
Ambient temperature	T_0	K	300	Variable
Ambient Pressure	P_0	kPa	100	Fixed
Length of the receiver tube	L	m	2	Fixed
Sun temperature	T_s	K	5600	Fixed
Inlet temperature of the solar receiver	T_{in}	K	310	variable
Outlet temperature	T_{out}	K	-------	Variable
Solar radiation	G_b	W/m^2	900	Variable
Concentration ratio	C	------	9.89	Fixed
Mass flow rate	$\dot{m}$	Kg/s	0.01	Variable
Tracking	-----	------	E-W	Fixed

5.3.1 Measurement Procedure

This experimental study was conducted at RERDC (Renewable Energy Research and Development Center) located in Taxila. Taxila Latitude and longitude is 33.7370° N, 72.7994° E. The PTC is capable of single axis E-W tracking located on N-S axis. Fig.13 shows the schematic of the experimental setup. In the current study various parameters such as climate, inlet and outlet parameters are continuously monitored at time interval of 5 minutes. The parameters include direct solar radiation, ambient temperature, wind velocity, fluid temperature, and mass flow rate of the working fluid.

Operating temperatures in the range of 20-90℃ were measured by using K type thermocouples with sensitivity of 0.01℃ and calibrated with standard thermocouple temp sensor PT100 having calibration range - 20°C ~ 100°C with an accuracy of ±0,1°C in refrigerated bath circulator model WCR-P12. Digital flow transducer S8011R was used to measure the mass flow rate in the range of 3-100 kg/h. Whereas, climate data including wind velocity, solar radiations are measured through hot wire anemometer and Pyrheliometer model TBS-2-2 with spectral range of 280-3000ns and sensitivity of 9.876 uv/wm^2. Experiments were conducted from 9:00 am to 6:00 pm in each case with a fixed mass flow rate of 60 (kg/hr). Climate data was recorded in Jinzhou Sunshine Science Data collector unit model TRM-Zs1.

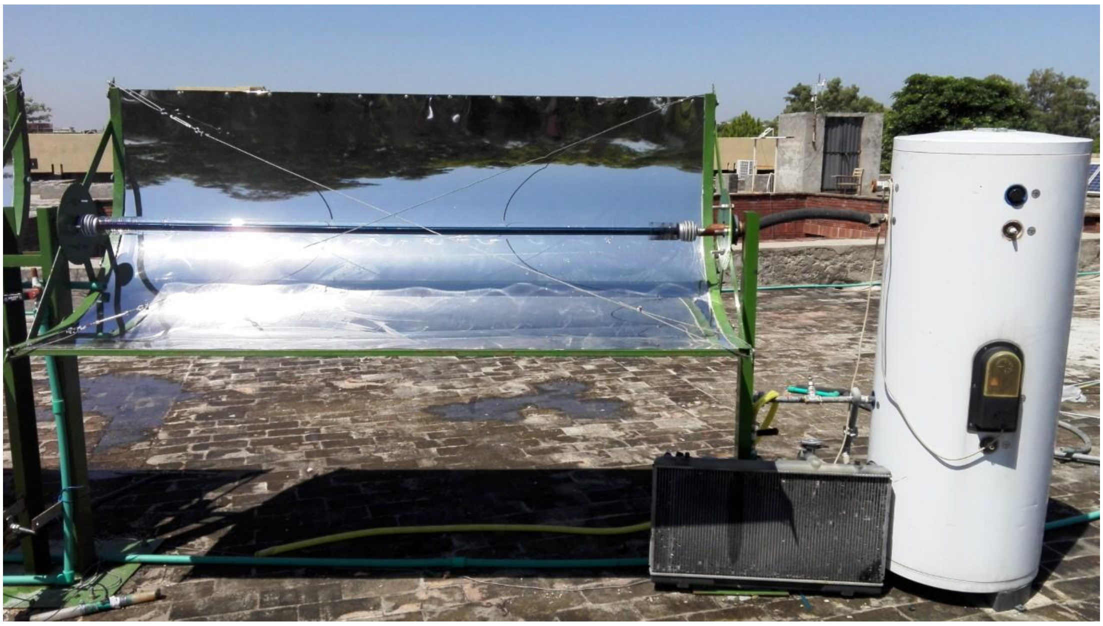
Figure 13: Schematic of the parabolic trough solar collector

The accuracy of the components involved in the experimental setup is always a major concern to be considered. The accuracy of the measurement shows the closeness of the results with its real value. The higher the accuracy, the less will be the error. There is always some uncertainty in experimental results, the errors can and do happen in experimental observations. A great care needs to be taken to reduce the possibility of the errors. The error analysis are performed in-between the experimental and simulation results and the percentage error is calculated using the equation given below.

$$\%error = \left[\frac{Exp_{results} - Simu_{results}}{Simu_{results}}\right] * 100 \tag{5.15}$$

Chapter 6

RESULTS AND DISCUSSION

This chapter explains in detail, the modelling and simulation results of solar collectors (SCs), solar thermal power plants and solar assisted multi-effect absorption cycles and their validation with the literature results. Starting with nanofluids, the use of nanofluids in SCs, the integration of solar collectors with steam cycle and finally, the integration of solar collectors with absorption cycles are discussed in detail.

It is necessary to mention that most of the present work is based on the simulations rather than on experimental observations. There were some constraints in conducting the experiments such as the unavailability of the test facility at author's university, therefore, the author had to travel to Pakistan (UET Taxila) to conduct the experiments. There was another difficulty in finding the required equipment for the experimental setup and to purchase nanoparticles to make the nanofluids ready. The other constraints such as, the unavailability of the equipment to prepare the nanofluids, lack of time and lack of resources prevented us to perform adequate experiments within the specified timeframe. Consequently, the authors decided to opt for simulation analysis of the proposed systems. The simulation results are validated with experimental results obtained through experiments.

6.1 Nanofluids

In this study, the nanofluids are prepared using nano sized particles of Al_2O_3 and Fe_2O_3 nano sized powder. The preparation of nanofluids is discussed in chapter 4.

6.1.1 Properties of nanofluids

Nanoparticles of Al_2O_3 and Fe_2O_3 are mixed in distilled water to prepare the nanofluids to be used as HTFs in solar collectors. Table 2 shows the properties of Al_2O_3 and Fe_2O_3 nanoparticles, base fluid (water) and Al_2O_3-water Fe_2O_3-water nanofluids. The properties of the Al_2O_3 nanoparticles are the properties of the nano powder purchased from US Nano Research materials [132].

Table 3: Thermophysical properties of nanofluids at 300 K

Material	**Cp (J/Kg. K)**	**ρ (kg/m^3)**	***k* (W/m. K)**	**μ (Pa s)**
Al_2O_3 [132]	788.2 [140]	3890 [132]	40 [1]	---
H_2O	4175	997.9	0.599	0.0008537
Al_2O_3- H_2O nanofluid	3815	1070	0.643	0.0009106
Fe_2O_3 [132]	696.3 [141]	5240 [132]	6.081[142]	---
H_2O	4175	997.9	0.599	0.0008537
Fe_2O_3- H_2O nanofluid	3785	1083	0.6265	0.0008986

6.1.2 Simulations

The mathematical models of solar collectors, Rankine cycle as well as absorption cooling cycles are analyzed using a simulation program called engineering equation solver (EES) developed by S. A. Klein [122]. The EES software is a well-known software to solve complex engineering equations simultaneously. It has the ability to solve multiple equations and to do the parametric analysis of engineering related problems. Simulations are performed in order to evaluate the heat and mass transfer to and from the systems considered. The input parameters and the boundary conditions applied to simulate the thermodynamic models are presented in chapter 4, section 4.5.

6.1.4 Validation of simulation results with experimental data

The experiments are performed on PTSC using Al_2O_3-water based nanofluids. The preparation and properties of the nanofluids along with experimental detail are discussed in chapter 5. The simulation results are validated with the experimental data collected through solar collectors. The nanofluids of Al_2O_3 and Fe_2O_3 are prepared and further used as HTFs to absorb sunlight. The comparison between simulations and experimental results of Al_2O_3 nanofluid at 2 % weight fraction of nanoparticles are presented in Fig. 14. The collector parameter $(T_{in} - T_0)/G_b$ for experimental results and simulations is plotted against the inlet temperature of the solar collector.

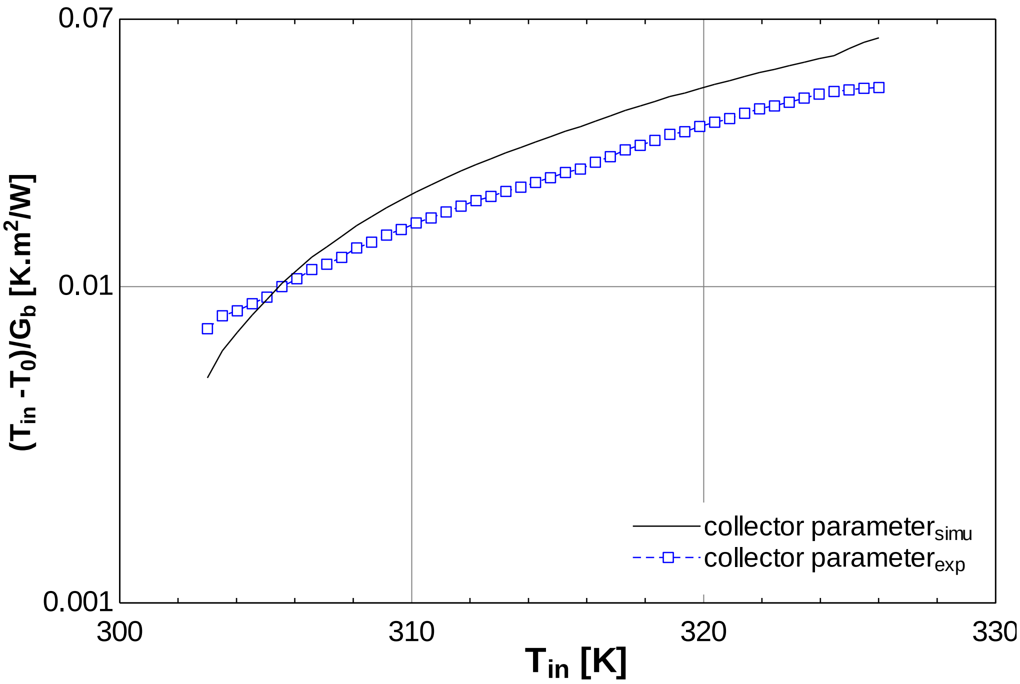

Figure 14: The effect of inlet temperature on collector parameter of the PTSC

As expected the experimental results of $(T_{in} - T_0)/G_b$ are lower in comparison to simulation results. The reason for the lower experimental results is that the simulation software is designed to work under steady state conditions, while the experiments are conducted in an environment, where the solar radiation changes with time. The lack in experimental data was the main hurdle in performing the statistical analysis of the experimental results. The inaccuracy of the experimental setup may also be the reason of lower experimental results. The percentage error (Fig. 14) is calculated using equation 5.15, and the percentage error is observed to be 19.35%. The higher error would be attributed to the inaccuracy of the experimental setup.

Fig. 15 displays the relationship between the collector efficiency and the collector parameter. The experimental results are close to the simulations at lower values of collector parameter but deviate at higher values of collector parameter. The deviation in experimental results from simulations is expected because simulations are performed on steady state conditions, on the other hand, the experimental results vary with operating conditions. Both numerical and experimental results show similar trends in energy efficiency at a collector parameter of 0.012, and starts to deviate from each other at higher values of the collector parameter. The percentage error is calculated using the equation 5.15, the percentage error is observed to be 20.75 % at a collector parameter of 0.03.

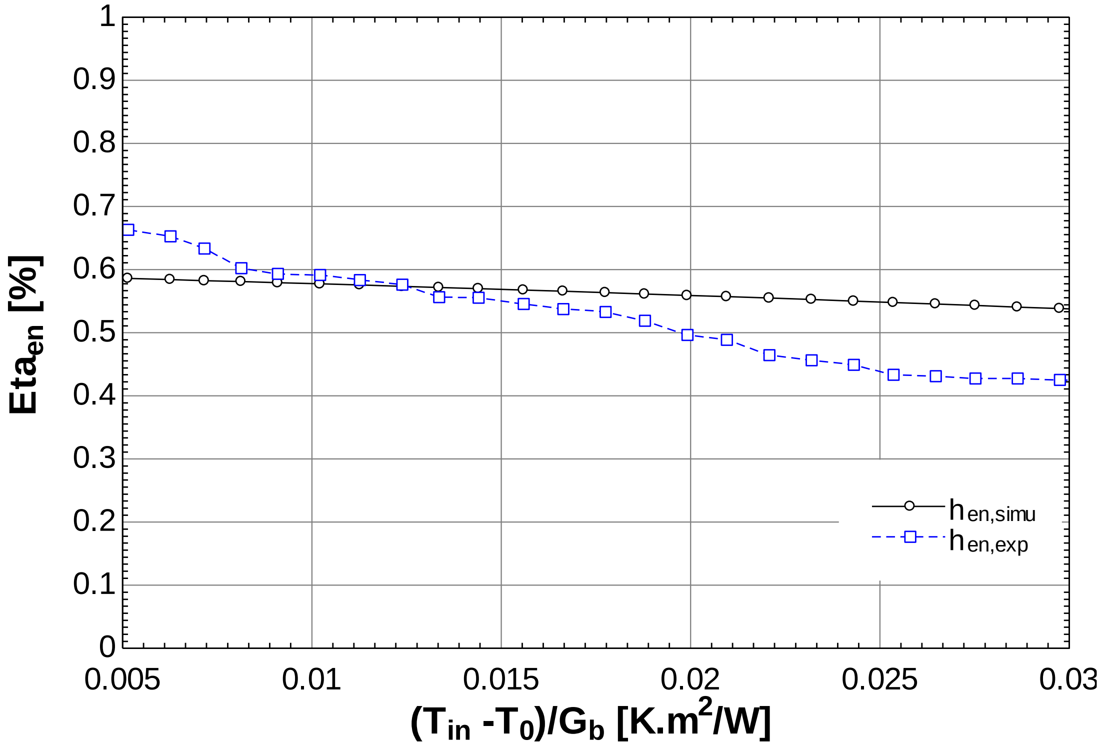

Figure 15: The effect of collector parameter (T_in-T_0)/G_b) on the collector efficiency

The properties (Cp, *k*, ρ, μ) of Al_2O_3 and Fe_2O_3 water based nanofluids are calculated using the proper equations by varying the temperature range. The Fig. 16 demonstrates the property comparison between Al_2O_3-water nanofluid and water as the base fluid. Figure 16 a, illustrates the behavior of thermal conductivities of Al_2O_3- water based nanofluids and water. The thermal conductivity of nanofluids is higher in comparison to water, because the Al_2O_3 nanoparticles have higher tendency to conduct heat. Dynamic viscosity comparison is provided in Fig. 16 b, and the viscosity is observed to be higher for nanofluids than the base fluids of water. The Fig. 16 c, provides an overview between the densities of the nanofluid along with base fluid (water). Nanofluid is observed to have greater density as compared to base fluid but the C_p of base fluids is higher than nanofluids, the results of these (Cp, *k*, ρ, μ) properties obtained in the present study show somehow a similar behavior with the results of reference [1]. The reference [1] compares oil based nanofluids with base fluid of oil, on the other hand, the present results compares water based nanofluids with base fluid of water. The water goes through a phase change process at 100℃ (373.15 K). Therefore, thermal conductivity (Fig. 16a) of water and water based nanofluids increases initially then starts to decrease with increase in temperature. Three of the four properties mentioned in Fig. 16, are higher for nanofluids in comparison to base fluid. Because the nanoparticles in their solid form hold higher properties.

The Fig. 17 shows the comparison of Fe_2O_3-water nanofluids with water as base fluid. The Fig. 17a, illustrates the behavior of thermal conductivity with increase in temperature. The thermal conductivity of Fe_2O_3-water nanofluids is higher in comparison to water. All these properties are evaluated at higher pressures to keep the water in liquid form at higher temperatures. The properties of both Al_2O_3 and Fe_2O_3-water nanofluids show the similar trend as observed by [1]. The thermal conductivity, viscosity and density of nanofluids are higher, while the specific heat capacity is lower than base fluid of water (Fig. 17d). The reason of the higher properties is that the nanoparticles possess higher properties in their original (powder) form. It is assumed that the Al_2O_3- water based nanofluids behave as Newtonian fluids as observed by Das et al. [31]. It is also witnessed in their studies that the viscosity is independent of the shear rate.

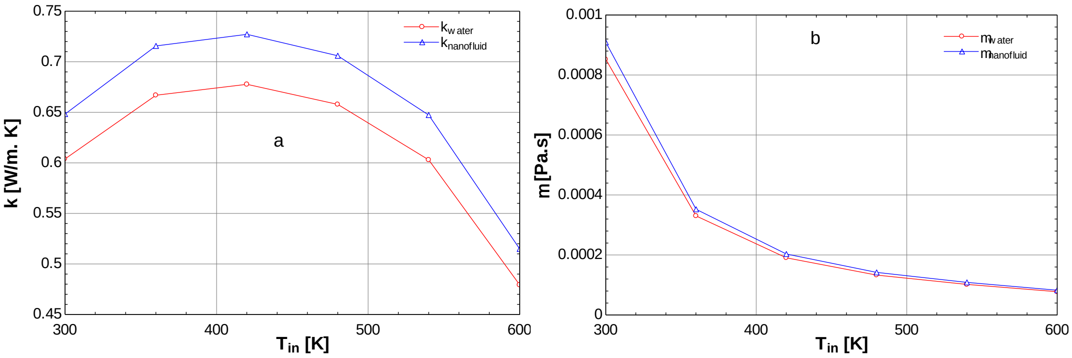

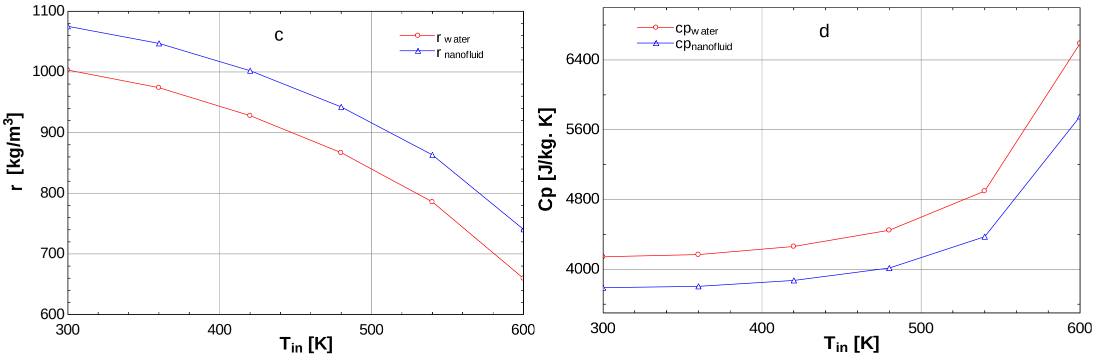

Figure 16: Property comparison between Al_2O_3 nanofluid and base fluid (water). a) Thermal conductivity, b) dynamic viscosity, c) density, d) specific heat capacity.

6.2 Solar collectors

In this section, the solar collectors are simulated and analyzed in detail. The solar collectors are modelled to work on nanofluids as HTFs. The solar collectors of parabolic trough and parabolic dish are modelled using EES software developed by S. A. Klein [122].

6.2.1 Parabolic trough solar collector (PTSC)

The parabolic trough (PT) solar collector is simulated and analyzed for its energetic and exergetic performance perspective. The PT solar collector model is adopted from the model presented by S.A. Kalogirou [123] and F. A. Suleiman [56]. The simulation results of the solar collector are validated with the reference model and are presented in table 3. The comparison of energy efficiency shows that the results of our models are within 0.63% difference with the reference model, which confirms the validity of our models.

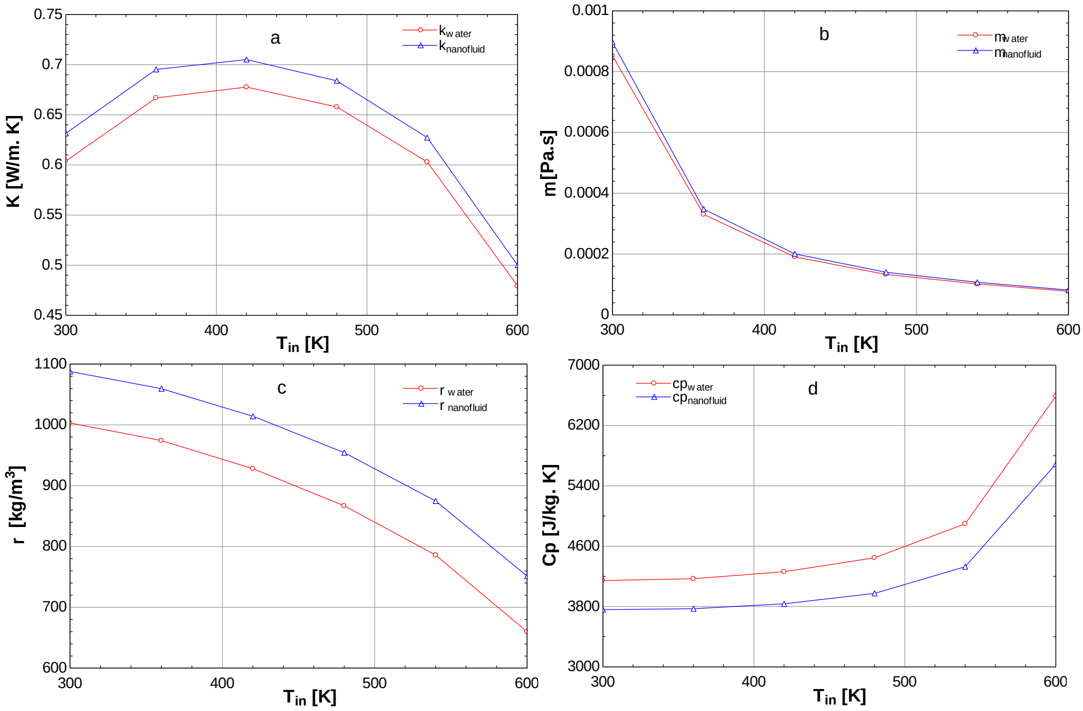

Figure 17: Comparison of the properties between Fe_2O_3 nanofluids and water. a) Thermal conductivity, b) dynamic viscosity, c) density, d) specific heat capacity.

The main parameters of the reference model are reformed according to design conditions. The parameters such as collector area, receiver area, working fluid, convection heat transfer coefficient, etc. are modified to meet the useful energy output. The assumptions made in analyzing the model are provided in chapter 4.

Table 4: Validation of the present results of PTSC with ref. [123] at inlet temperature of 350 K

Material	**η_{en} [%]**	**η_{ex} [%]**	**Cp (J/kg. K)**
Kalogirou [123]	67.37	16.44	3800
Al_2O_3-water (nanofluid)	67.53	16.36	3890
Fe_2O_3-water (nanofluid)	67.37	16.49	3765
Water	67.80	16.08	4160

The parametric study is performed in order to evaluate the performance of the collectors. Three different fluids are used as HTFs, from which two of them are Al_2O_3 and Fe_2O_3-water based nanofluids and water. The performance of collectors is evaluated and compared using parametric studies. The performance parameters such as, solar irradiation, inlet temperature, ambient temperature, percentage of nanoparticles and mass flow rate are varied individually in order to observe their effect on useful energy, energy efficiency, exergy efficiency and convection heat transfer coefficient.

The convection heat transfer coefficient (h_{con}) is considered the main parameter to effect the performance of solar collectors. The influence of mass flow rate on h_{con} is plotted at various inlet temperatures and is displayed for Al_2O_3-water nanofluids (Fig. 18). The increase in inlet temperature of the receiver increases the convection heat transfer coefficient through the collector. The h_{con} gets increased with increase in mass flow rate. The increased heat transfer coefficient, $h_{con,}$ will increase the convection heat transfer (equation 5.6) of the PT solar collector. The main significance of the higher convection heat transfer coefficient is the higher rate of heat transfer, which is very vital in applications such as cooling of microelectronics. The geometry affects also play an important role in heat transfer enhancement through nanofluids as suggested by Bellos et al. [1], however, geometry affects are not considered in the present analysis. They shall definitely be evaluated in the upcoming research. The Fig. 19 shows the variation of h_{con} with respect to percentage of nanoparticles. The increase in percentage of nanoparticles increases the heat transfer coefficient of the nanofluids. This behavior was expected because the movement of the particles transport some of the heat with them to contribute to total heat transfer through agitation in the liquid. This phenomenon seems to explain the behavior of nanofluids. The effect of increase is observed to be higher at higher inlet temperature. The relationship between the percentages of nanoparticles of Al_2O_3 and T_{out} of the solar collector is presented in Fig. 20. It is obvious that the increase in percentage of nanoparticles affects the outlet temperature of Al_2O_3-water nanofluids. The influence of percentage is observed to be higher at higher inlet temperatures.

The Fig. 21 shows the energetic and exergetic efficiency comparison with respect to ambient temperature. The energetic performance increases with increase in ambient temperature. Both nanofluids have similar increase in efficiency, water has comparatively higher energy efficiency than nanofluids. The exergetic efficiency (η_{ex}) shows the opposite trend and it decreases with increase in ambient temperature. The η_{ex} of nanofluids is perceived to be 3.96% greater as compared to water.

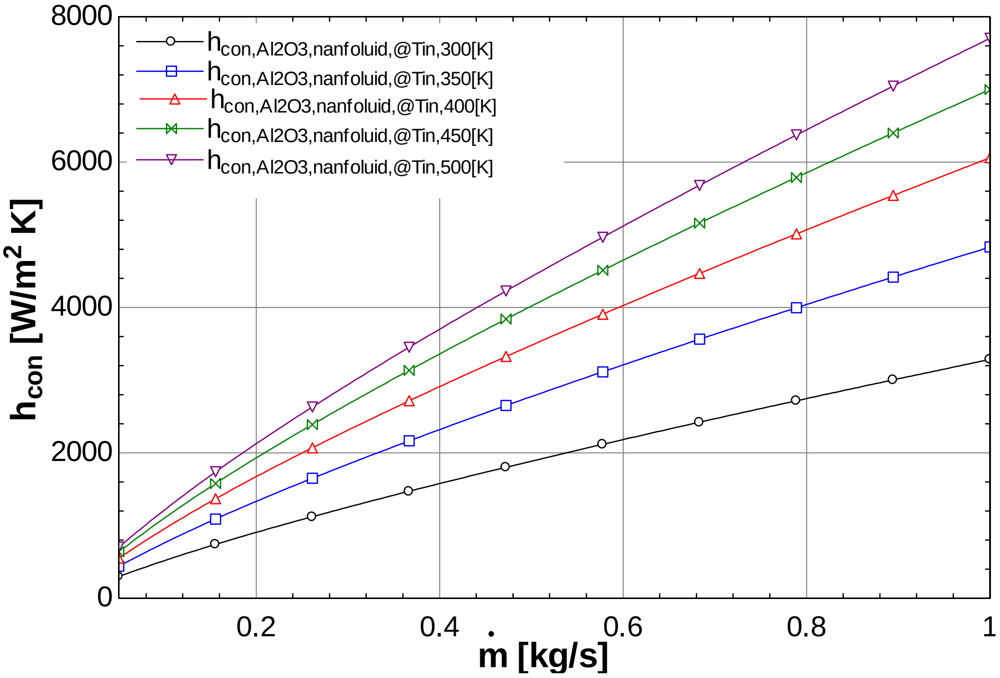

Figure 18: The variation in heat convection coefficient with respect to mass flow rate of the collector.

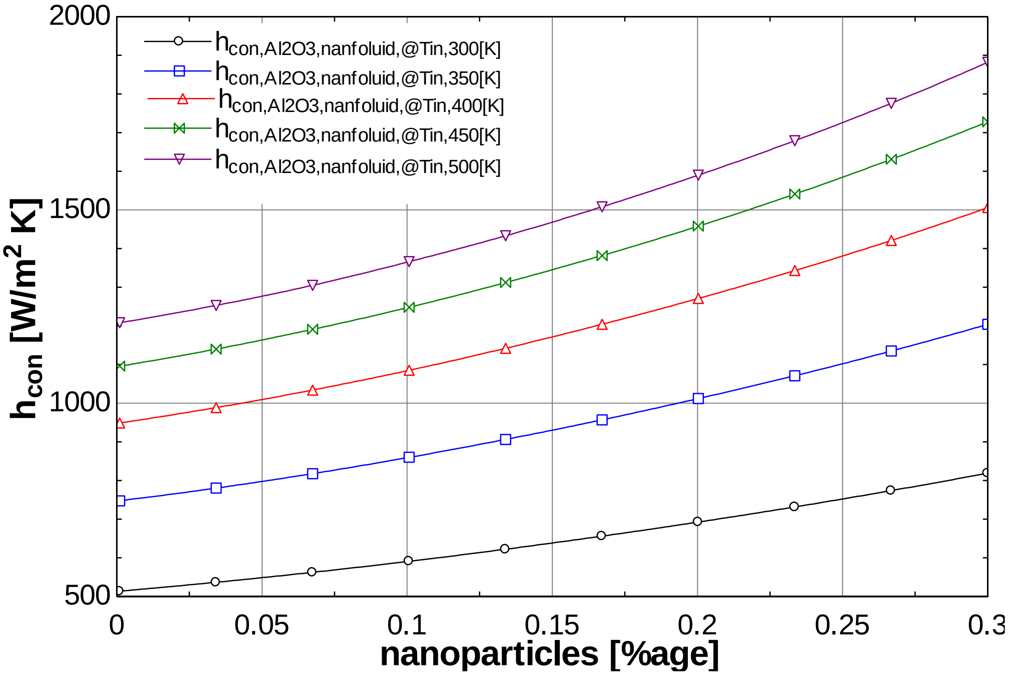

Figure 19: The relationship between percentage of Al_2O_3 nanoparticles and heat convection coefficient at various inlet temperatures

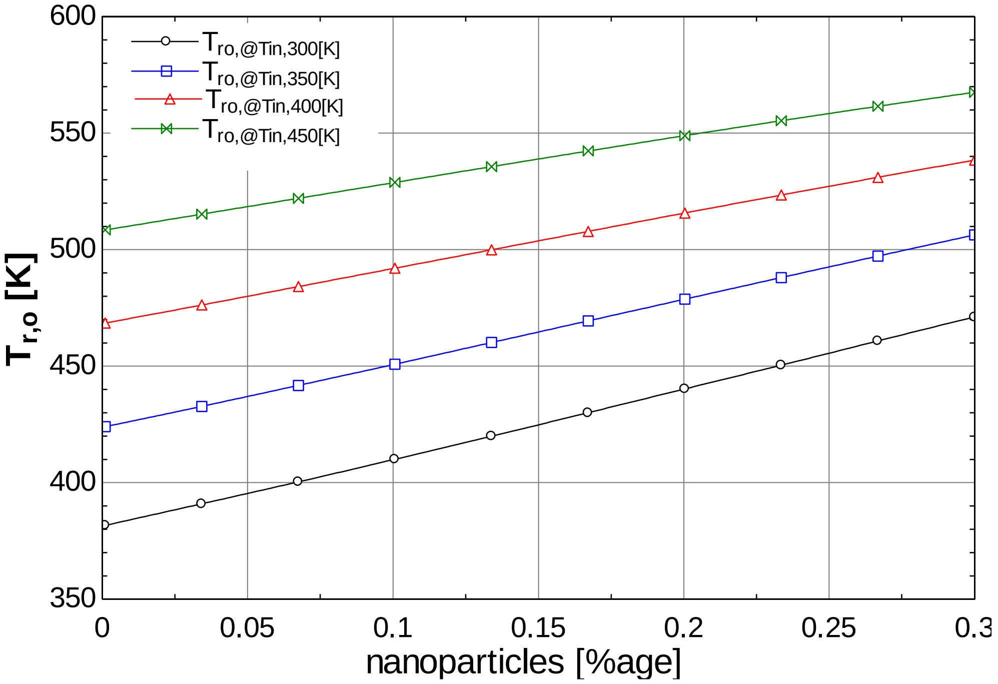

Figure 20: The relationship between outlet temperature of the collector and percentage of Al_2O_3 nanoparticles.

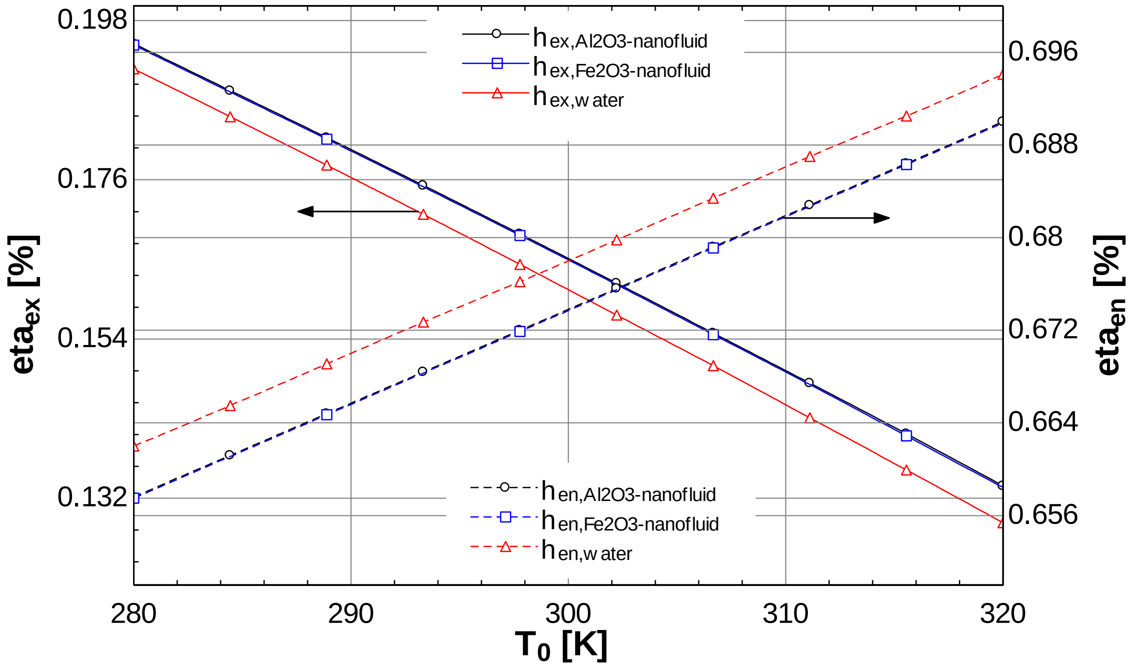

Figure 21 : The influence of ambient temperature on the energetic and exergetic efficiencies of the PT solar collector.

6.2.2 Parabolic dish solar collector (PDSC)

Parabolic dish solar collectors are second set of collectors used to obtain heat from solar energy. The design parameters of PD collectors are different than PT collectors, because they can concentrate the solar rays at higher ratios and has higher operation temperature under identical operating conditions Kalogirou [123]. The PD collectors are simulated and analyzed for thermal power as well as for electric power generation. The models used in this study are adopted from the models presented by Lloyd C.N. [67], Sendhil K. N, K.S. Reddy [68], Kaushika N. D., and K. S. Reddy [69]. The reference models are more focused on optical analysis. The reference model is redesigned according to the design conditions. The parameters such as, collector area, receiver area, working fluid are changed to fulfill the required thermal power (Q_u) output. In the reference model, the convection heat transfer coefficient was assumed as a fixed value, but in present study, it is calculated using the proper equation. The

PD model used in this study is validated with the reference model and their comparison is presented in table 4.

Table 5: Validation of the present results with ref. [67] at inlet temperature of 350 K.

Material	**η_{en} [%]**	**η_{ex} [%]**	**Cp (J/kg. K)**
Lloyd C.Ngo [67]	76.42	19.12	4087
Al_2O_3-water (nanofluid)	73.23	18.29	3866
Fe_2O_3-water (nanofluid)	72.13	18.07	3774
Water	72.33	17.53	4160

The parametric study is performed in order to evaluate the performance of the PD collectors. The HTFs used are Al_2O_3 and Fe_2O_3-water based nanofluids and are compared with water. The performance of collectors is evaluated and compared by performing parametric studies. The performance parameters such as, solar irradiation, inlet temperature, ambient temperature, percentage of nanoparticles and mass flow rate are varied in order to observe their effect on useful energy, energy efficiency, exergy efficiency and convection heat transfer coefficient.

The Fig. 22 shows the relationship between outlet and inlet temperature of PD collector. The outlet temperature increases with increase in inlet temperature. The outlet temperature increases from 435.7 K to 572.4 K, 436.5 K to 569 K and 428.6 K to 561.8 K respectively for Al_2O_3 and Fe_2O_3-water based nanofluids and for water. It is observed that the outlet temperature for nanofluids is about 1.89% (temperature difference of 10.6 K) higher in comparison to water. The enhancement in outlet temperature is credited to higher properties of nanofluids. The movement of the particles absorbs some extra amount of heat, which leads them to have higher temperature as compared to base fluid.

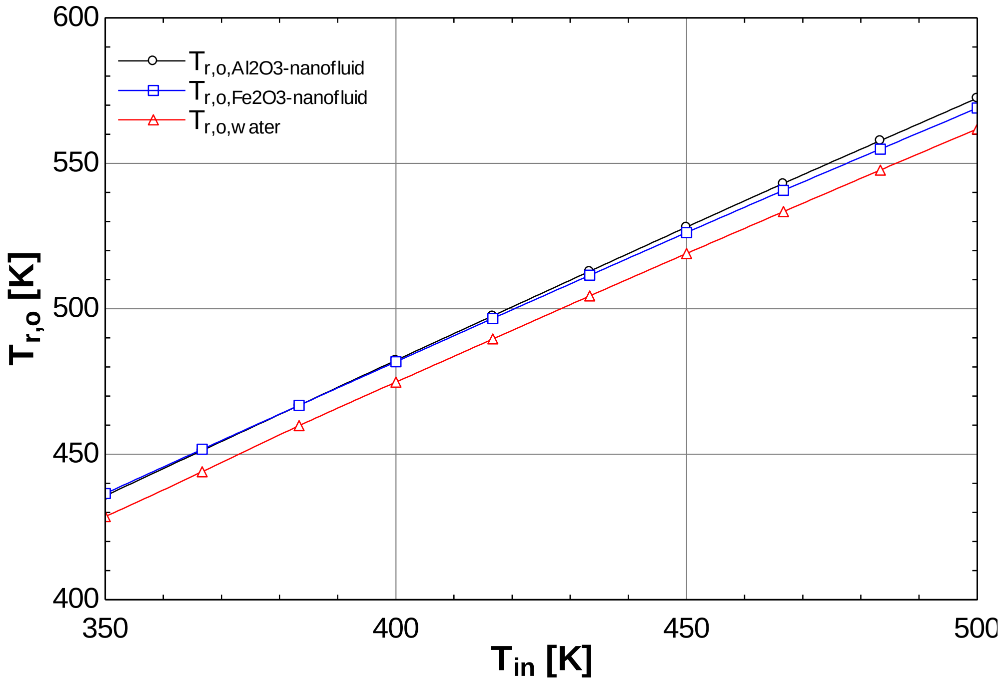

Figure 22: The influence of inlet temperature on T_{out} of the collector

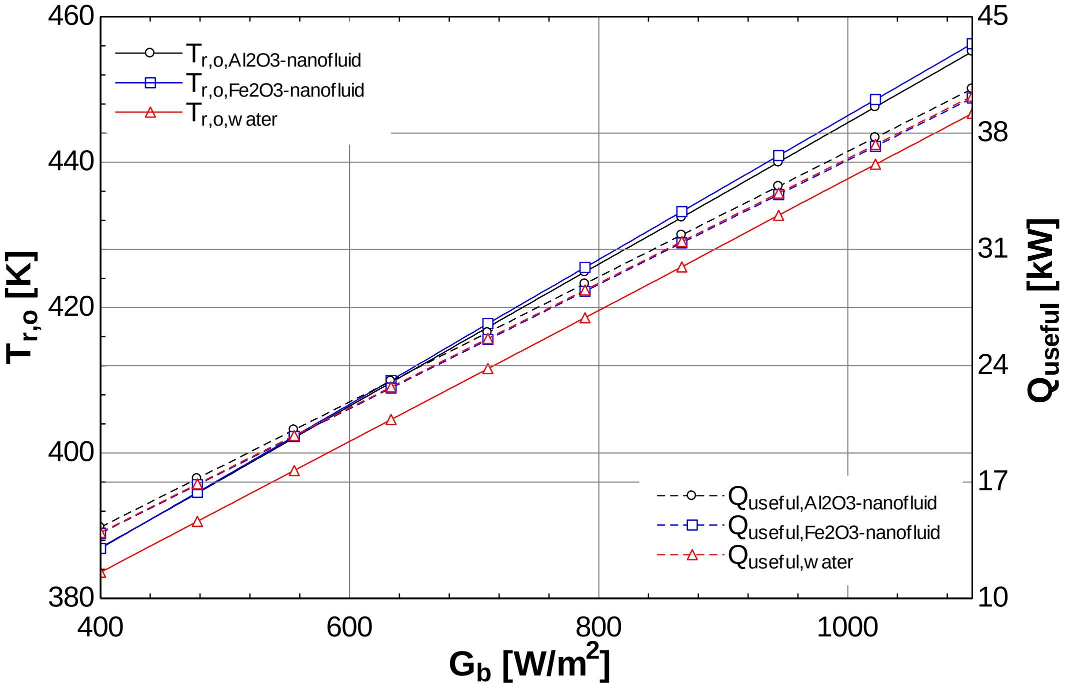

Figure 23: The deviation in the outlet temperature and useful heat of the collector with increase in solar irradiation.

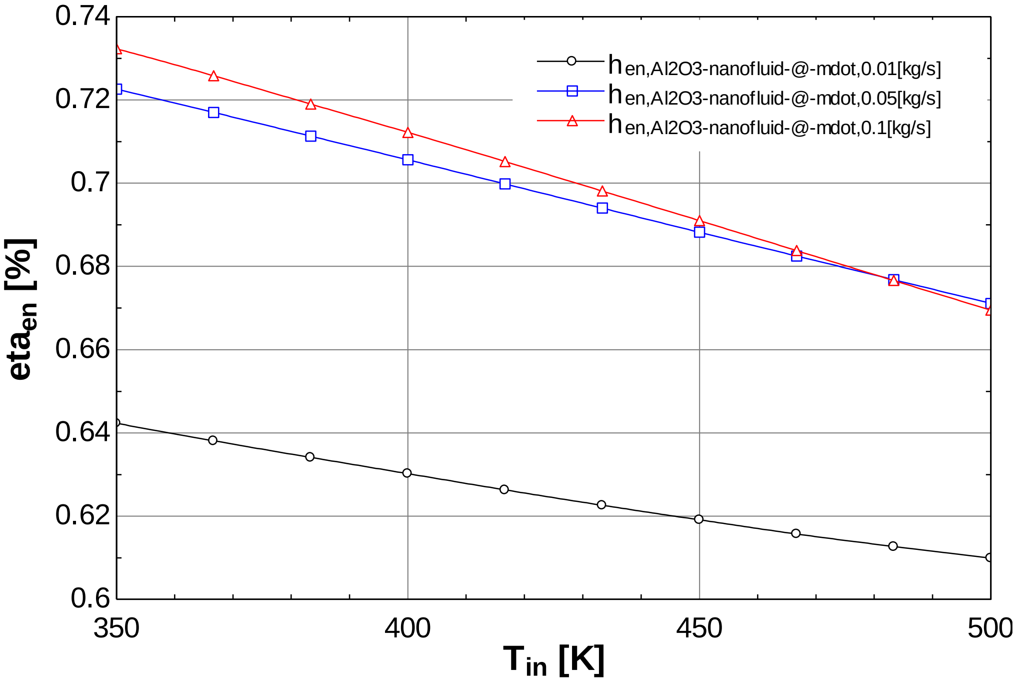

Figure 24: The impact of inlet temperature on energetic efficiency at different mass flow rates of the solar collector

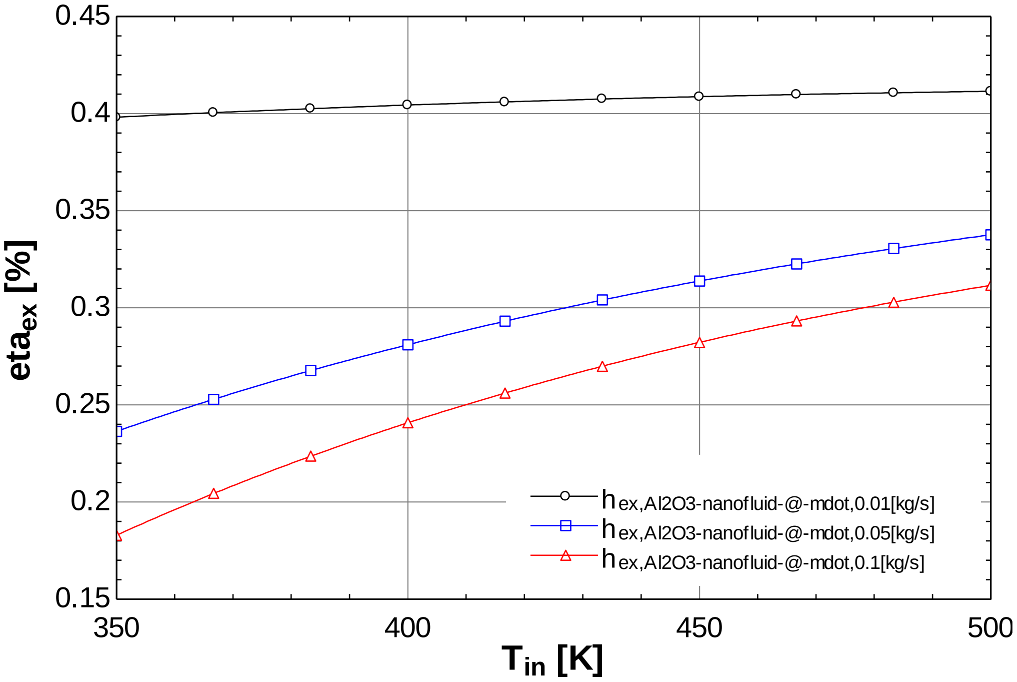

Figure 25: The variation in exergetic efficiency with inlet temperature of the solar collector

The Fig. 23 displays the difference of outlet temperature and useful energy produced with respect to solar irradiation. It is clearly seen that both the outlet temperature and useful energy increases with increase in solar irradiation. The outlet temperature of nanofluids is 2.14% higher in comparison to water. The useful energy produced increases from 14.29 kW to 40.66 kW, 13.93 kW to 40.11 kW and 13.97 kW to 40.22 kW respectively with increase in solar irradiation from 400 W/m^2 to 1100 W/m^2. The Al_2O_3 nanofluid has the highest rate of useful energy followed by water and Fe_2O_3. The Fig's 24 and 25 shows deviation of energy and exergy efficiency of Al_2O_3 nanofluid at various flow rates of the HTF. The energy efficiency is witnessed to decrease by varying the inlet temperature, the higher efficiency is witnessed at a mass flow rate of 0.1 kg/s. The lower mass flow rate has lower energy efficiency. On the other hand, the exergetic efficiency increases with increase in inlet temperature. The higher exergetic efficiency is observed to be higher at lower mass flow rate. The exergy efficiency of Al_2O_3 nanofluid at three different mass flow rates increases from 39.81 % to 41.15 %, 23.64 % to 33.76 % and 18.29 % to 31.16 % respectively with increase in inlet temperature from 350 K to 500 K. The Fig. 26 displays the influence of ambient temperature on energetic and exergetic efficiency of Al_2O_3 nanofluid. The energy efficiency is observed to be higher at higher incident solar radiation, and increases as the ambient temperature gets increased. The exergetic efficiency follows the opposite trend and decreases with increase in ambient temperature. The higher exergy efficiency is observed at higher incident radiation and decreases linearly with increase in ambient temperature.

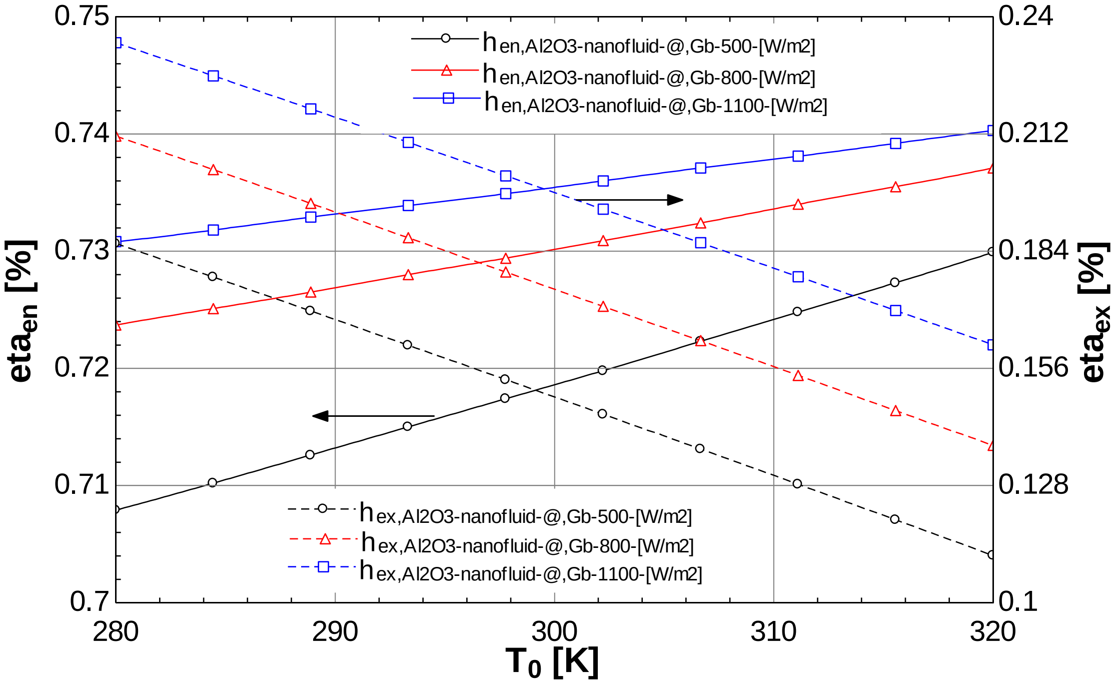

Figure 26: The impact of T_0 on the energetic and exergetic efficiencies.

6.3 Integration of PT-PD solar collectors with steam turbine

In this section, the solar collectors are further integrated with steam turbine (reheat Rankine cycle) to produce power. Both, PT and PD solar collectors are modelled, analyzed and integrated separately with steam turbine making it a solar thermal power plant (STPP). The idea of integration is to fulfil the heat requirement of the steam cycle boiler, it is accomplished with the useful heat produced of the solar field. The steam cycle model is adopted from Cengel Y. and Boles M. C. [127]. The reference model is altered according to the power output requirements. The solar thermal power plant (STPP) is modelled and analyzed using thermodynamic equations in order to evaluate the performance parameters such as, power output, overall energy efficiency and overall exergy efficiency of the STPP. The engineering equation solar (EES) software is used to model and analyze the STPP. The properties of the reheat Rankine cycle are presented in the table 5. The specific enthalpy and entropy at all 14 state points of the reheat Rankine cycle are determined to calculate the required parameters.

Table 6: Properties of the reheat Rankine cycle

No.	**P (kPa)**	**T (K)**	**h (kj/kg)**	**s (kj/kg.K)**
1	7.5	313.4	168.7	0.5763
2	100	313.4	168.9	0.5763
3	100	372.8	417.5	1.303
4	6000	372.5	421.1	1.296
5	3000	507	1008	2.645
6	6000	507.8	1013	2.647
7	6000	507	1008	2.638
8	6000	507.1	1009	2.64
9	6000	623.1	3044	6.336
10	3000	539.8	2905	6.381
11	800	443.6	2624	6.336
12	800	623.1	3162	7.411
13	100	417.1	2765	7.586
14	7.5	313.4	2311	7.411

The Fig. 27 shows the effect of solar irradiation on overall energy and exergy efficiency of PD solar collector. The overall energy and exergy efficiency of all three HTFs increases with increase in solar irradiation. The Al_2O_3 nanofluid is observed to have higher overall performance in comparison to other fluids. The overall energy efficiency of the STPP increases from 20.53 % to 21.24 %, 20.01 % to 20.95 5 and 20.07 % to 21.01 % respectively with increase in solar irradiation from 400 W/m^2 to 1100 W/m^2. The Fig. 28 illustrates the effect of solar irradiation on heat rate produced and net power produced of the parabolic dish solar thermal power plant (PDSTPP). Both net power output and rate of heat transfer increases as the incident solar radiation increases. The total work produced of PDSTPP rises from 4.128 kW to 11.74 kW, 4.024 kW to 11.58 kW and 4.035 kW to 11.62 kW respectively, as the incident solar radiation increases from 400 W/m^2 to 1100 W/m^2. The total work output is observed to be the higher (1.36%) for Al_2O_3 water based nanofluid as compared to water. The Fig. 29 describes the effect of inlet temperature on exergetic efficiency of PD collector and the overall exergetic efficiency of the PDSTPP. It can be seen that the overall exergy efficiency of the system decreases with increase in inlet temperature, on the other hand, exergy efficiency of the PD collector increases with increase in inlet temperature. Both exergy efficiency of the PD collector and overall exergy efficiency of the system for Al_2O_3 nanofluid is higher in comparison to other two fluids.

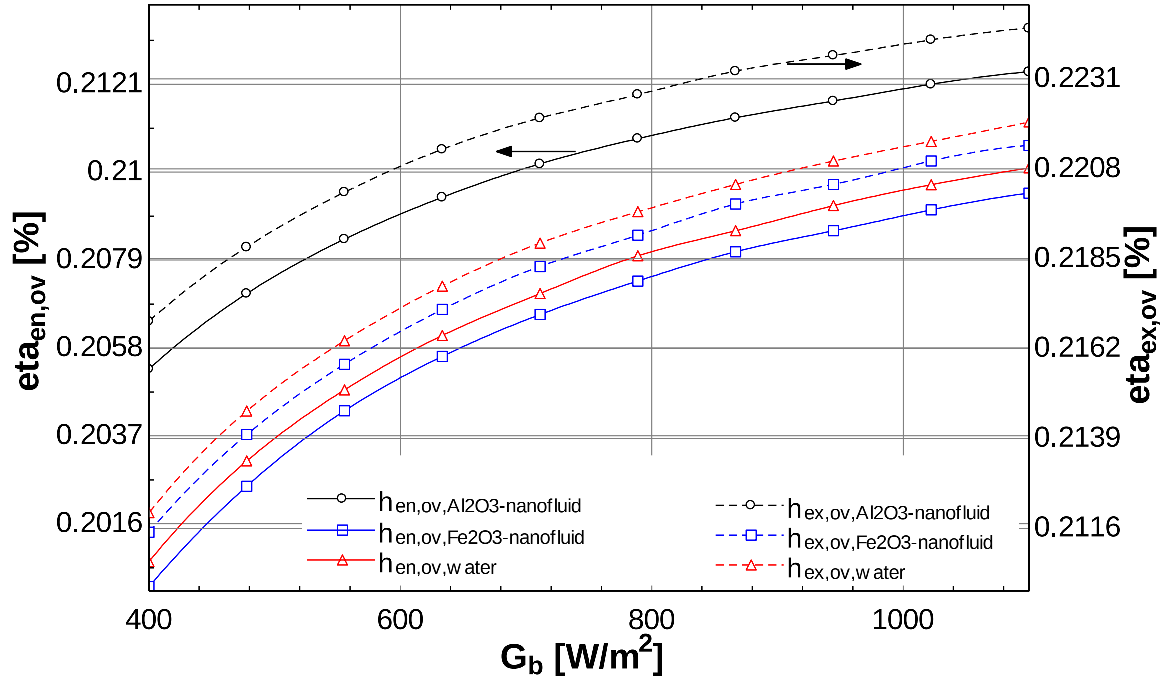

Figure 27: The trend of overall energetic and overall exergetic efficiency of the PDSTPP with respect to G_b.

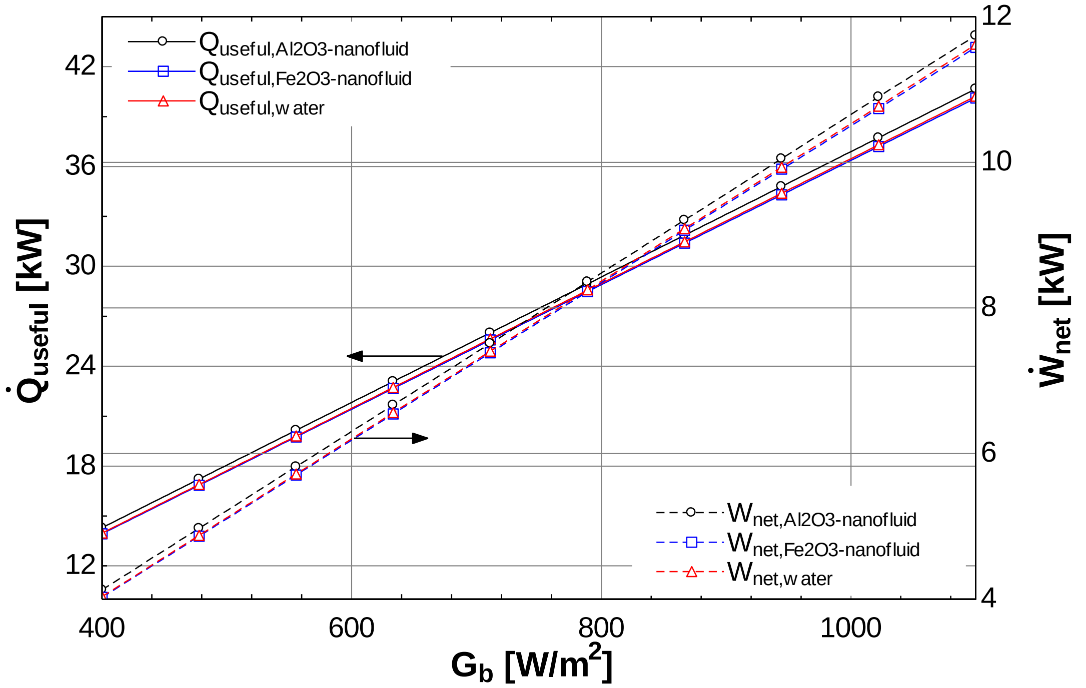

Figure 28: The influence of G_b on the useful heat gain and the net power produced of the PD solar collector

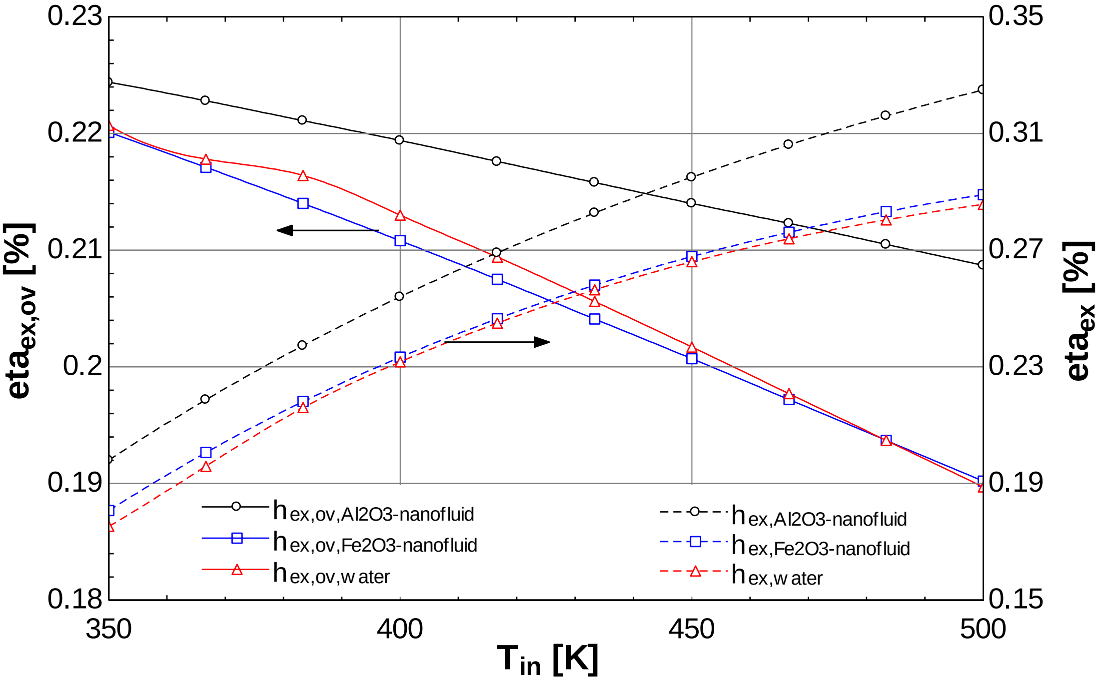

Figure 29: The relationship between the exergetic efficiency of the overall system and exergetic efficiency of the collector with respect to T_{in}.

The Fig. 30 shows the comparison of overall energy and exergy efficiency of PTSTPP with respect to solar irradiation. The overall exergetic performance of the system is relatively higher in comparison to overall energetic performance. It is obvious from the efficiency curves that the real performance (exergetic efficiency) of the system is higher, therefore, performing exergy analysis is preferable.

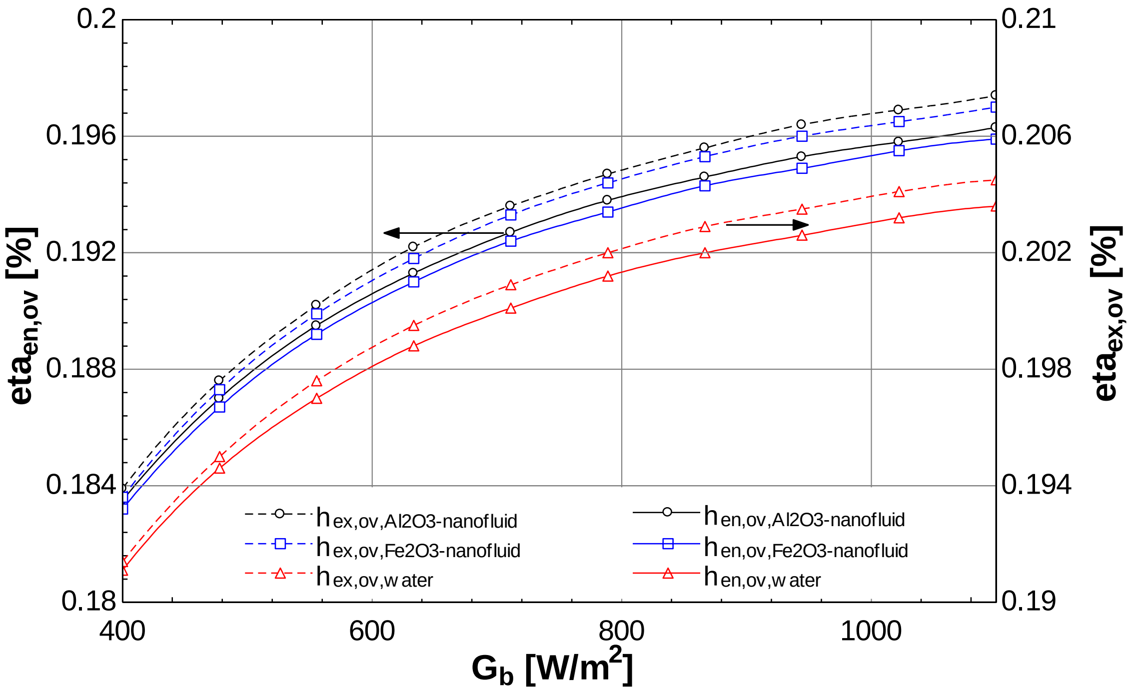

Figure 30: The graph of overall energetic and exegetic efficiencies with respect to G_b.

The Fig. 31 shows the relationship between the solar irradiation and the exergetic efficiency of the combined system with the exergetic efficiency of the PT collector. The overall energy efficiency of the Al_2O_3 nanofluids is higher in comparison to other fluids, it increases with increase in solar irradiation. But the exergy efficiency of the PT collector increases linearly and with increase in solar irradiation. The overall energy efficiency of the PTSTPP increases from 19.39 % to 20.74 %, 19.36 % to 20.7

% and 19.14 % to 20.45 % respectively, with increase in solar irradiation from 400 W/m^2 to 1100 W/m^2.

The Fig’s 32 and 33 show the comparison between the PTSTPP and PDSTPP. The Fig. 32 shows the overall energy comparison of the two (PT-PD) STPPs with respect to solar irradiation. The overall energetic efficiency of the PDSTPP is higher in comparison to PTSTPP. The overall energetic performance of PDSTPP is observed to be 10.62% as compared to PTSTPP. The same trend is observed in Fig. 33, where the total work output of the PDSTPP is higher in comparison to PTSTPP. The total work output of the PDSTPP for Al_2O_3 nanofluid is 10.65% higher than PTSTPP under the identical operating conditions. The same effect is observed for other two working fluids. The higher overall performance of the PDSTPP is attributed to higher concentration ratio, which leads to higher outlet temperature of the collector, consequently will have the higher heat rate produced under identical working conditions.

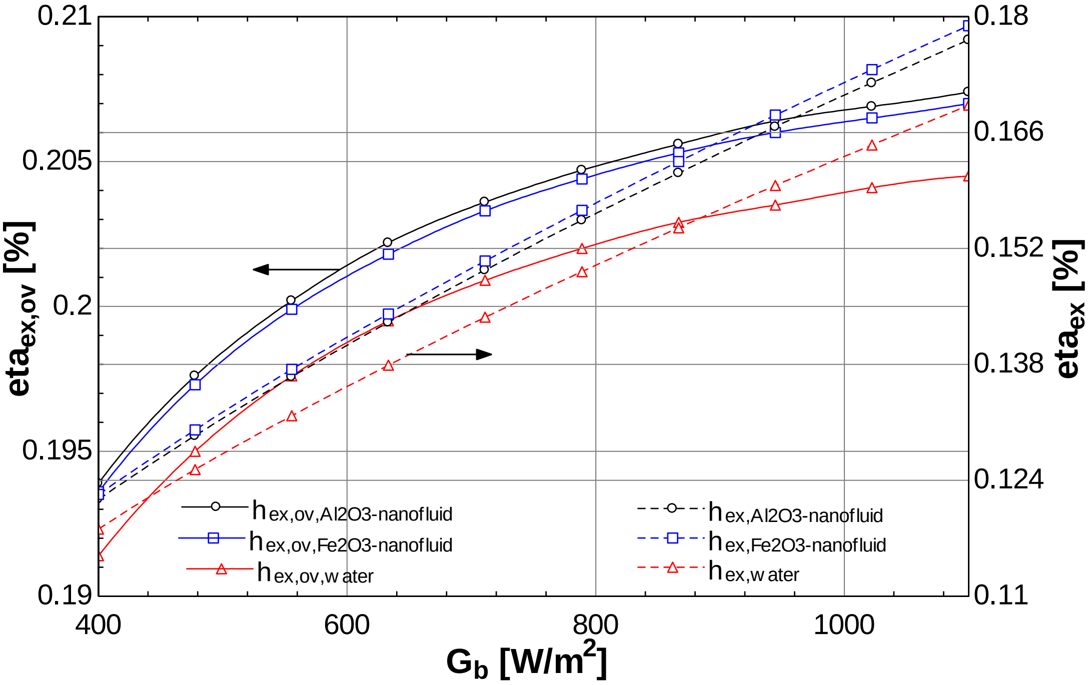

Figure 31: The influence of G_b on overall exergetic and exergetic efficiency of the solar collector

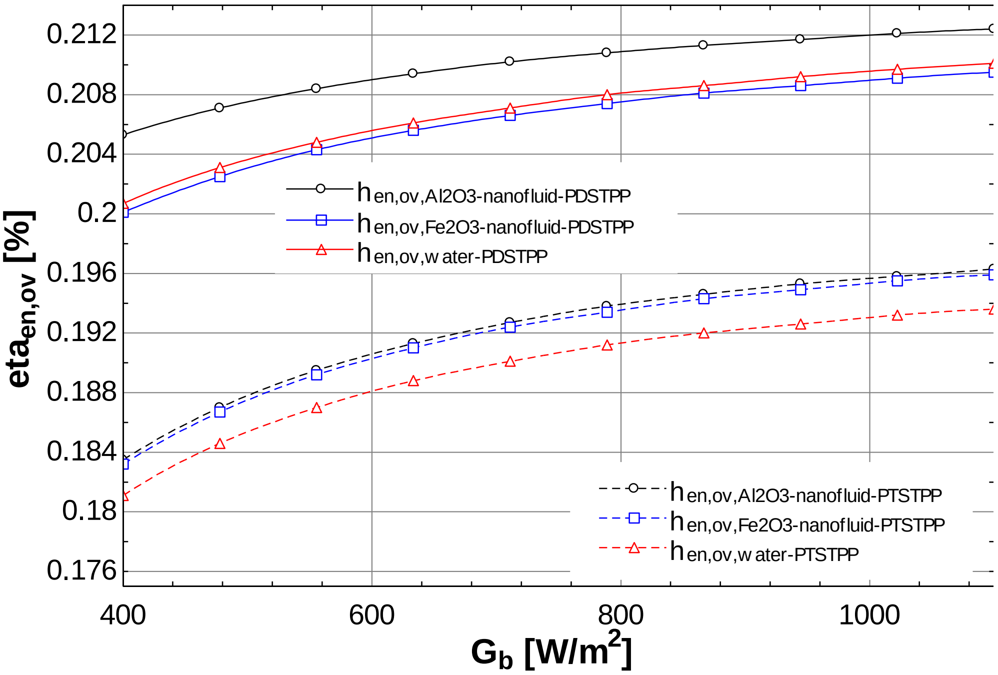

Figure 32: The variation in overall energetic performance of PT-PD STPP with increase in G_b.

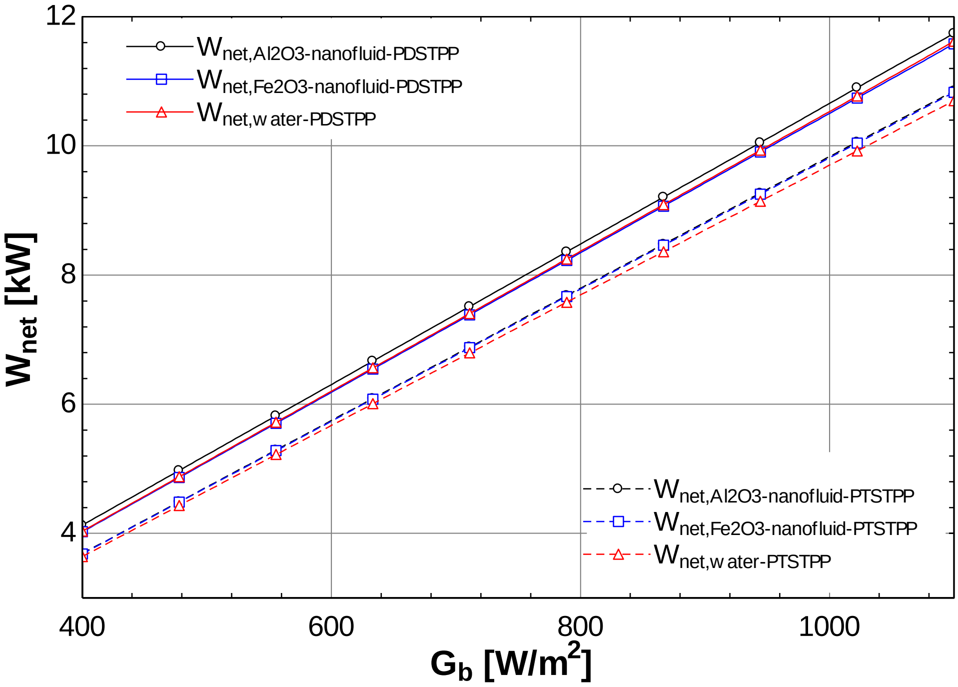

Figure 33: The variation in total work produced of PT-PD STPP with increase in G_b.

6.4 Absorption cooling systems

This section explains in detail the absorption cooling systems. The absorption cooling systems commonly known as absorption cycles are different from conventional vapour compression refrigeration cycles, because they require heat instead of electricity to operate. The absorption cooling systems of single, double, triple and quadruple effect are simulated and analyzed for their exergetic efficiency as well as for their coefficient of performance (COP) under identical environmental and operating conditions. They are also validated with the literature results. The assumption made in analyzing the absorption cycles are presented in chapter 4.

6.4.1 Single effect absorption cycle (SEAC)

The working principle of the SEAC is explained in chapter 4 with the help of mathematical model as well as with the schematic diagrams. The SEAC is designed to work on LiBr-H_2O working pair, where water behaves as a refrigerant and LiBr as absorbent. The input parameters for simulating the SEAC are as follow: inlet temperature of the pump, inlet pressure of the pump, inlet pressure of the generator, percentage of the solution entering the pump, percentage of the solution exiting the generator, exit temperature of the evaporator, condenser load, mass flow rate at the pump inlet, the exit temperature of generator.

The simulation outcomes of the current SEAC are validated with the results of Berhane at al. [131], both results are found to be in good agreement with each other and are presented in table 5. The units of the temperature used in this study are Kelvin (K), and are converted to degree Celsius (℃) for the comparison with the reference [131].

Table 7: Property comparison of single effect cycle, (a) present model, (b) reference model [131] at every state point of the proposed cycle

Point #	**P(kPa)**		**T(℃)**		***h*(kj/kg)**		**s(kj/kg.k)**		**x (%LiBr)**	
	(a)	**(b)**	**(a)**	**(b)**	**(a)**	**(b)**	**(a)**	**(b)**	**(a)**	**(b)**
1	1	1	32	32	69.96	73.2	0.2102	0.22	0.5225	0.5225
2	4.81	4.81	32.4	32	69.96	73.2	0.213	0.22	0.5225	0.5225
3	4.81	4.81	64.4	64.5	138.9	141.7	0.4247	0.43	0.5225	0.5225
4	4.81	4.81	71.4	69.8	164.8	164.1	0.4261	0.43	0.5694	0.5694
5	4.81	4.81	44.1	32.2	89.76	89.4	0.2605	0.20	0.5694	0.5694
6	1	1	40.5	32.2	89.76	89.4	0.2381	0.20	0.5694	0.5694
7	4.81	4.81	67.9	67.1	2627	2626	8.618	8.61	0	0
8	4.81	4.81	32	32	134.8	134.9	0.4667	0.47	0	0
9	1	1	7	7	134.8	134.9	0.4825	0.48	0	0
10	1	1	7	7	2514	2514	8.975	8.97	0	0

The flow of energy at different components of the SEAC are presented in table 6.

Table 8: Comparison of COP and exergetic efficiency, (a) present model and (b) reference model

Description	**Symbol**	**Load (kW)**		**Heat Exergy (kW)**
		(a)	**(b)**	**(a)**
Absorber	$\dot{Q}_{abs}$	219.5	1086.2	5.142
Condenser	$\dot{Q}_{con}$	205.3	1025	4.937
Evaporator	$\dot{Q}_{evp}$	195.9	1000	12.48
Generator	$\dot{Q}_{gen}$	228.8	1136.3	30.91
COP		**0.8564**	**0.88**	
η_{ex}				**0.4039**

The major parameters which affect the performance (energetic and exergetic) of the solar assisted absorption cycles are the incident solar radiation, ambient temperature, inlet temperature of the working fluid entering the collector, properties of the working fluid of the absorption cycles, percentage of the week and strong solution and geometry of the solar collector. Some of the parameters are discussed in the succeeding sections. The simulations of the solar assisted SEAC are carried out at design conditions and the results are presented in this section. The Fig. 34 shows the variation of COP and cooling load with respect to the generator load provided by solar field. The $\dot{Q}_{evp}$ of the SE absorption cycle decreases with increase in generator load, which effects the COP of the cycle. The COP of the SE absorption cycle is directly proportional to $\dot{Q}_{evp}$, the higher the cooling load, the higher the COP of the system. The higher generator load effects the performance of the system in negative way. The Fig. 35 shows the relationship between the COP and exergetic efficiency with respect to generator temperature. At a fixed values of condenser and evaporator temperature (T_{con} = 32 °C and T_{evp} = 9 °C) respectively, the exergetic efficiency as well as COP decreases with increase in generator temperature. The COP of the SE absorption cycle decreases from 1.089 to 0.6955 and exergy efficiency decreases from 0.7904 to 0.1943 with increase in generator temperature from 323 K to 373 K.

The Fig. 36 shows the variation of COP and exergetic efficiency with respect to evaporator temperature. The COP increases with increase in T_{evp}, in contrast, the exergetic efficiency decreases with increase in T_{evp}. The COP is perceived to increase from 0.8497 to 0.8583 and the exergetic efficiency decreases from 0.3743 to 0.1016 with increase in evaporator temperature from 280 K to 293 K. The exergetic efficiency drops sharply with increase in evaporator temperature.

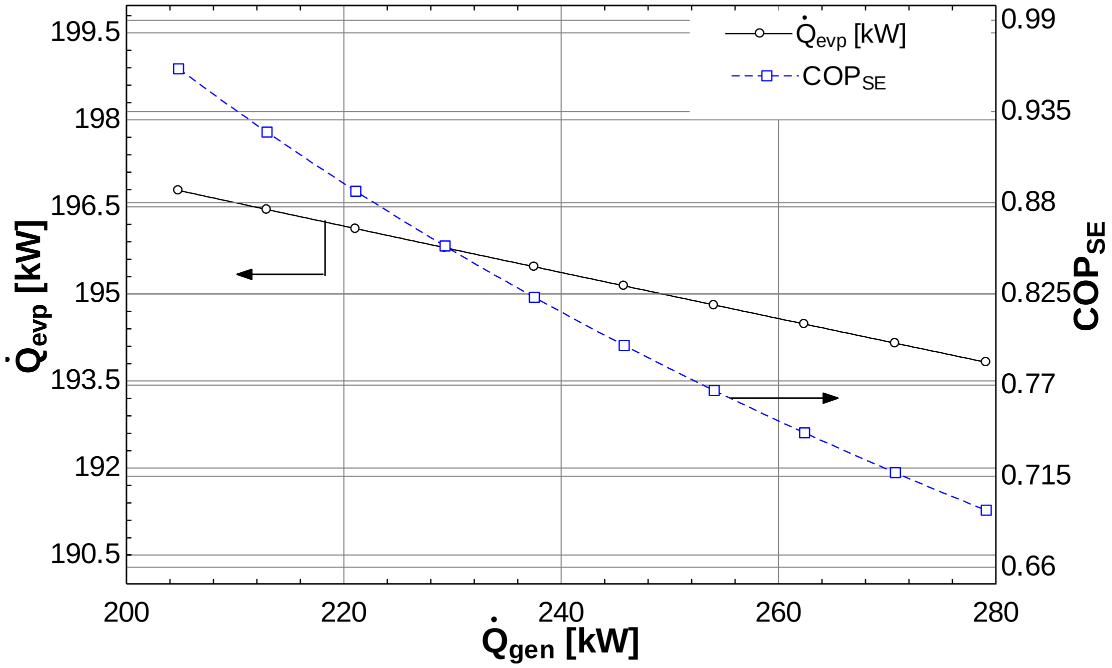

Figure 34: The effect of the generator load on the evaporator load and COP of the SE absorption cycle

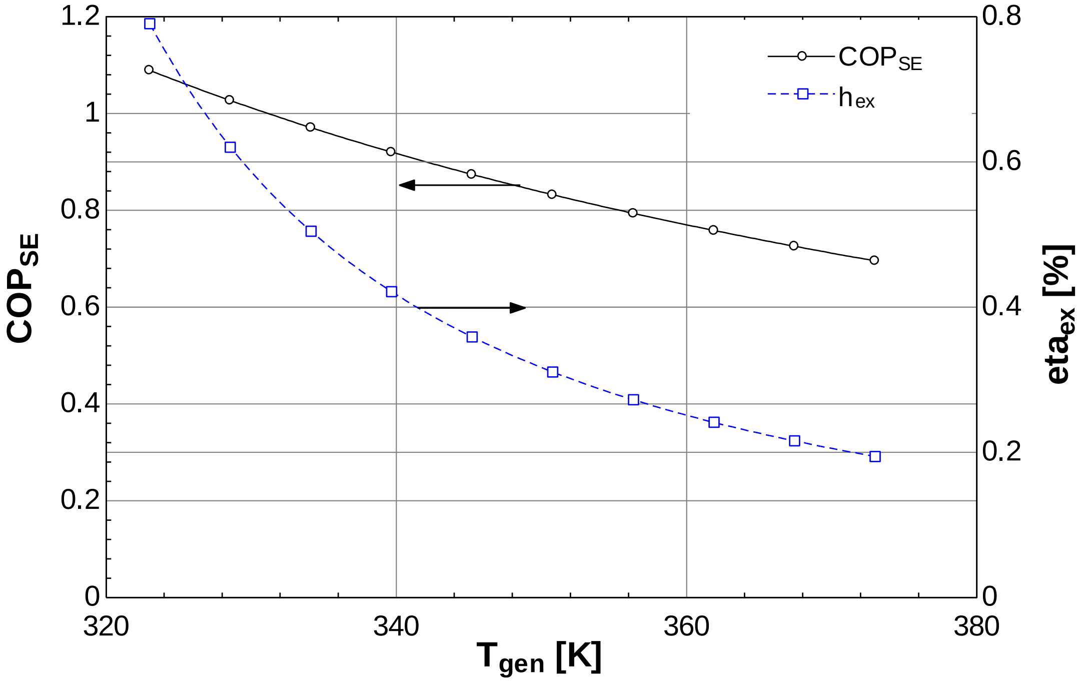

Figure 35: The influence of generator temperature on the COP and exergetic efficiency of the SE absorption cycle

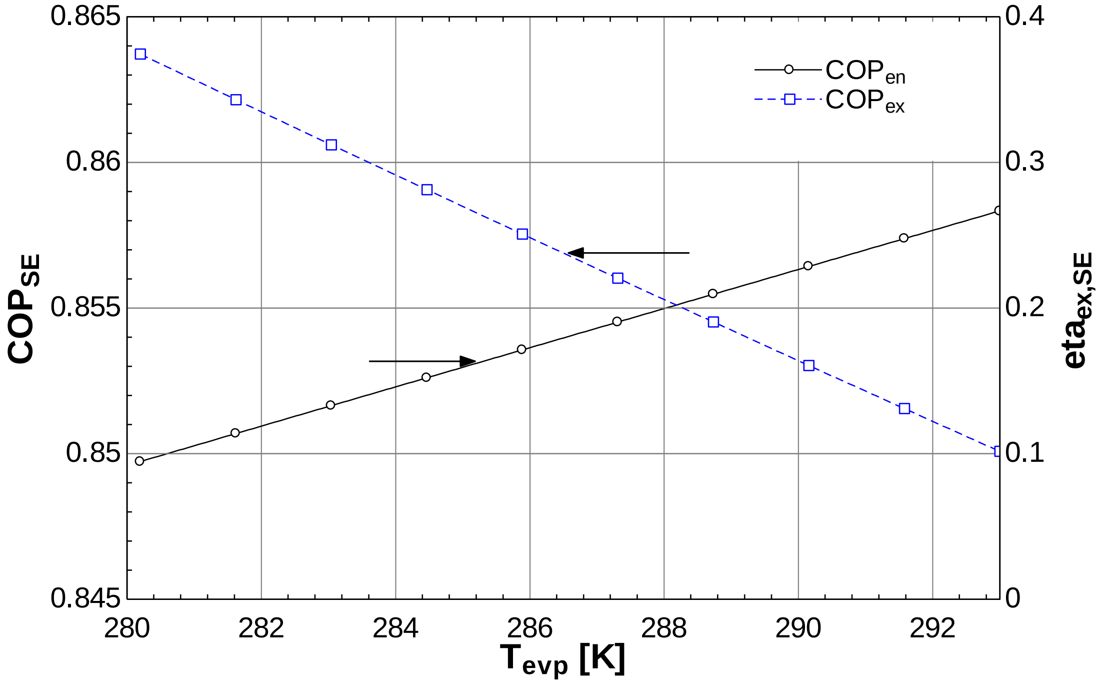

Figure 36: The variation in COP and exergetic efficiency of the SE cycle with increase in evaporator temperature (T_{evp}).

6.4.2 Double effect absorption cycle (DEAC)

The double effect absorption cycle (DEAC) works similar to the SE absorption cycle. The only difference is that the vapour gets produced twice in DE cycle, where in SE cycle the vapour produced only once. Producing vapour in two stages means producing more vapour from the internal heat exchange in-between the generators. The more the vapour produced, the more will be the cooling, which in the end, will have higher COP of the DE absorption cycle.

The input parameters used in analyzing the DE cycle are similar to the ones used for the SE absorption cycle. The system description of the DE cycle is provided in chapter 3 and mathematical modelling of the simulations are presented in chapter 4. The simulation results are validated with the results of reference [131] and are presented in table 8. The flow of energy and exergy at different components of the DEAC are presented in table 9.

Table 9: property comparison of DE cycle, present model (a) with reference model (b) at every point of the present cycle.

Point #	**P (kPa)**		**T (C)**		***h* (kj/kg)**		**s (kj/kg.k)**		**x (%LiBr)**	
	(a)	**(b)**	**(a)**	**(b)**	**(a)**	**(b)**	**(a)**	**(b)**	**(a)**	**(b)**
1	1	1	32	32	69.96	73.2	0.2102	0.22	0.5225	0.5225
2	32.3	32.3	32.4	32	69.96	73.2	0.213	0.22	0.5225	0.5225
3	32.3	32.3	64.4	64.5	138.9	141.7	0.4247	0.43	0.5225	0.5225
4	32.3	4.81	71.4	69.8	164.8	164.1	0.4261	0.43	0.5694	0.5694
5	32.3	4.81	44.1	32.2	89.76	89.4	0.2605	0.20	0.5694	0.5694
6	1	1	40.5	32.2	89.76	89.4	0.2381	0.20	0.5694	0.5694
7	32.3	4.81	67.9	67.1	2627	2626	8.618	8.61	0	0

8	32.3	4.81	32	32	134.8	134.9	0.4667	0.47	0	0
9	1	1	7	7	134.8	134.9	0.4825	0.48	0	0
10	1	1	7	7	2514	2514	8.975	8.97	0	0
11	32.3	32.3	64.06	64.8	138.1	138.1	0.4226	0.44	0.5225	0.5225
12	32.3	32.3	64.06	648	138.1	138.1	0.4226	0.44	0.5225	0.5225
13	32.3	32.3	100.1	106	216.9	230	0.6432	0.68	0.5225	0.5225
14	32.3	32.3	110.1	109	244.6	241	0.6443	0.67	0.5694	0.5694
15	32.3	32.3	77.86	65	158.7	148	0.4638	0.41	0.5694	0.5694
16	32.3	32.3	105.1	107.9	2695	2700	7.928	7.94	0	0
17	32.3	32.3	70.8	70.8	1480	296	0.9649	0.97	0	0
18	32.3	32.3	70.8	70.6	163.7	167	0.4227	0.44	0.5694	0.5694

Table 10: The results of the DE absorption cycle analyzed in the present study.

Description	**Symbol**	**Load (kW)**	**Heat Exergy (kW)**
Absorber	$\dot{Q}_{abs}$	215.9	4.827
Condenser	$\dot{Q}_{con}$	140	6.278
Evaporator	$\dot{Q}_{evp}$	195.2	12.44
Generator	$\dot{Q}_{gen}$	1601	34.06
COP		**1.215**	
$\boldsymbol{\eta_{ex}}$			**0.3887**

As discussed earlier, the performance of the DE absorption cycle is higher in comparison to SE cycle. The Fig. 37 shows the comparison of COP and exergetic efficiency with increase in generator temperature. Both COP and η_{ex} decreases with increase in $T_{gen.}$ The COP of the DE cycle is higher at low T_{gen} but starts to decrease with increase in $T_{gen.}$ The COP decreases from 1.663 to 1.058 and η_{ex} decreases from 0.4756 to 0.2486 with increase in T_{gen} from 353 K to 400 K. The Fig. 38 shows the COP and the cooling load in regard to percentage of the weak solution. The COP of the DE cycle increases with increase in %age of the weak solution, in contrast, the cooling load decreases with increase in %age of the weak solution at a fixed condenser and evaporator temperatures of 305 K and 208 K. The COP is also observed to increase with increase in evaporator temperature.

The effect of %age of the strong solution on exergetic efficiency (η_{ex}) and COP of the DE cycle is shown in Fig. 39. The increase in the %age of the strong solution decreases the η_{ex} and COP of the DE cycle. The COP is observed to be higher at low %age of strong solution, and starts to fall down with increase in %age. The same effect is observed with η_{ex} and it also decreases with increase in %age of strong solution at a fixed condenser and evaporator temperature of 312 K and 284 K. The η_{ex} is observed to increase with decrease in evaporator temperature (T_{evp}) and the COP decreases with decrease in $T_{evp.}$

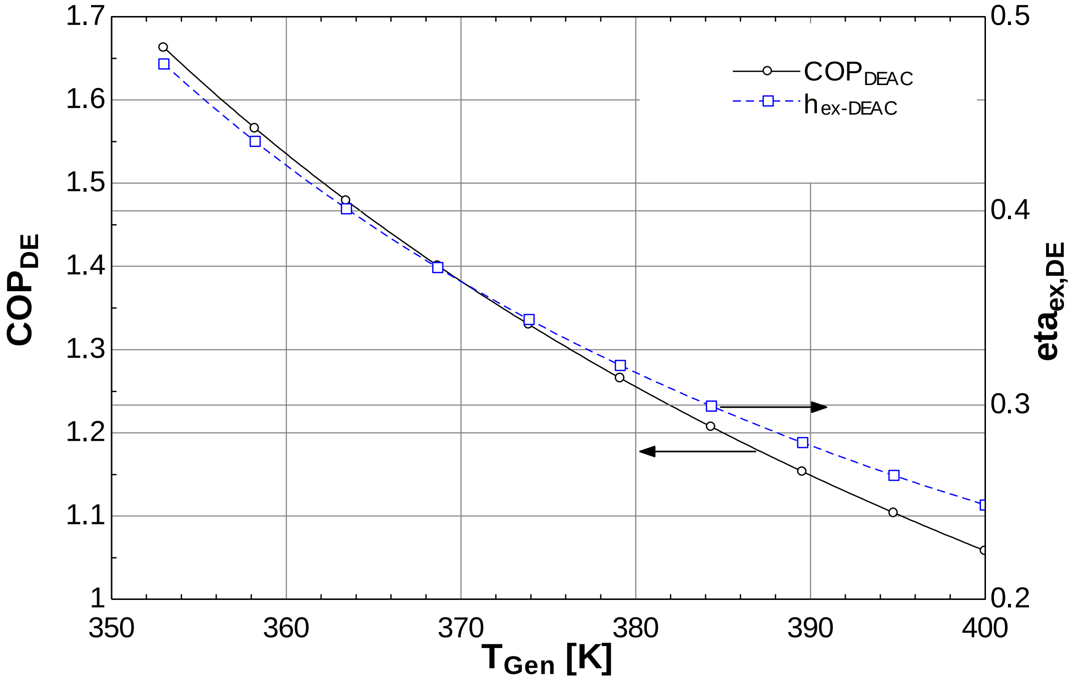

Figure 37: The impact of Tgen on the COP and exergetic efficiency of the DE cycle

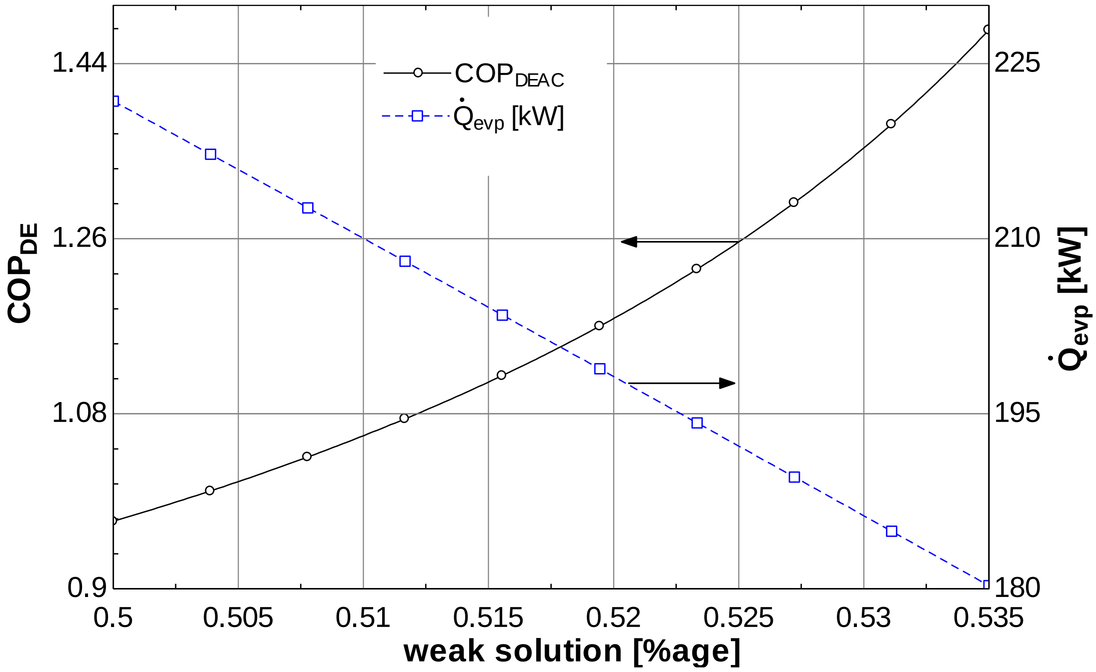

Figure 38: The deviation in between the COP and evaporator load of the DE cycle with respect to weak solution percentage.

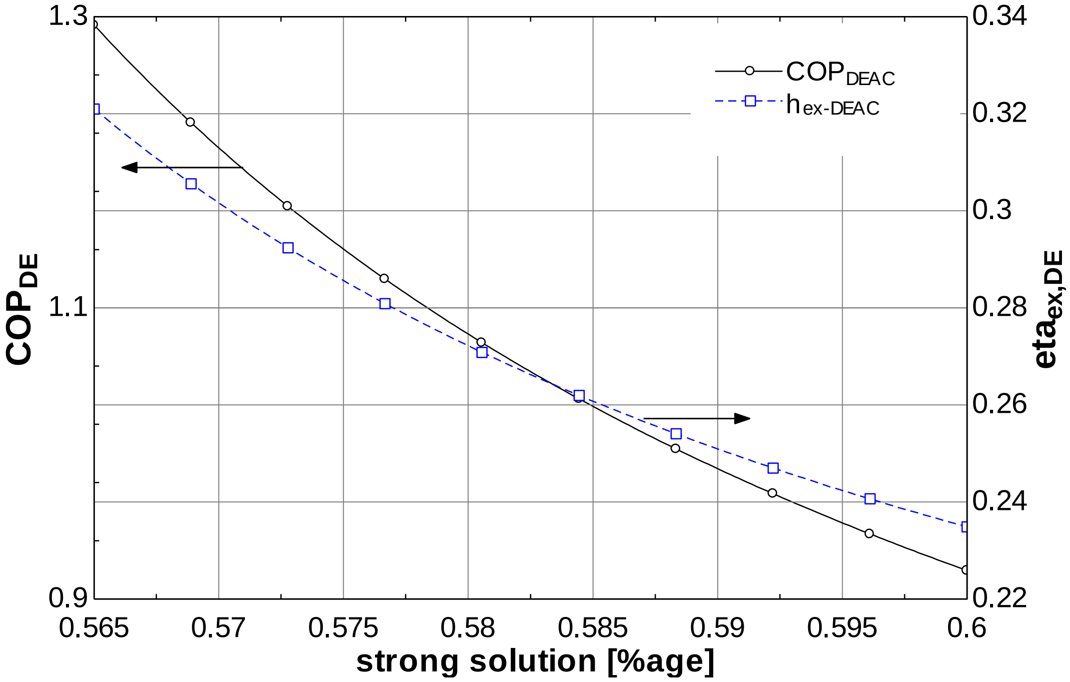

Figure 39: The effect of strong solution percentage on COP and exergetic efficiency of the DE cycle

6.4.3 Triple effect absorption cycle (TEAC)

As the number of stages of the generators increase, the performance of the cycles increase. The triple effect (TE) absorption cycle has three stages of vapour generation, which forms an extension of the DE absorption cycle where, vapour gets produced in two stages. The more is the vapour, the more will be the cooling capacity. The higher cooling capacity will have higher COP of the cycle. All these cycles are based on the SE cycle, therefore, the input variables and operating conditions are considered same for all the cycles. The TE cycle has higher COP in comparison to SE and DE cycles. It needs lower heat input as compared to SE cycle, but it requires a higher temperature heat source to operate.

The simulations of TE cycle are performed and analyzed using thermodynamic equations. The system description of the cycle is explained with the help of schematic diagrams in chapter 3. The mathematical model and working principle of the TE cycle is described in detail in chapter 4. The model simulations are validated with the reference model presented by ref. [105].

The properties of the TE cycle at each state point is calculated using the simulation program called EES developed by S. A. Klein [122]. The thermodynamic properties of the TE cycle presented in table 9 are in good agreement with the reference model [105]

Table 11: Properties of triple effect absorption cycle at every point of the cycle

Point #	**P(kPa)**	**T(K)**	***h*(kj/kg)**	**s(kj/kg.k)**	**x (%LiBr)**
1	1	304.8	69.26	0.2079	0.5225
2	134.1	304.8	69.36	0.2079	0.5225
3	134.1	336.8	137.3	0.4201	0.5225
4	134.1	336.8	137.3	0.4201	0.5225
5	134.1	336.8	137.3	0.4201	0.5225
6	134.1	371.8	213.8	0.6349	0.5225
7	134.1	371.8	213.8	0.6349	0.5225
8	134.1	371.8	213.8	0.6349	0.5225
9	134.1	409.8	298.5	0.8503	0.5225
10	134.1	421.8	325.9	0.8454	0.5694
11	134.1	373.9	233.6	0.5933	0.5694
12	134.1	391.8	262.6	0.6905	0.5694
13	134.1	382.8	242.3	0.6423	0.5694
14	134.1	373.9	158.9	0.5933	0.5694
15	134.1	352.4	180.9	0.4719	0.5694

16	134.1	363.1	165.5	0.5333	0.5694
17	134.1	373.9	91.45	0.5933	0.5694
18	1	313.7	91.45	0.2381	0.5694
19	134.1	415.8	2759	7.439	0
20	134.1	381.2	1471	1.397	0
21	134.1	381.8	2677	7.264	0
22	134.1	381.2	584	1.397	0
23	134.1	344.6	2565	6.939	0
24	134.1	304.8	136.8	0.4725	0
25	1	280.1	136.8	0.1059	0
26	1	280.2	2514	8.975	0

The effect of generator temperature on COP and the exergy efficiency of the TE absorption cycle is shown in table 10. It is observed from the table that the COP of the TE cycle increases with increase in $T_{evp.}$ But it starts to decrease with increase in T_{gen}. The exergy efficiency shows the downward trend with increase in T_{evp}. It decreases from 0.5252 to 0.343 with increase in T_{evp} from 7℃ to 13℃. The η_{ex} also decreases with increase in T_{gen} from 400 K to 450 K.

Table 12: Variation of COP and ηex at various evaporator temperatures with respect to generator temperature

T_{gen} (K)	**@ T_{evp} =7℃**		**@ T_{evp} =9℃**		**@ T_{evp} =11℃**		**@ T_{evp} =13℃**	
	COP	η_{ex}	COP	η_{ex}	COP	η_{ex}	COP	η_{ex}
400	2.183	0.5252	2.186	0.4638	2.19	0.403	2.193	0.343
405.6	2.055	0.4853	2.058	0.4286	2.062	0.3724	2.065	0.3169

411.1	1.941	0.4502	1.944	0.3975	1.947	0.3455	1.95	0.294
416.7	1.838	0.419	1.841	0.37	1.844	0.3216	1.847	0.2736
422.2	1.746	0.3912	1.749	0.3455	1.751	0.3002	1.754	0.2555
427.8	1.662	0.3663	1.664	0.3235	1.667	0.2811	1.67	0.2392
433.3	1.585	0.3439	1.588	0.3037	1.59	0.2639	1.593	0.2246
438.9	1.515	0.3236	1.517	0.2857	1.52	0.2483	1.522	0.2113
444.4	1.45	0.3052	1.453	0.2695	1.455	0.2342	1.457	0.1993
450	1.391	0.2884	1.393	0.2547	1.395	0.2213	1.398	0.1883

The effect of T_{evp} on the COP and exergetic efficiency is presented in Fig. 40. The COP of the TE cycle increases linearly with increase in $T_{evp.}$ The COP of the cycle increases from 1.752 to 1.773 and η_{ex} drops from 0.39 to 0.063 with increase in T_{evp} from 280 K to 293 K at fixed generator and condenser temperature of 422 K and 305 K. The COP of SE, DE and TE cycles is displayed in Fig. 41 with variation in generator temperature. The TE cycle has the highest COP among all the cycles. The COP of the triple effect cycle is observed to be 31.66% higher as compared to double effect cycle and is noticed to be more than twice the single effect cycle. The TE cycle operates at higher temperature and pressures, and requires less heat input at higher source temperatures, on the other hand produces the higher cooling effect in comparison to single and double effect cycles. The internal heat exchange in-between the low and medium temperature generators of the double and triple effect cycles help in higher vapour production in comparison to single effect cycle. The higher vapour production results in higher COP of the absorption cycles.

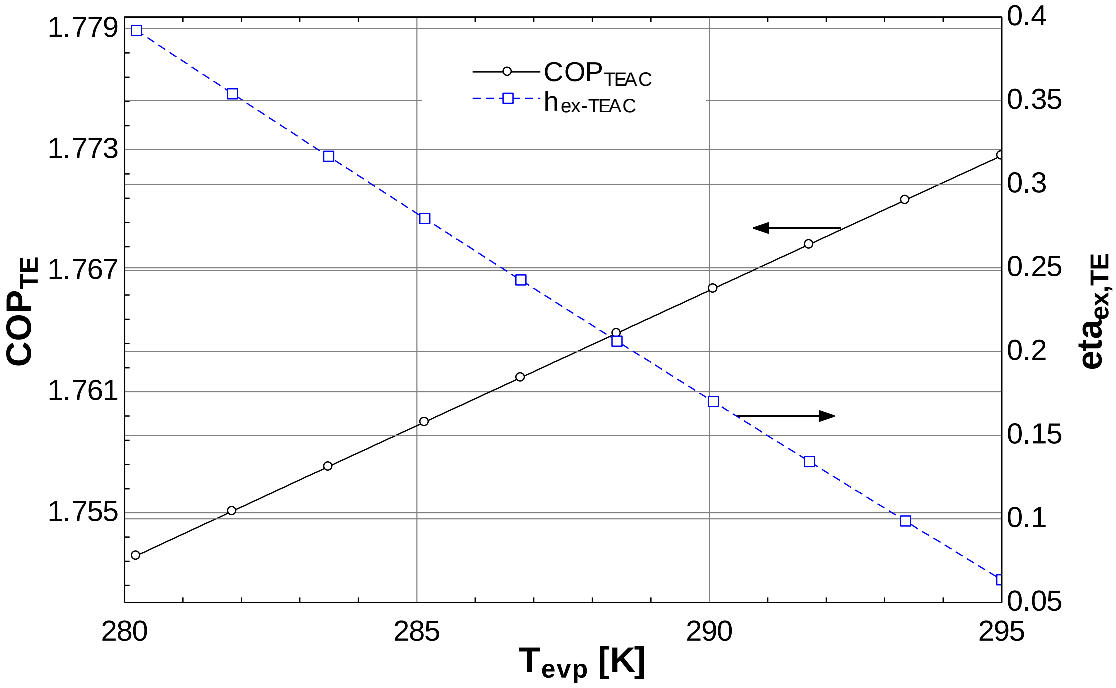

Figure 40: The impact of evaporator temperature (T_{evp}) on the COP and exergetic efficiency of the TE cycle.

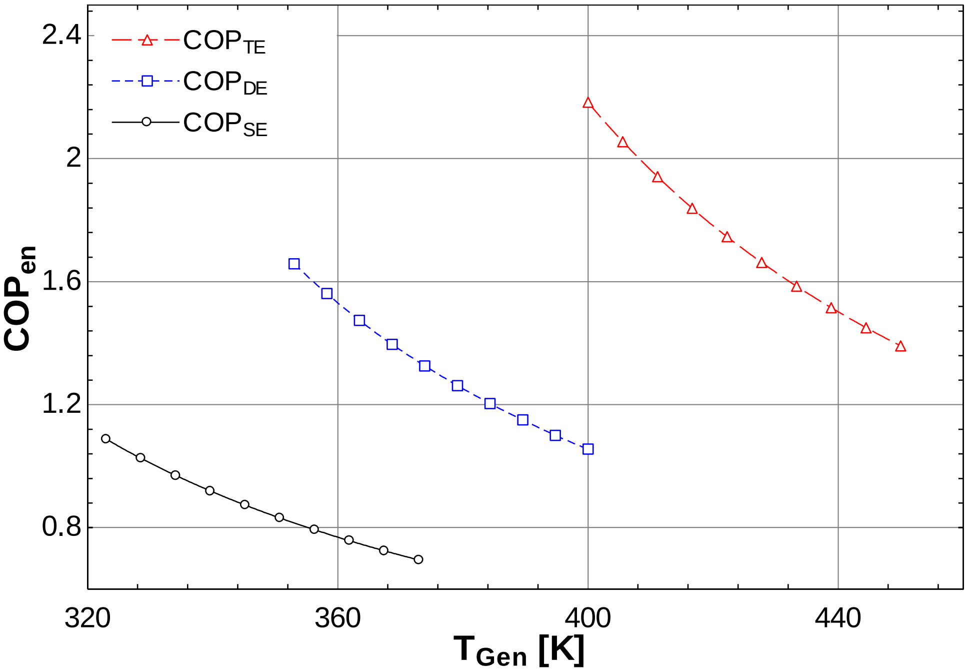

Figure 41: The impact of Tgen on the COP of SE, DE and TE cycles

6.4.4 Quadruple effect absorption cycle (QEAC)

The QE absorption cycle is modelled and simulated using the EES software proposed by S. A. Klein [122]. The properties of LiBr-H_2O mixture are evaluated from the correlations presented by [103, 105, and 106]. These correlations are effective for temperatures up to 500 K [143] and are applied to quadruple effect cycle as it work within this temperature range. The modelled code for QEAC is the extension of the triple effect cycle which has been studied in detail [105, 106].

The operating parameters such as, evaporator temperature, condenser temperature, generator temperature, effectiveness of the heat exchangers and finally the evaporator load is studied. The enthalpy values are calculated at each state point to find the energy and exergy values of the cycle. The properties of the QE cycle are presented in table 11. The thermodynamic analysis of the QEAC is conducted by applying the laws of mass conservation, concentration conservation and first and second laws of thermodynamics (discussed in chapter 4).

Table 13: Properties of quadruple effect absorption cycle at each state point

Point #	**P(kPa)**	**T(K)**	***h*(kj/kg)**	**s(kj/kg.k)**	**x (%LiBr)**
1	1	304.8	69.26	0.2079	0.5225
2	402.2	305.2	69.56	0.2107	0.5225
3	402.2	337.2	138.1	0.4226	0.5225
4	402.2	337.2	138.1	0.4226	0.5225
5	402.2	337.2	138.1	0.4226	0.5225
6	402.2	371.2	212.5	0.6314	0.5225
7	402.2	371.2	212.5	0.6314	0.5225
8	402.2	371.2	212.5	0.6314	0.5225

9	402.2	408.2	294.9	0.8416	0.5225
10	402.2	408.2	294.9	0.8416	0.5225
11	402.2	408.2	294.9	0.8416	0.5225
12	402.2	446.2	380.8	1.042	0.5225
13	402.2	471.2	431.9	1.082	0.5694
14	402.2	427.1	338.3	0.8718	0.5694
15	402.2	422.2	326.7	0.8474	0.5694
16	402.2	424.7	334.9	0.8596	0.5694
17	402.2	387.2	245	0.6661	0.5694
18	402.2	384.2	246.7	0.6497	0.5694
19	402.2	385.7	245.5	0.6579	0.5694
20	402.2	351.8	164.5	0.4682	0.5694
21	402.2	352.2	180.5	0.4708	0.5694
22	402.2	352	169.3	0.4695	0.5694
23	402.2	319.2	94.54	0.273	0.5694
24	1	313.7	94.54	0.2381	0.5694
25	402.2	458.7	2830	7.104	0
26	402.2	417	1609	1.779	0
27	402.2	415.2	2790	7.014	0
28	402.2	378.2	724.5	1.364	0
29	402.2	377.7	2723	6.856	0
30	402.2	344.2	75.23	0.9681	0
31	402.2	344.7	2580	6.515	0
32	402.2	304.8	137	0.4596	0
33	1	280.1	137	0.1059	0
34	1	280.2	2514	8.975	0

The Fig. 42 displays the variation in COP of SE, DE, TE and quadruple effect cycles at a fixed condenser and generator temperature (T_{con} = 305 K, T_{gen} = 471 K) and T_{evp} = 280 K, with increase in percentage of the weak solution. The COP of all the cycles increase with increase in the concentration of the weak solution. The highest COP is observed for QE cycle followed by TE cycle. The higher COP is resulted from the vapour separation from the solution, in QE cycle, the vapour gets distributed in four generators. The vapour production of four generators produces higher cooling effect. The Fig. 43 shows the variation of COP with increase in concentration of the strong solution. It is witnessed that the COP decreases with increase in %age of the strong solution. The higher concentration of the strong solution would produce less amount of vapour, which causes the COP to go down at higher concentration of strong solution. The relation between the exergetic efficiency (η_{ex}) of the SE, DE, TE and QE absorption cycles with respect to T_{gen} is presented in Fig. 44. The η_{ex} of SE cycle is observed to be higher at low temperatures, but drops sharply with increase in $T_{gen.}$ In contrast, the η_{ex} of the DE cycle is lower than SE, but decreases slowly with increase in $T_{gen.}$ The η_{ex} of the DE cycle decrease from 0.4756 to 0.248 and the η_{ex} of the TE cycle decreases from 0.5252 to 0.288. The η_{ex} of the QE cycle is highest in comparison to all other cycles. It starts to decrease from 0.5304 and ends at 0.317, which shows that the QE cycle has greater potential to produce useful work at higher temperatures.

The Fig's 45 and 46 show the relation in-between the COP and T_{gen} of the all the four cycles. Both figures portray the COP comparison of the absorption cycles, but at different $T_{evp.}$ The increase in evaporator temperature (T_{evp}) from 280 K to 286 K increases the η_{ex} of the QE cycle by 0.324% followed by TE cycle, where the increment is 0.319%. The higher evaporator temperature helps in increasing the cooling production which results in higher COP of the cycles. The COP of the QE cycle is

21.36% higher than TE cycle and it is 2.55 times higher than SE cycle, The COP of the QE cycle is also noticed to be 1.7 times higher than DE cycle at an evaporator temperature of 286 K. The internal heat exchange in-between the low and medium temperature generators of the double and triple effect cycles help in higher vapour production in comparison to single effect cycle. The vapour production is observed to be the highest for the quadruple effect cycle. The vapour production increases further with the change in the mass distribution among the low, medium and high temperature generators. The effect of mass distribution among the generators is presented in Fig. 47. The COP of the quadruple effect cycle is observed to be the highest by providing 40% of the total system mass to the low temperature generator. The little modification in the mass distribution affects the COP of the absorption cycles strongly, without the addition of any extra amount of heat.

On the other hand, the increase in mass concentration to the low temperature generator decreases the cooling capacity of the of the absorption cycles as well as increases the risk of crystallization of the LiBr-H_2O solution in the absorber.

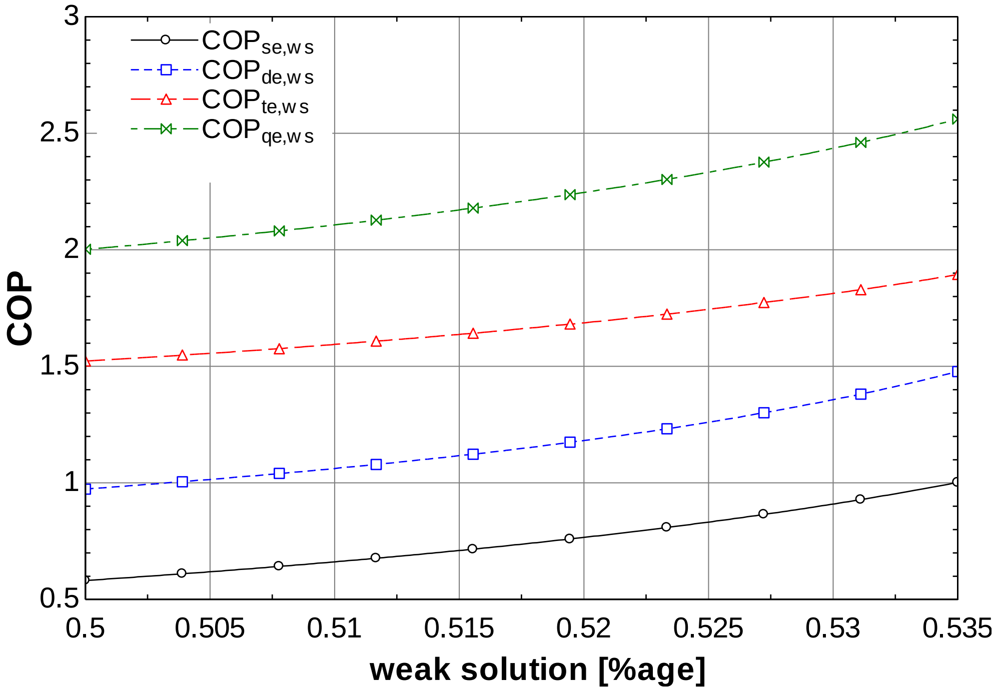

Figure 42: The effect of weak solution percentage on the COP of the single, double, triple and quadruple effect absorption cycles

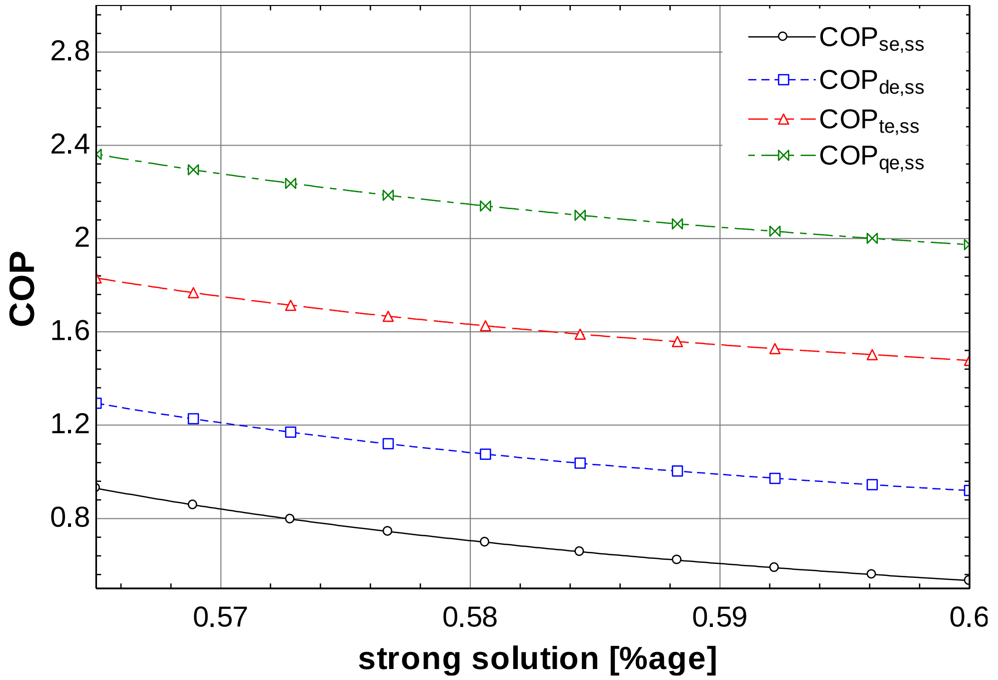

Figure 43: The relation between the percentage of strong solution and COP of the single, double, triple and quadruple effect absorption cycles

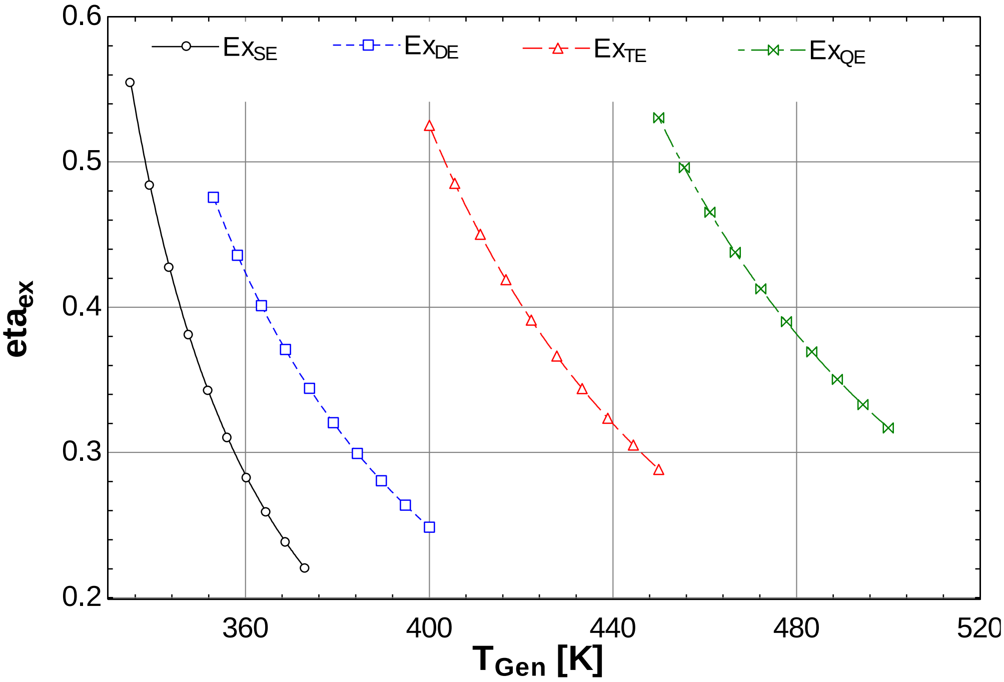

Figure 44: The influence of Tgen on the exergetic efficiency of four different absorption cycles

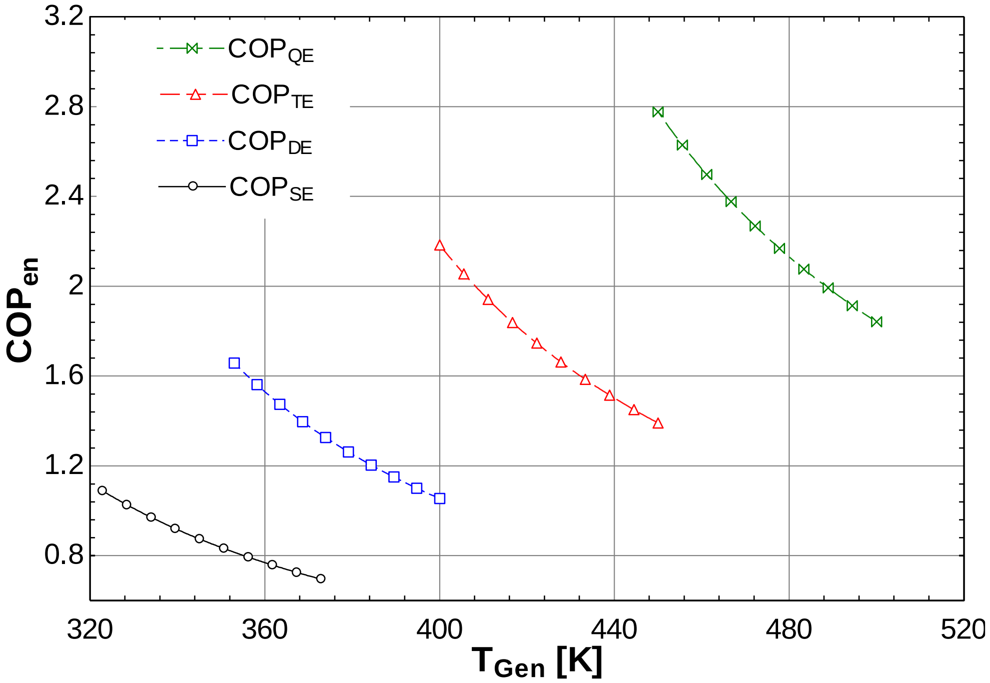

Figure 45: The influence of generator temperature (Tgen) on the COP of all four absorption cycles at an evaporator temperature (T_{evp}) of 280 K.

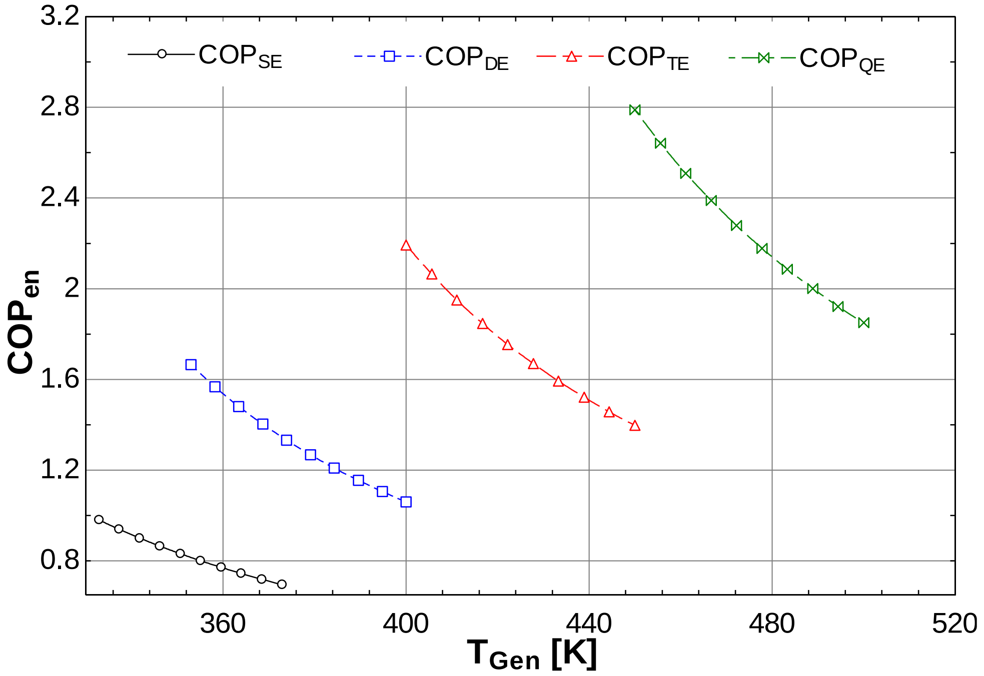

Figure 46: The influence of generator temperature (Tgen) on the COP of all four absorption cycles at an evaporator temperature (T_{evp}) of 286 K.

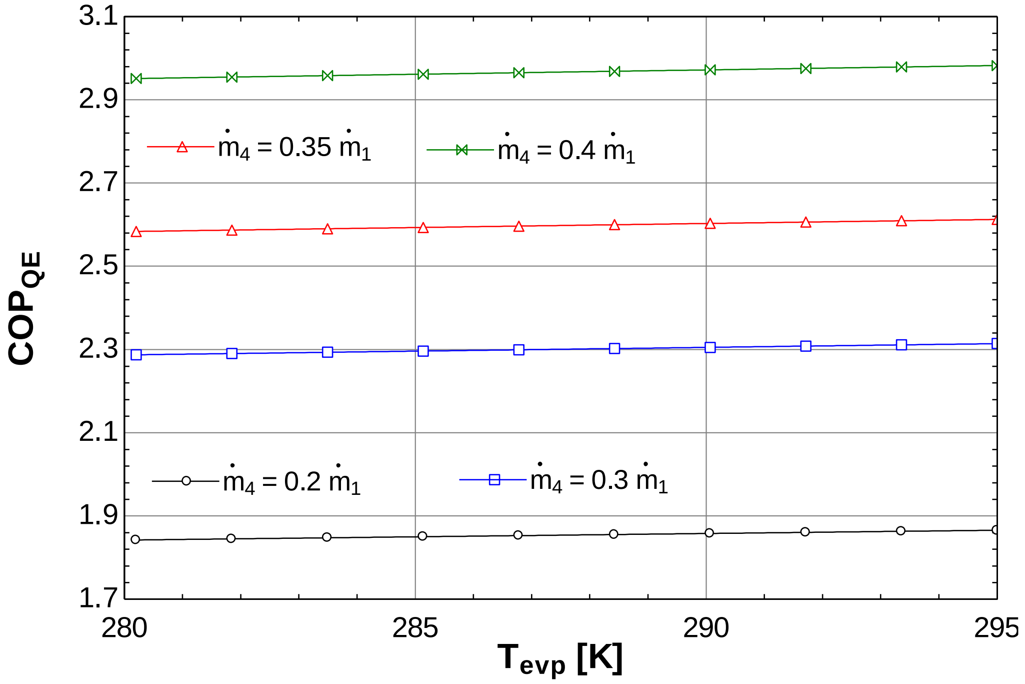

Figure 47: Effect of mass distribution in the low temperature generator of the quadruple effect cycle.

Chapter 7

CONCLUSIONS AND RECOMMENDATIONS

7.1 Conclusions

This comparative study is carried out to evaluate the energetic and exergetic performance of solar assisted power generation and multi-effect absorption cycles. Solar heat is collected using PT and PD solar collectors. The heat transfer fluids employed in solar collectors are Al_2O_3 and Fe_2O_3 water based nanofluids. The performance of the water based nanofluids is compared with pure water to observe the effect of nanofluids on the thermophysical properties of base fluids. In the first part of the analysis, nanofluids are prepared and tested in parabolic trough solar collectors both numerically as well as experimentally. The simulations are performed to analyze solar collectors of PT and PD at different design conditions. The solar collectors are further evaluated upon integration with Rankine cycle to generate electric power. In the second part of the analysis, the absorption cycles of single, double, triple and quadruple are simulated and analyzed individually as well as together to evaluate their performance on comparative basis. The following are the conclusions drawn from the conducted research:

7.1.1 Nanofluids

Nanofluids are observed to have better thermophysical properties than the base fluids of water. The thermal conductivity, density and viscosity of the Al_2O_3-water based nanofluid is observed to be 6.84%, 6.73% 6.24% higher than base fluids of water at room temperature, these properties are found to increase with increase in temperature.

The nanoparticles in solid form possess low heat capacity as compared to pure water, consequently there solution will have lower values of Cp as compared to water. The same effect is observed for Fe_2O_3 water based nanofluids, where the density effect is observed to be 7.87% higher in comparison to water. The thermal conductivity effect is observed to be 4.39% higher than pure water. The C_p is observed to be 9.3% lower than that of pure water at a temperature of 300 K.

7.1.2 Solar Collectors

The nanofluids discussed above are used as HTFs in both, PD and PT collectors. There are many factors which are considered to be responsible to affect the performance of PT collectors. Convection heat transfer coefficient is reflected as the key factor to affect the efficiency of solar collectors. The greater values of convection coefficient lead to the lower absorber temperature which, in result, lowers the heat losses from the collector. It is observed that the convection heat transfer coefficient for Al_2O_3-water based nanofluid is 56.5 higher followed by Nusselt number which is 46.3% higher as compared to pure water. The overall heat transfer coefficient for nanofluids is observed to be 4.32% higher than pure water. The outlet temperature of the PT collector for Fe_2O_3 water based nanofluid is observed to be 1.7% higher than water. The performance parameters such as, heat transfer rate and net power produced are observed to be about 7-8% higher for parabolic dish solar collectors for both nanofluids.

7.1.3 Absorption Cycles

The absorption cycles are designed to work on LiBr-H_2O solution, and to be externally heated by solar heat available from solar collectors. Some concluding remarks, drawn from the performed study, are as follows:

- The quadruple effect absorption cycle has the highest COP among other cycles analyzed in this study.
- The COP of the quadruple effect absorption cycle is 21.36% higher than triple effect absorption cycle and it is 2.55 times higher than SE cycle. It is also noticed to be 1.7 times higher than DE cycle at an evaporator temperature of 286 K.
- The exergetic efficiency of the QE absorption cycle is observed to be 11.1% higher than SE absorption cycle. It is observed that the TE cycle has 4.74% higher exergetic efficiency in comparison to SE cycle at an evaporator temperature of 280 K.
- The QE cycle needs about 63% less heat input as compared to SE cycle to produce the same cooling effect.
- The COP of the absorption cycles is witnessed to increase with distribution of the mass flow rate among the generators. The highest COP (QE cycle) was observed to be at 40% of the total mass provided to the low temperature generator.
- The QE cycle needs a temperature of about 2.64 times higher than SE cycle to operate under same operating conditions.

The conclusions drawn above provide an idea how nanofluids effect the performance of solar collectors. The nanofluids affect the heat transfer properties, such as, thermal conductivity and convection heat transfer coefficient of the base fluids, because nanoparticles in their original form, have higher thermal properties. It is observed that the particle size and the percentage of nanoparticles are two major parameters, which are considered to play an important role in enhancing heat transfer properties.

Therefore, these parameters have to be chosen sensibly, because of the unpredictable behavior of nanoparticles. Apart from the high thermophysical properties of nanofluids, there are concerns which need to be clarified for the commercial application of nanofluids. The first is the Cp of nanofluids which is low in comparison to base fluids, the Cp of the working fluids needs to be higher to absorb more heat. The second major concern is the high cost of nanofluids, which is considered as the main hindrance for nanofluids to have their industrial applications. The other concerns such as, oxidation, segregation, agglomeration and settlements of nanoparticles have adverse effect on the system performance. Therefore, even though the rate of heat transfer increases by several percentage, the practical implication of nanofluids needs to be carefully evaluated.

7.2 Recommendations and future work

System integration analysis of the solar assisted power generation and absorption cooling offers several main areas of future research which are summarized below,

- Apart from the thermophysical properties of the nanoparticles, the effect of nanoparticle’s shape, size and pH value should be considered in the analysis of nanofluids. The metallic nanoparticles (A_u, A_g, C_u) shall also be included in the future research to be compared with metal oxide (Al_2O_3) nanofluids.
- The experimental analysis should be performed simultaneously on two identical systems, one working on nanofluids and the other one working on water, so their results can be compared under identical operating conditions.
- Simulations of the mathematical models are carried out for their thermodynamics (first and second law of thermodynamics) analysis only, their analysis need to be extended further to perform their economic as well as

environmental analysis. The required capital investment and operating cost for the power along with cooling production should be explored.

- The integrated system shall be extended further to use the waste heat through the integration of the Kalina cycle to generate electricity from the low grade temperature heat.
- The geometry effects of the solar collectors shall be considered in the further research, because the geometry effects play an important role in convection heat transfer.
- The absorption cycles should also be analyzed using different working fluids ($LiCl-H_2O$, NH_3-H_2O) as well as to be operated with heat sources (geothermal, biomass) other than solar energy.

REFERENCES

[1] E. Bellos, C. Tzivanidis, K.A. Antonopoulos, G. Gkinis. (2016). Thermal enhancement of solar parabolic trough collectors by using nanofluids and converging-diverging absorber tube. *Renewable Energy* 94 213-222

[2] Yimin X., Li Q. (2003). Investigation of convective heat transfer and flow features of nanofluids. *Journal of heat transfer* (25), 151-155

[3] Lee, S., Choi, S. U. S., Li, S., and Eastman, J. A. (1999). Measuring Thermal Conductivity of Fluids Containing Oxide Nanoparticles, *J. Heat Transfer* 121, pp. 280–289.

[4] Solangi K. H, Islam M. R, Saidur R, Rahim NA, Fayaz H. (2011). A review on global solar energy policy. *Renewable and Sustainable Energy Reviews*; 15(4): 2149–63.

[5] Mekhilef S, Saidur R, Safari A. (2011). A review on solar energy use in industries. *Renewable and Sustainable Energy Reviews*. 15(4): 1777–90.

[6] R. Saidur, G. Boroumand Jazi, S. Mekhlif, M. Jameel. (2012). Exergy analysis of solar energy applications. *Renewable and Sustainable Energy Reviews* 16: 350–356.

[7] Yousefi T, VeysiF, Shojaeizadeh E, Zinadini S. (2012). An experimental investigation on the effect of Al_2O_3–H_2O nanofluids on the efficiency of flat-plate solar collectors. *Renew Energy* 39 (1): 293–298.

[8] Fernández-García A., E. Zarza, L. Valenzuela, M. Pérez. (2010). Parabolic-trough solar collectors and their applications, *Renewable Sustainable Energy Rev*. 14 (7): 1695-1721.

[9] Choi, S.U.S. (1995). Enhancing thermal conductivity of fluids with nanoparticles. In: *Proceedings of the 1995 ASME International Mechanical Engineering Congress and Exposition*. San Francisco, CA, USA.

[10] Eastman J. A., Choi S. U. S. S., Li W. Yu, and L. J. (2001). Anomalously increased effective thermal conductivities of ethylene glycol-based nanofluids containing copper nanoparticles. *Thompson, Appl. Phys.* Lett. 78, 718.

[11] Roetzel W., Y. Xuan. (2000). Conceptions for heat transfer correlation of nanofluids, *Int. J. Heat Mass Transfer* 433701–3707.

[12] Li Y., J. Zhou, S. Tung, E. Schneider, Xi S. (2009). A review on development of nanofluid preparation and characterization, *Powder Technol*. 196 89–101.

[13] Dongsheng Wen and Yulong Ding (2004). Effective Thermal Conductivity of Aqueous Suspensions of Carbon Nanotubes (Carbon Nanotube Nanofluids) *Journal of Thermophysics and Heat Transfer*, Vol. 18, No. 4 pp. 481-485. http://dx.doi.org/10.2514/1.9934

[14] Natarajan E., Sathish R. (2009). Role of nanofluids in solar water heater. *Int J Adv Manuf Technol.* doi: 10.1007/S00170-008-1876-8

[15] Masuda H, Ebata A, Teramae K, Hishinuma N. (1993). Alteration of thermal conductivity and viscosity of liquid by dispersing ultra-fine particles (dispersion of g- Al_2O_3, SiO_2 and TiO_2 ultra-fine particles*). Netsu Bussei (Japan).* 7: 227-33.

[16] Grimm A. (1993). Powdered aluminum-containing heat transfer fluids. *German Patent DE* 4131516 A1

[17] Zhu D,Li X, Wang N, Wang X, Gao J, Li H. (2009). Dispersion behavior and thermal conductivity characteristics of Al2O3–H2O nanofluids. *Curr Appl Phys* 9:131–9.

[18] Wu C,Cho TJ ,Xu J, Lee D,Yang B, Zachariah MR. (2010). Effect of nanoparticle clustering on the effective thermal conductivity of concentrated silica colloids. *Nanoscale Res Lett* 81:011406.

[19] Younes H, Christensen G, Luan X, Hong H, Smith P. (2012). Effects of alignment, pH, surfactant, and solvent on heat transfer nanofluids containing Fe_2O_3 and CuO nanoparticles. *Appl. Phys;* 111:064308.

[20] Xie H, Wang J, Xi T, Liu Y, Ai F. (2002). Thermal conductivity enhancement of suspensions containing nano-sized alumina particles. *J Appl Phys;* 91 (7):4568–72, http://dxdoi.org/10.1063/1.1454184.

[21] Li X F, Zhu DS, Wang XJ, Wang N, Gao NW, Li H. (2008). Thermal conductivity enhancement dependent pH and chemical surfactant for Cu-H2O nanofluids. *Thermo chim Acta*; 69:98–103.

[22] Zhou M, Xia G, Li J, Chai L, Zhou L. (2012). Analysis of factors influencing thermal conductivity and viscosity in different kinds of surfactant solutions. *Exp Therm Fluid Sci.* 36:22 (22).

[23] Wang X, Zhu D, Yang S. (2009). Investigation of pH and SDBS on enhancement of thermal conductivity in nanofluids. *Chem Phys Lett* 470:107–11.

[24] Lee D, Kim JW, Kim BG. (2006). A new parameter to control heat transport in nanofluids: surface charge state of the particle in suspension. *Phys Chem B* 110:4323–8.

[25] Gowda R, Sun H, Wang P, Charmchi M, Gao F,Gu Z, Budhlall B. (2010). Effects of particle surface charge, species, concentration and dispersion method on the thermal conductivity of nanofluids. *Advances in Mechanical Engineering* (Article ID 807610, 10p. doi:10.1155/2010/807610).

[26] Thomas S., C. Sobhan. (2011). A review of experimental investigations on thermal phenomena in nanofluids, *Nanoscale Res. Lett*. 6 377

[27] Wang, X., Xu, X., and Choi, S. U. S. (1999). Thermal Conductivity of Nanoparticle-Fluid Mixture. *Journal of Thermophysics and Heat Transfer*, vol. 13, pp. 474–480,

[28] Pak, B., and Cho, Y. I. (1998). Hydrodynamic and Heat Transfer Study of Dispersed Fluids with Submicron Metallic Oxide Particle, *Experimental Heat Transfer*, vol. 11, pp. 151–170.

[29] Choi, S. U. S., Zhang, Z. G., and Keblinski, P. (2004). Nanofluids, in Encyclopedia of Nanoscience and Nanotechnology. *American Scientific Publishers, Los Angeles, Calif*. vol. 6, pp. 757–773

[30] Das, S. K., Putra, N., and Roetzel, W. (2003). Pool Boiling Characteristics of Nano-Fluids, *International Journal of Heat and Mass Transfer*, vol. 46, no. 5, pp. 851–862

[31] Sarit Kumar Das , Stephen U. S. Choi & Hrishikesh E. Patel (2006) Heat Transfer in Nanofluids—A Review, *Heat Transfer Engineering*, 27:10, 3-19, DOI: 10.1080/01457630600904593

[32] Choi, S. U. S. (1995). Enhancing Thermal Conductivity of Fluids with Nanoparticles, in Developments and Applications of Non- Newtonian Flows, eds. D. A. Singer and H. P. Wang, , *American Society of Mechanical Engineers*, New York vol. FED 231, pp. 99–105.

[33] Xuan, Y., and Roetzel, W. (2000). Conceptions for Heat Transfer Correlation of Nano-fluids, *International Journal of Heat and Mass Transfer*, vol. 43, pp. 3701–3707

[34] Eastman, J. A., Choi, S. U. S., Li, S., Soyez, G., Thompson, L. J., and DiMelfi, R. J. (1998). Novel Thermal Properties of Nanostructured Materials, *Journal of Metastable Nanocrystalline Materials*, vol. 2, pp. 629–637

[35] Putra, N., Roetzel, W., and Das, S. K. (2003). Natural Convection of Nano-Fluids, *Heat and Mass Transfer*, vol. 39, no. 8–9, pp. 775–784,

[36] Yousefi T, Veysi F, Shojaeizadeh E, Zinadini S. (2012). An experimental investigation on the effect of Al_2O_3–H_2O nanofluid on the efficiency of flat-plate solar collectors. *Renew Energy;* 39:293–8

[37] Otanicar T., P.E. Phelan, R.S. Prasher, G. Rosengarten, R.A. Taylor. (2010). Nanofluid based direct absorption solar collector, *J. Renew. Sust. Energy* 2 033102

[38] Tyagi H., P. Phelan, R. Prasher. (2009). Predicted efficiency of a low-temperature nanofluid based direct absorption solar collector, *J. Sol. Energy. Eng.* 131 041004-1

[39] Otanicar T., J. Golden. (2009). Comparative environmental and economic analysis of conventional and nanofluid solar hot water technologies, *Environ. Sci. Technol.* 43 6082–6087

[40] Saidur R., S.N. Kazi, M.S. Hossain, M.M. Rahman, H.A. Mohammed. (2011). A review on the performance of nanoparticles suspended with refrigerants and lubricating oils in refrigeration systems, *Renew. Sustain. Energy Rev.*15 310–323

[41] Yousefi T, Veisy F, Shojaeizadeh E, Zinadini S. (2012). An experimental investigation on the effect of MWCNT–H_2O nanofluid on the efficiency of flat-plate solar collectors. *Exp Thermal Fluid Sci;* 39:207–12

[42] Taylor R.A., P.E. Phelan, T.P. Otanicar, R. Adrian, R. Prasher. (2011). Nanofluid optical property characterization: towards efficient direct absorption solar collectors, *Nanoscale Res. Lett*. 6 (1) 1–11

[43] Tyagi, H., Phelan, P., and Prasher, R. (2009). Predicted Efficiency of a Low-Temperature Nanofluid-Based Direct Absorption Solar Collector, *ASME J. Sol. Energy Eng.*, 131 (4), p. 041004.

[44] Otanicar, T., Phelan, P. E., Prasher R. S., Rosengarten G., and Taylor R. A. (2010). Nanofluid-Based Direct Absorption Solar Collector. *J. Renewable Sustainable Energy*. 2(3), p. 033102.

[45] Lenert, A., Zuniga, Y. S. P., and Wang, E. N. (2010). Nanofluid-Based Absorbers for High Temperature Direct Solar Collectors. *Proceedings of the International Heat Transfer Conference* (IHTC14), Washington, D.C., Aug. 8–13, Paper No. IHTC14-22208.

[46] Taylor, R. A., Phelan, P. E., Otanicar, T. P., Walker, C. A., Nguyen, M., Trimble, S., and Prasher, R. (2011). Applicability of Nanofluids in High Flux Solar Collectors. *J. Renewable Sustainable Energy*, 3(2), p. 023104.

[47] Lenert A., E.N. Wang. (2012). Optimization of nanofluid volumetric receivers for solar thermal energy conversion, *Solar Energy*. 86 253–265

[48] Saidur R., K.Y. Leong, H.A. Mohammad. (2011). A review on applications and challenges of nanofluids, *Renew. Sustain. Energy Rev.* 15 1646–1668

[49] Kahrobaian, A. and Malekmohammadi, H. (2008). Exergy Optimization Applied to Linear Parabolic Solar Collectors. *Journal of Faculty of Engineering* 42(1), pp. 131-144.

[50] Ceylan I., A. Ergun, (2013). Thermodynamic analysis of a new design of temperature controlled parabolic trough collector. *Energy Convers. Manag*. 74: 505-510.

[51] Zamfirescu, C. And Dincer, I. (2009). How much exergy one can obtain from incident solar radiation. *Journal of Applied Physics*. 105: 044911-5.

[52] Dincer I., Rosen MA. (2007). Exergy, energy, environment and sustainable development. *Oxford: lsevier*.

[53] Hou H., Z. Yu, Y. Yang, C. Zhou, J. Song. (2014). Exergy analysis of parabolic trough solar collector, *Taiyangneng Xuebao/Acta Energiae Solaris Sin.;* 35(6): 1022-1028.

[54] Liang Hongbo, You Shijun, Zhang Huan. (2015). Comparison of different heat transfer models for parabolic trough solar collectors. *Appl Energy;* 148: 105–14.

[55] Kalogirou, S.A. (2004). STC and Applications. *Progress in Energy & Combustion Science*; 30(3): 231-295.

[56] Al-Suleiman F.A. (2014). Exergy analysis of parabolic trough solar collectors integrated with combined steam and organic Rankine cycles, *Energy Convers. Manag.*; 77: 441-449.

[57] Kaushik SC, Misra RD, Singh N. (2000). Second law analysis of a solar thermal power system. *International Journal of Solar Energy*; 20: 239-53.

[58] Gupta MK, Kaushik SC. (2010). Exergy analysis and investigation for various feed water heaters of direct steam generation solar-thermal power plant. *Renewable Energy*; 35(6): 1228-35.

[59] V. Khullar, H. Tyagi, P.E. Phelan, T.P. Otanicar, H. Singh, R.A. Taylor. (2012). Solar energy harvesting using nanofluids-based concentrating solar

collector, in: Proceedings of MNHMT2012 3rd Micro/Nanoscale Heat & Mass *Transfer International Conference on March 3–6, Atlanta, Georgia, USA.*

[60] Biryukov, S. (2004). Determining the optical properties of PETAL, the 400 m2 parabolic dish at Sede Boqer. *Journal of Solar Energy Engineering* 126, 827–832.

[61] Standards Australia, (2002). Australian Standard for structural design, AS1170.

[62] Johnston, G., (1995). Flux mapping the 400 m2 “Big-Dish” at the Australian National University. *ASME Journal of Solar Energy Engineering* 117, 290–292.

[63] Johnston, G., Lovegrove, K., Luzzi, A. (2003). Optical performance of spherical reflecting elements for use with paraboloidal dish concentrators. *Solar Energy* 74, 133–140.

[64] Lovegrove, K. et al. (2003). Paraboloidal dish solar concentrators for multi-megawatt power generation. *ISES Solar World Congress, Go¨teborg, Sweden*, 16–19 June 2003.

[65] Ulmer, Steffen, Reinalter, Wolfgang, Heller, Peter, Lupfert, Eckhard, (2002). Beam characterization and improvement with a flux mapping system for dish concentrators. *Journal of Solar Energy Engineering* 124 (2002), 182–188.

[66] Shuang-Ying Wua, Lan Xiao, Yiding Cao, You-Rong Li (2010). A parabolic dish/AMTEC solar thermal power system and its performance evaluation. *Applied Energy* 87 452–462

[67] Ngo LC. (2013). Exergetic Analysis and Optimization of a Parabolic Dish Collector for Low Power Application, *Centre for Renewable and Sustainable Energy Studies.* University of Pretoria,

[68] Kaushika, N.D. and Reddy, K.S., (2000). Performance of a low cost solar paraboloidal dish steam generating system. *Energy Conversion and Management* 41(7), pp. 713-726.

[69] Sendhil Kumar, N. and Reddy, K.S. (2008). Comparison of receivers for solar dish collector system. *Energy Conversion and Management*, 49(4), pp. 812-819.

[70] Taylor RA, Phelan PE, Otanicar T, Walker CA, Nguyen M, Trimble S, PrasherR. (2011). Applicability of nanofluids in high flux solar collectors. *Renew Sustain Energy;* 3:023104.

[71] Abid M, Ratlamwala TAH, Atikol U. (2015). Performance assessment of parabolic dish and parabolic trough solar thermal power plant using nanofluids and molten salts. *Int J Energy Res;* 40:550–563.

[72] T. Otanicar, R. A. Taylor, P. E. Phelan, and R. Prasher. (2009). *Proceedings of the Third International Conference on Energy Sustainability*.

[73] H. Tyagi, P. E. Phelan, and R. Prasher, J. (2009). Predicted efficiency of a Low-temperature Nanofluid-based direct absorption solar collector *Sol. Energy Eng.* 131, 4. 20P.

[74] E. Phelan, P. Bhattacharya, and R.S. Prasher. (2005). Nanofluids for heat transfer applications, Annu. *Rev. Heat Transfer*, Vol. 14, P. 255–275.

[75] Bong TY, Ng K, Tan AO. (1987). Performance study of a solar-powered air-conditioning system. *Solar Energy;* 39(3):173–82.

[76] Z.C. Huang, W.H. Xia, W.B. (1991). Ma A 2-stage LiBr absorption chiller for solar cooling, *Proceedings of the Biennial Congress of the International Solar Energy Society ISES, Denver,* pp. 1643–1648

[77] Li Jianhong, Ma Weibin, Jiang Qing A. (1999). 100 kW solar air-conditioning system *Acta Energiae Solaris Sinica,* 20 (3), pp. 239–243

[78] He Zinian, Zhu Ning, Liu Fang, Guo Shuling. (2001). Design and performance of a solar absorption air conditioning and heat supply system *Acta Energiae Solaris Sinica,* 22 (1), pp. 6–1

[79] F. Assilzadeh, S.A. Kalogirou, Y. Ali, K. (2005). Sopian Simulation and optimization of a LiBr solar absorption cooling system with evacuated tube collectors *Renewable Energy*, 30, pp. 1143–1159.

[80] M. Izquierdo, P. Rodríguez, A. Lecuona, E. Martín. (1998). Energetic, economic and environmental viability of absorption air-conditioning systems in Spain *IEA Heat Pump Center Newsletter*, 16 pp. 24–25

[81] A. Syed, M. Izquierdo, P. Rodríguez, G. Maidment, J. Missenden, A. Lecuona, R. Tozer (2005). A novel experimental investigation of a solar cooling system in *Madrid International Journal of Refrigeration*, 28 (6) pp. 859–871

[82] M. Izquierdo, M. Venegas, P. Rodríguez, A. Lecuona. (2004). Crystallization as a limit to develop solar air-cooled LiBr–H2O absorption systems using low-grade heat. *Solar Energy Materials & Solar Cells*, 81, pp. 205–216

[83] F. Asdrubali, S. Grignaffini. (2005). Experimental evaluation of the performances of a H20–LiBr absorption refrigerator under different service conditions. *International Journal of Refrigeration*, 28, pp. 489–497

[84] M. Engler, G. Grossman, H.M. Hellmann. (1997). Comparative simulation and investigation of ammonia–water absorption cycles for heat pump applications *Int. J. Refrigeration*, 20 (7), pp. 504–516

[85] Hammad, M. A., Audi, M.S., (1992). Performance of a solar LiBr-water absorption refrigeration system. *Rennewable energy* 2 (3), 275-282

[86] Haim, I., Grosman, G., Shavit A. (1992). Simulation and analysis of open cycle absorption system for solar cooling. *Sol.Energy* 49 (6), 515-534

[87] Hawlader, M.N.A., Nooval, K.S., Wood B.D. (1993). Unglazed collector/regenerator performance of a solar assisted open cycle absorption cooling system *Sol. Energy* 50 (1), 59-73

[88] Ghaddar N. K., Shihab M., Bdier F. (1997). Modelling and simulation of solar absorption system performance in Beirut. *Renewable Energy* 10 (4), 539-558

[89] M.B Arun, M.P Maiya, S.Srinivasa. (2001). Murthy Performance comparison of double-effect parallel-flow and series flow water– lithium bromide absorption systems, *Applied thermal Engineering*, 21, pp. 1273–1279.

[90] R. Gomri. (2010). Investigation of the potential of application of single effect and multiple effect absorption cooling systems, *Energy Conversion and Management*, 51, pp. 1629–1636

[91] Ravikumar TS, Suganthi L, Anand AS. (1998). Exergy analysis of solar assisted double effect absorption refrigeration system. *Renewable Energy;* 14:55–59. DOI: 10.1016/S0960-1481(98)00047-0.

[92] R. Gomri. (2009). Second law comparison of single effect and double effect vapor absorption refrigeration systems. *Energy Conversion and Management* 2009; 50:1279–1287. DOI: 10.1016/j.enconman.01.019

[93] Worek .WM, Ludovisi. D, Meckler. M. (2003). Enhancement of a double-effect absorption cooling system using a vapor recompression absorber, *Energy*. 28, pp. 1151–1163

[94] L. Garousi Farshi, S.M.S. Mahmoudi, M.A. Rosen, M. Yari, M. Amidpour. (2013). Exergoeconomic analysis of double effect absorption refrigeration systems, *Energy Conversion and Management*, 65 pp. 13-25

[95] G. Grosman, M. Wilk and R. C. DeVaulb. (1994). Simulation and performance analysis of triple-effects absorption cycles. *ASHRAE Transactions 100*, Part 1

[96] Lee S.F., Sherif S.A., (2001). Thermodynamic analysis of a lithium bromide/water absorption system for cooling and heating applications. *Int J. Energy Res.* 25, 1019-1031.

[97] Gomed, K., Grossman. G. - Performance analysis of staged absorption heat pumps: Water- lithium bromide systems. *ASHRAE Transactions* 96(1), p. (1590-1598).

[98] M. B. Arun, M. P. Maiya, and S. S. Murthy. (2001). Performance comparison of double effect parallel-flow and series flow water–lithium bromide

absorption systems. *Applied Thermal Engineering*, vol. 21, no. 12, pp. 1273-1279, Aug.

[99] Oh MD, Kim SC, Kim YL, Kim Y. (1994). Cycle analysis of air-cooled, double-effect absorption heat pump with parallel flow type. In: *Proceedings of the International Absorption Heat Pump Conference, New Orleans*, p. 117–23.

[100] Oouchi, T., Usui, S., Fukuda. K., and Nishiguchi, A. (1985). Multi-stage Absorption Refrigeration System. *US Patent* No. 4,520,634.

[101] R. C. DeVault and J. Marsala. (1990). Ammonia-water triple-effect absorption cycle. *ASHRAE Trans*. 96 Part 1.

[102] W. J. Biermann and R. C. DeVault. (1992). Triple-effect Absorption Refrigerant System with Double- condenser Coupling, *US Patent Application*, pending.

[103] R. Gormi. (2008). Thermodynamic evaluation of triple effect absorption chiller. *Thermal Issues in Emerging Technologies*, 245 – 250

[104] T.A.H. Ratlamwala, M.A. Gadalla, I. Dincer. (2011). Performance assessment of an integrated PV/T and triple effect cooling system for hydrogen and cooling production, *International Journal of Hydrogen Energy*, 36, 11282–11291

[105] G. Grossman, M. Wilk, R.C. DeVault. (1994). Simulation and performance analysis of triple-effect absorption cycles, *ASHRAE Trans*. 100 (2) 452– 462.

[106] Y. Kaita. (2002). Simulation results of triple-effect absorption cycles, *Int. J. Refrigeration* 25 (7) 999–1007.

[107] S. Sedigh, H. Saffari. (2012). Thermodynamic analysis of triple effect absorption refrigeration systems, *Int. J. Energy Technol*. 4 (7) 1–8.

[108] Ratlamwala TAH, Gadalla MA, Dincer I. (2010). Performance Assessment of an Integrated PV/T and Triple Effect Cooling System for Hydrogen and Cooling Production. *International Conference on Hydrogen Production*.

[109] Gadalla MA, Ratlamwala TAH, Dincer I. (2010). Energy and exergy analysis of an integrated fuel cell and absorption cooling system. *International Journal of Exergy*; 7:731–754.

[110] Ratlamwala TAH, Gadalla MA, Dincer I. (2010). Evaluation of a triple effect absorption air-conditioning system integrated with PEM fuel cell. *Proceedings of the ASME 2010 Eighth International Fuel Cell Science,* Engineering and Technology Conference.

[111] Ratlamwala TAH, El-Sinawi AH, Gadalla MA, Aidan A. (2012). Performance analysis of a new designed PEM fuel cell. *International Journal of Energy Research. Doi: 10.1002/ er.1877.*

[112] Dincer I, Dost S. (1996). A simple model for heat and mass transfer in absorption cooling systems (ACSs). *International Journal of Energy Research; 20:237-43.*

[113] Ratlamwala TAH, Gadalla MA, Dincer I. (2011). Performance assessment of an integrated PV/T and triple effect cooling system for hydrogen and cooling production. *International Journal of Hydrogen Energy*; 36(17):11282-91.

[114] R. Gomri. (2010). Investigation of the potential of application of single effect and multiple effect absorption cooling system. *Energy Convers. Manage*. 51 1629–1636.

[115] Alefeld, G. (1987). What needs to be known about fluid pairs to determine heat ratios of absorption heat pumps and heat transformers? In: *Proceedings of IEA Heat Pump Conference.* Orlando, FL (Chapter 26).

[116] Ziegler, F., Brandl, F., Volkl, J. and Alefeld, G. (1985). A Cascading Two-Stage Sorption Chiller System Consisting of a Water-Zeolite High Temperature Stage and a Water-LiBr Low Temperature Stage. *Proceedings, the Absorption Heat Pumps Congress*. Paris, France, March 20-22, pp. 231-238.

[117] Xu, G.P., Dai, Y.Q. (1997). Theoretical analysis and optimization of a double-effect parallel flow type absorption chiller. *Appl. Therm. Eng*. 17 (2), 157-170.

[118] Arun, M.B.,Maiya, M.P.,Murthy, S.S. (2000). Equilibrium low pressure generator temperatures for double effect series flow absorption refrigeration systems. *Appl. Therm. Eng.* 20, 227-242.

[119] De Vault, R.C. (1988). Triple-effect absorption chiller utilizing two refrigerant circuits". *U.S. Patent* 4,732,008, March 22.

[120] Ratlamwala TAH, Dincer I., Gadalla MA. (2012). Thermodynamic analysis of a novel integrated geothermal based power generation-quadruple effect absorption cooling-hydrogen liquefaction system. *International Journal of hydrogen energy*. 37 5840-5849

[121] Ratlamwala TAH, Dincer I., Gadalla MA. (2013). Energy and exergy analyses of an integrated solar-based desalination quadruple effect absorption system for freshwater and cooling production. *Int. J. Energy Res*. 37:1569–1579

[122] Klein, S.A. (2009). Engineering Equation Solver, v8.411. *F-Chart Software.* Madison, Wisconsin.

[123] Kalogirou S. A. (2009). Solar energy engineering: processes and systems. London: *Elsevier Inc*,

[124] Duffie, J. and Beckman, W. (2006). Solar Engineering of Thermal Processes. *2nd edition*. *John Wiley and Sons.* New Jersey

[125] Ratlamwala, T.A.H., Dincer, I., M. Aydin. (2012). Energy, exergy analyses and optimization study of an integrated solar heliostat field system for hydrogen production. *International journal of hydrogen energy* 37 18704-18712.

[126] Petela, R. (2010). Discussion of Radiation Exergy Formulae Proposed by Researchers. *Engineering Thermodynamics of Thermal Radiation*. McGraw-Hill, pp. 247-263.

[127] Younus A. Cengel, Michael A. Boles. (2011). Thermodynamics: *An engineering approach. 7th ed. in SI units* New York. Mcgraw-Hill;

[128] Incropera P. Frank, Dewitt P. David, Bergman L. Theodore, Lavine S. Adrienne. (2006). *Fundamentals of Mass and Heat Transfer*. 6th edition. John Wiley and Sons,

[129] Wu, S., Xiao, L., Cao, Y. And Li, Y. (2010). A parabolic dish/AMTEC solar thermal power system and its performance evaluation. *Applied Energy*, 87(2), pp. 452-462.

[130] A. Hajizadeh, F. Ranjbar, S.M. Seyed. (2008). Performance comparison of triple-effect parallel flow and series flow absorption refrigeration systems *J. Appl. Sci*, 8 (16) pp. 2913–2918

[131] Berhane H. Gebreslassie, Marc Medrano, Dieter Boer. (2010). Exergy analysis of multi-effect water–LiBr absorption systems: From half to triple effect. *Renewable Energy* 35 1773–1782.

[132] US research nanomaterials inc. http://www.us-nano.com/inc/sdetail/209.

[133] K. Khanafer, K. Vafai. (2011). A critical synthesis of thermophysical characteristics of nanofluids. *Int. J. Heat. Mass Transf*. 54 4410-4428.

[134] M. Ayatollahi, S.H. Nasiri, A.B. Kasaeian. (2012). Convection heat transfer modeling of Ag nanofluid using different viscosity theories, *IIUM Eng*. J. 13 (1).

[135] W. Yu, S.U.S. Choi (2004). The role of interfacial layers in the enhanced thermal conductivity of nanofluids: a renovated Hamilton-Crosser model, *J. Nanoparticle Res*. 6 (4) 355-361.

[136] J.C. Maxwell (1881). A Treatise on Electricity and Magnetism, *second ed., Clarendon Press*, Oxford, UK.

[137] G.K. Batchelor (1977). The effect of Brownian motion on the bulk stress in a suspension of spherical particles, *J. Fluid Mech*. 83 97-117.

[138] J. Leinhard IV, J. Leinhard V. (2012). A Heat Transfer Textbook, *fourth ed., Philogiston Press*, USA, pp. 354-360.

[139] A.P. Colburn (1933). A method for correlating forced convection heat transfer data and a comparison with fluid friction *Trans. Am. Inst. Chem. Engrs*, 29 pp. 174–210

[140] Defoe C. Ginnings and Robert 1. Corruccini (1947). Enthalpy, Specific Heat, and entropy of Aluminum Oxide from 0° to 900° C. *U. S. Department of Commerce National Bureau of Standards*. June, Volume 38

[141] Claine L. Snow, Christopher R. Lee, Quan Shi, Juliana Boerio-Goates, Brian F. Woodfield. (2010). Size-dependence of the heat capacity and thermodynamic properties of hematite (a-Fe2O3). *J. Chem. Thermodynamics* 42 1142–1151

[142] Mikako Takeda, Takashi Onishi, Shouhei Nakakubo and Shinji Fujimoto. (2009). Physical Properties of Iron-Oxide Scales on Si-Containing Steels at High Temperature. *Materials Transactions*, Vol. 50, No. 9 pp. 2242 to 2246.

[143] Patek, J., Klomfar, J. (2006). A computationally effective formulation of the thermodynamic properties of water-lithium bromide solutions from 273 to 500 K over full composition range. *Int. J. Refrig.* 29, 566-578.